# University of Zurich UZH

# Ice Sheet Margin on the Rocks – A Century of Thinning, Retreat and Velocity Measurements at a Land-Terminating Ice Sheet Margin in West Greenland

GEO 511 Master's Thesis

**Author**
Simon Schudel
12-709-069

**Supervised by**
Dr. Martin Lüthi

**Faculty representative**
Prof. Dr. Andreas Vieli

30.01.2019
Department of Geography, University of Zurich

University of
**Zurich** UZH

Geo 511 Master's Thesis

# Ice Sheet Margin on the Rocks

## A Century of Thinning, Retreat and Velocity Measurements at a Land-Terminating Ice Sheet Margin in West Greenland

*Author*

Simon Schudel

simon.schudel@gmail.com

12-709-069

*Supervisor*

Dr. Martin Lüthi

martin.luethi@geo.uzh.ch

*Supervisor & Faculty Member*

Prof. Dr. Andreas Vieli

andreas.vieli@geo.uzh.ch

31st of January 2019

Department of Geography, University of Zurich

# Summary

This thesis focuses on a section of the rarely researched, slow flowing and land-terminating ice margin. The study site close to the Eqip Sermia outlet glacier in West Greenland is split into two subareas: *Nunap Kigdlinga*, a slow and relatively flat ice-margin with little to no dynamic influences and *Sermeq Kujalleq*, a lobe-shaped glacier tongue. Both areas are characterized by an exceptional historical data availability, enabling the assessment of surface elevation change, ice extent and velocity over a period of more than a century. Historic sources such as aerial images or early topographic maps are combined with state-of-the-art techniques like Structure from Motion (SFM) in order to retrieve information that has not before been analyzed. Historic data is supplemented with the newest releases of remote sensing data such as the ArcticDEM, as well as differential GPS measurements and very-high-resolution drone imagery acquired in a field campaign in July 2018.

The results show that Nunap Kigdlinga and Sermeq Kujalleq both underwent very similar temporal changes in terms of surface elevation change albeit in different magnitudes. The surface elevation was relatively stable between 1912 and 2003, with hints of a slight elevation increase between the 1980s and 2003. Since then, a drastic surface lowering, and a retreat for Sermeq Kujalleq has set in, which lasts until today. The speed and magnitude of this surface lowering and retreat is unprecedented in the century before this. The ice flow velocity has remained relatively stable at Nunap Kigdlinga and was roughly halved at Sermeq Kujalleq as an effect of the retreat and thinning since 2003. The above-mentioned cumulative surface elevation changes can be reproduced using calibrated cumulative positive degree month temperatures from different temperature datasets. This hints at a strong connection between the observed changes and atmospheric temperature developments. The signature of the changes also bears striking similarities with the nearby Eqip Sermia outlet glacier, whereat the retreat and thinning of Eqip Sermia is about five times larger in magnitude than for Sermeq Kujalleq. This suggests that the change of the outlet glacier may not have solely been caused by oceanic temperature anomalies. Further research of slow flowing land-terminating ice margins is encouraged in order to close the knowledge gap about these types of margins and to improve the understanding of the role and importance of surface mass balance, which is the most important factor contributing to change in these areas.

# Acknowledgements

# Table of Contents

# List of Abbreviations

| | |
|---|---|
| ALS | airborne laser scanning |
| AOI | area of interest |
| ASTER | Advanced Spaceborne Thermal Emission and Reflection Radiometer |
| AWS | automated weather station |
| DEM | digital elevation model |
| DLR | *Deutsches Zentrum für Luft- und Raumfahrt* (German Aerospace Center) |
| DSM | digital surface model |
| DTM | digital terrain model |
| EBM | Energy Balance Model |
| EGIG | *Expédition Glaciologique Internationale au Groenland* (international glaciological expedition in Greenland) |
| EPF | *Expédition Polaires Françaises* (French polar expeditions) |
| ETHZ | *Eidgenössische Technische Hochschule Zürich* (Swiss Federal Institute of Technology in Zurich) |
| ETIM | Enhanced Temperature Index Model |
| FOM | figure of merit |
| GC-NET | Greenland Climate Network |
| GCP | ground control point |
| GDEM | Global Digital Elevation Model |
| GIS | geographic information system |
| GIUZ | *Geographisches Institut der Universität Zürich* (Department of Geography at University of Zurich) |
| GLAS | Geoscience Laser Altimeter System |
| GPS | Global Positioning System |
| GrIS | Greenland ice sheet |
| ICESat | Ice, Cloud and Land Elevation Satellite |
| IDW | Inverse Distance Weighting |
| LIDAR | Light Detection and Ranging |
| MVS | Multiview Stereo |
| NGA | National Geospatial-Intelligence Agency of the United States |
| NSF | National Science Foundation of the United States |
| NSIDC | National Snow and Ice Data Center of the United States |
| RADAR | Radio Detection and Ranging |
| RMSE | root mean square error |
| SDFE | *Styrelsen for Dataforsyning og Effektivisering* (The Danish Agency for Data Supply and Efficiency) |
| SFM | structure from motion |
| SIFT | Scale Invariant Feature Transform |
| TIM | Temperature Index Model |
| TIN | triangulated irregular network |
| UAV | unmanned aerial vehicle |
| UNIS | University Centre of Svalbard |
| VNIR | Visible Near Infrared |
| VAW | *Versuchsanstalt für Wasserbau, Hydrologie und Glaziologie* (Laboratory of Hydraulics, Hydrology and Glaciology) |

# List of Figures

# List of Tables

# 1. Introduction

## 1.1. Motivation

'Century', 'thinning measurements' and 'land-terminating margin of the Greenland ice sheet' – the three terms outlining the temporal, thematic and spatial scope of this thesis have never been combined in a scientific paper before. Glaciological research in Greenland is dominated by two types of study approaches. The first type entails a focus on the marine-terminating and fast flowing outlet glaciers, where changes are often dramatic and have implications for their large catchment areas (e.g. Chauché et al. 2014; Holland et al. 2008; Howat et al. 2005; Jouvet et al. 2017; Lüthi et al. 2016; Ryan et al. 2015). In the second type, the whole Greenland Ice Sheet (GrIS) is at the center of attention in order to describe large-scale trends or historical developments (e.g. Fettweis et al. 2017; Joughin et al. 2010; Kjeldsen et al. 2015; Rignot & Kanagaratnam 2006; Zwally et al. 2011). This thesis takes a different approach and focuses on a small section of a slow flowing land-terminating ice margin close to Eqip Sermia, like it exists for thousands of kilometers in Greenland. Due to its location on a historically preferred transect across the GrIS, the data availability for the area of interest (AOI) is exceptional and goes all the way back to the efforts of two early Swiss researchers de Quervain & Mercanton in 1912. A long period of interest is necessary to effectively study the developments in such an inactive area, where the changes are naturally much smaller than for outlet glaciers. Most other studies focusing on this type of slow flowing land-terminating ice margin have aimed at reconstructing the retreat using historic aerial or satellite imagery (e.g. Bjørk et al. 2012), others on the reconstruction of the Holocene development using [10]Be exposure dating or lake sediments as dating techniques (e.g. Carrivick et al. 2017; Håkansson et al. 2014; Kelley et al. 2012; Lesnek & Briner 2018; Levy et al. 2016). However, there has never been a study on a whole century of direct surface elevation measurements at a slow flowing land-terminating Greenland ice sheet margin. In that sense, this thesis is also a first – especially in such a high resolution.

Studying such an ice sheet margin will not only yield information about the little-known development in these areas but may also contribute to a better understanding of the retreat of marine-terminating outlet glaciers. The development of such glaciers is comparably very well documented but allocating it to the forcing of atmospheric or oceanic temperatures is challenging. Both of these are so closely intertwined that it is difficult to estimate the influence of the atmospheric temperatures which dominate the surface melt from above, and the oceanic conditions which dominate the mass loss at the outlet glaciers from below. The AOI of this thesis is disconnected from any direct oceanic influences and dynamic processes associated with changing glacier geometries are also negligible (at least for Nunap Kigdlinga). This makes it a good indicator for isolated surface melt, giving a hint towards the influence of atmospheric temperature forcing in the whole area.

1

## 1.2.    Approach, Aim and Research Questions

A data-centered approach was selected, which entails focusing on the available historic data and selective supplementation with newly generated data, such as high-resolution drone data collected in the field in summer 2018 in order to generate comparable digital elevation models (DEMs). Additionally, historical sources are combined with state-of-the-art techniques (e.g. SFM).

The main goal is to gain new information about the long-term development (period of 1912 to 2018) of Nunap Kigdlinga and Sermeq Kujalleq, two areas of the slow-flowing GrIS margin close to Eqip Sermia. A strong focus is put on the comparability and the uncertainty assessment of the available data sources. The overall aim is achieved by answering the following research questions:

a. How comparable is the data derived from different sources?
   - What are the uncertainties associated with each of the datasets?
b. What is the magnitude, uncertainty and temporal development of the following glacier change parameters: surface elevation change, terminus retreat and ice flow velocity?
   - How far up the ice can thinning be observed and in what magnitude?
c. How do Nunap Kigdlinga and Sermeq Kujalleq compare in terms of surface elevation change and ice flow velocity?
   - Can Sermeq Kujalleq be considered as an 'enhancer' of developments at Nunap Kigdlinga?
d. Can the temporal developments in surface elevation change be linked to changes in temperature?
   - Which temperature dataset best represents the changes observed?

The structure of this thesis was designed as follows: Chapter 2 introduces the study site in a local and regional setting and gives an overview of the exploration history in the 20th century. Chapter 3 is designed to provide the necessary background information on which this study is based on. The broad spectrum of already existing data is presented in chapter 4, while chapter 5 elaborates about how the existing data was incorporated into the thesis and how new data was generated. The results are showcased in chapter 6 before being discussed and put in relation to previous research in chapter 7. In chapter 8, the research questions are answered, before an outlook to further necessary research completes the thesis.

## 2. Study Site

### 2.1. Ice Sheet Margin

The study site at the ice sheet margin is not entirely homogenous. Rather, two areas with different characteristics can be distinguished: The Nunap Kigdlinga ice sheet margin and the Sermeq Kujalleq ice lobe. Both are presented in more detail in the following paragraphs.
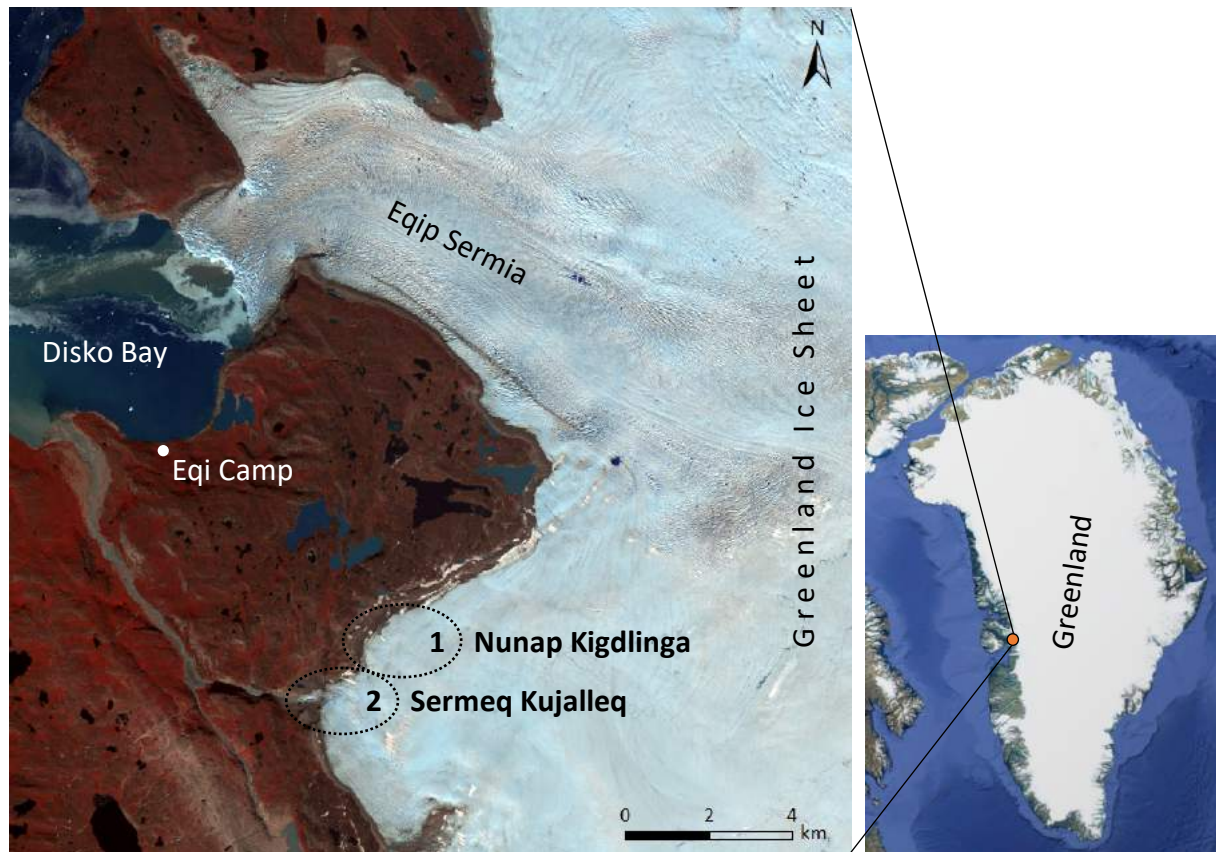


*Figure 1*: Study sites. Area 1 = Nunap Kigdlinga, Area 2 = Sermeq Kujalleq. Marked are also the marine-terminating outlet glacier Eqip Sermia close-by, as well as Eqi Camp, the base camp for the fieldwork in summer 2018. Background: 2016 false color satellite image from ASTER (U.S./Japan ASTER Science Team 2007). Inset map with data from Google Earth (2018).

### 2.1.1. Area 1: Nunap Kigdlinga

To start, some information on the denotation of the area. The name *"Nŭnap Kigdlingâ"* (literal translation: 'border of the land') first appears in Rabot & Mercanton (1913). De Quervain & Mercanton (1920) continue to use this name for the whole ice-free area between Eqip Sermia and Sermeq Kujalleq (see chapter 2.1.2), as well as the ice just to the east of it. In one instance (overview map), this part of the ice is also called *"Sermersŭaq"* (literal translation: 'great ice' or 'large glacier'). Some publications also just refer to this margin with the general Danish term *"Inlandsis"* ('ice sheet').
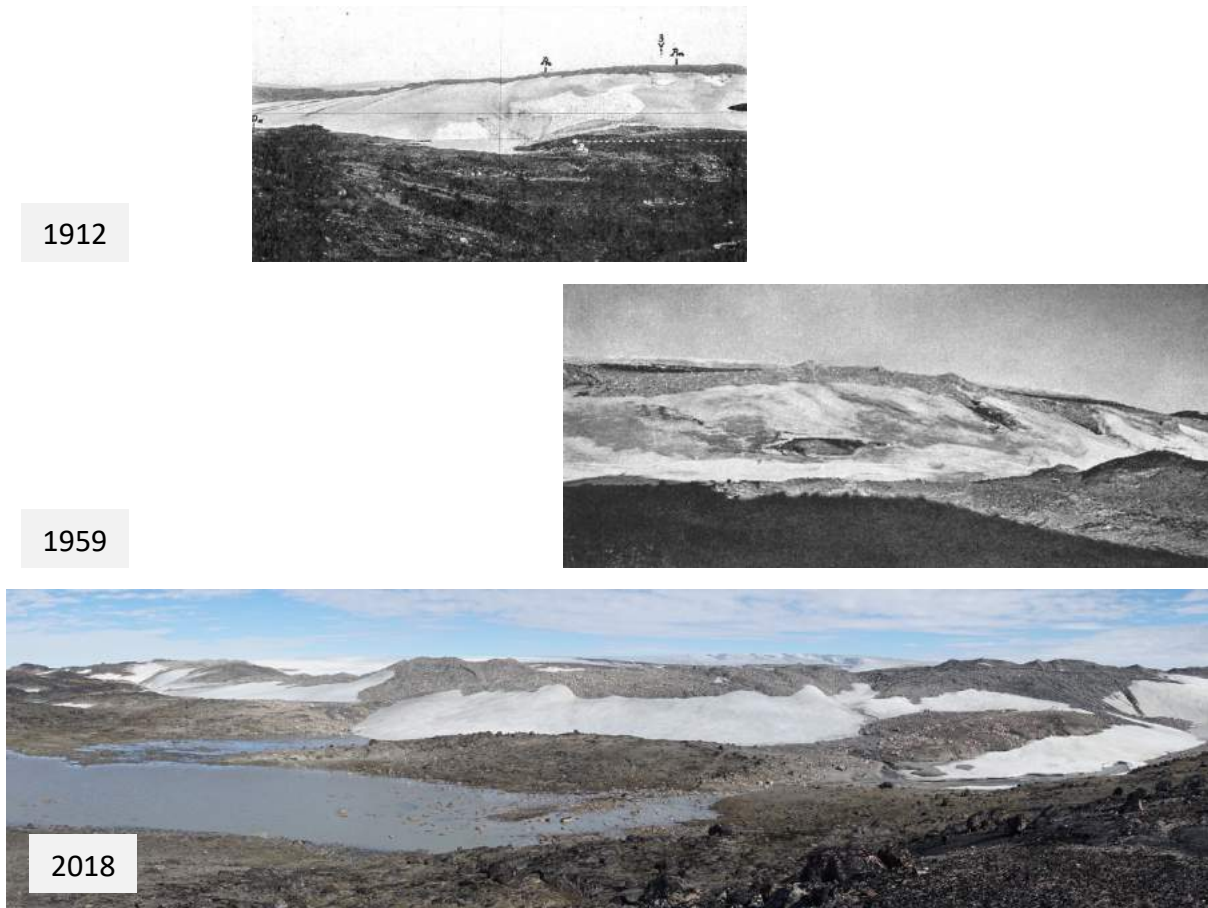
*Figure 2*: *View from Frysefjeld (A15) towards the Nunap Kigdlinga ice margin, direction east. Pictures taken by de Quervain & Mercanton* (1920)*, Bauer* (1968c) *and Simon Schudel (from top to bottom). Note that the exact location of the historic pictures could not be determined. The location of the 2018 image is marked in Figure 86 (Appendix C).*

In this paper, *Nunap Kigdlinga* is used for the area 1 marked in Figure 1. Here, the ice sheet margin is characterized by an even horizontal ice boundary contained by an old moraine complex. The flow velocity is much lower than for Eqip Sermia and changes to the geometry of the boundary are rare and slow (Bauer 1955; de Quervain & Mercanton 1920; Zick 1972). This kind of land-based ice sheet margin is symptomatic for hundreds of kilometers of the GrIS boundary, where the large, fast flowing outlet glaciers are too far away to have a dominant effect on the ice movement. Retreat here is much less dramatic than in marine-terminating glaciers (e.g. Levy et al. 2016). Because of the lack of 'action' and the fact that changes only happen very small-scale and long-term, such ice sheet margins have been rarely studied or monitored.

The Kigdlinga ice sheet margin in particular is characterized by a sequence of different zones of terrain and ice. Hansen (1968) describes these characteristics of the ice margin at Nunap Kigdlinga in detail and states that it is in complete compliance with an ice-margin at *Frederiksåb Isblink* in Southwest Greenland, which he had sketched earlier. Figure 3 is an adapted and supplemented version of said sketch. The following zones can be differentiated – going from the ice-free area (NW) towards the ice sheet (SE):

4

1. Historic moraine complex
2. Meltwater-streams and proglacial lakes and ponds
3. Seasonal snow accumulation at the steep ice margin – also called *'parasite glacier'* (Bauer 1968c; de Quervain & Mercanton 1920). Hansen (1968) describes it as a clearly independent formation in front of the moraine.
4. Steep ice margin / ice cored moraine with large boulders and thick sediment cover
5. Less steep, dirty ice with some boulders and gravel, narrow parallel bands of fine-grained material, apparently representing the sliding surfaces of the ice
6. Strong border between clean and dirty ice
7. Clean ice without any debris taken up from the bed, small melt water streams and occasional cryoconite holes
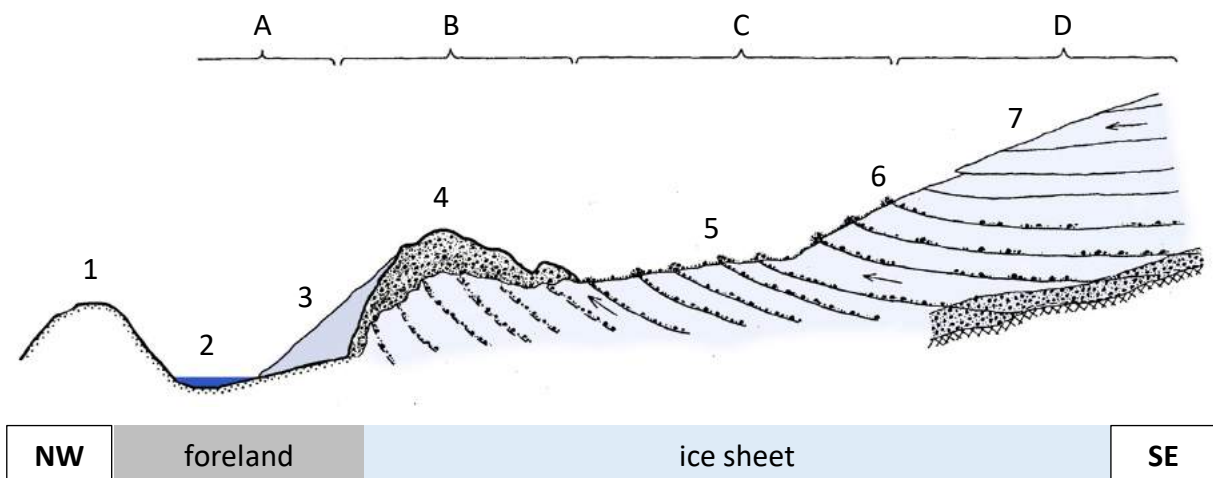


*Figure 3*: *Schematic topographic sequence of the Nunap Kigdlinga ice sheet margin. The numbers correspond to the zone classification presented in this thesis, while the letters correspond to the original classification by Sigurd Hansen. Sketch adapted and supplemented from Hansen* (1968: 309)*.*

The ice under the moraine is hardly moving anymore but is protected by both the thick debris cover on top as well as the snow accumulation in front of it. This inactivity forces the successional ice to surface along relatively steep gliding surfaces described also by de Quervain & Mercanton (1920). The debris which originates at the glacier bed and is entrained in the basal ice is transported along these gliding lines to the surface. In zone (5) this debris is deposited and partly washed away by supraglacial melt water. Large boulders remain and are slowly transported further to zone (4), where they will make up the moraine. Hence zone (4) is a mix of deposited debris and ice with entrained debris, which makes it difficult to make a distinction between an ice-cored moraine or just debris-covered ice. Zones 2, 3 and 4 are well visible in Figure 2, while Figure 4 depicts the debris bands of zone 5. Another picture of zones 4 and 5 can be found in Appendix C (Figure 88).

***Figure 4****: The different sliding surfaces and the resulting debris bands in zone 5 of Nunap Kigdlinga. For location of the image refer to Figure 86. Image by Simon Schudel (July 2018).*

As we can see, the description of the sequence by Hansen (1968: 309) is almost identical:

A.  Barren open terrain ("*Hedeslette"*)
B.  Moraine cover, dead ice ("*Morænedækket dødis"*)
    → corresponds to (4)
C.  Sludge covered ice with little movement ("*Slamdækket is med ringe bevægelse"*)
    → corresponds to (5)
D.  Active clean ice with clean sliding surfaces and stronger movement ("*Levende, ren is med rene glideflader og stærkere bevægelse"*)
    → corresponds to (7)

However, he describes the moraine (B, 4) as *'dead ice'*. By definition, that is ice that is no longer under the influence of flow dynamics and often detached from the active ice body. However, both Bauer (1968c) and de Quervain & Mercanton (1920) describe some movement of the moraine crest (about 2m/y) and therefore the denomination 'dead ice' is not correct. In this thesis, the term 'ice-cored moraine' will be used for this zone. The description for the barren open terrain (A) was particularized in this thesis.
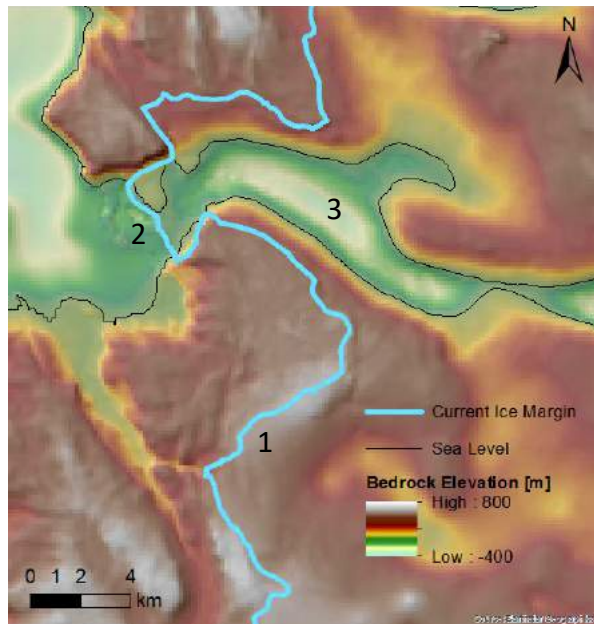
*Figure 5: Bedrock topography of the study site, (1) Nunap Kigdlinga ice sheet margin. (2) Current terminus of Eqip Sermia outlet glacier. (3) Bedrock basin underneath Eqip Sermia outlet glacier. Data from Morlighem et al. (2017).*
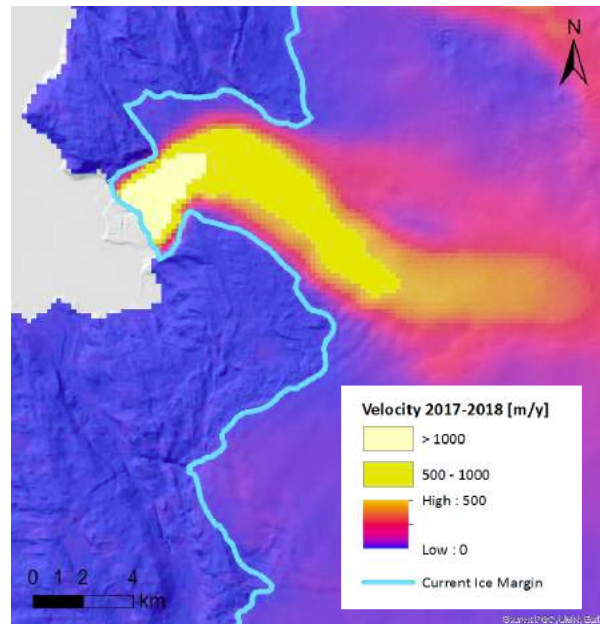
*Figure 6: Ice flow velocity between 2017 and 2018. New data from Joughin et al. (2015). Note that the ice sheet margin of Nunap Kigdlinga is not affected by the fast flow of Eqip Sermia.*

Looking at the bed topography (Figure 5), as well as the ice flow velocity (Figure 6) it is obvious that currently, the Kigdlinga ice sheet margin is under no direct or dynamic influence by the Eqip Sermia outlet glacier. However, this may be bound to change: With the expected retreat of Eqip Sermia into the large basin (see number 3 in Figure 5), the ice surface further upstream could steepen, which in turn would increase flow velocities of the surrounding ice, maybe enlarging the catchment of Eqip Sermia in this area all the way to the study site at Nunap Kigdlinga.

### 2.1.2.    Area 2: Sermeq Kujalleq

First, a short note on the name Sermeq Kujalleq is necessary. The ice lobe in question is called *"Sermek Kujadlek"* or *"Sermerk Kujadlek"* by de Quervain & Mercanton (1920), which is an old form of Greenlandic writing and means 'southern glacier'. Due to the fact that many glacier and landscape names in Greenland are similarly generic, there are at least 6 other glaciers in Greenland with this name, the most prominent being '*Jakobshavn Isbræ'* close to Ilulissat, as well as *'Store Gletsjer'* (Danish for *'large glacier'*) about 75km north of the study site, whose Greenlandic names are also 'Sermeq Kujalleq'  (Bjørk et al. 2015). In this paper, the term 'Sermeq Kujalleq', which is the modern Greenlandic spelling, is exclusively used for the ice lobe marked in Figure 1.

Sermeq Kujalleq is an area where the ice coming from the GrIS cascades over a series of topographic steps into a valley. The lobe ends in a large glacier mouth and a meltwater stream, which drains off to a delta situated a couple kilometers west of Eqi Camp (see Figure 1). The glacier mouth lies at about 200m.a.s.l., so almost 400m below the average altitude of the surrounding ice sheet margin. Due to the surface steepness, the ice surface of Sermeq Kujalleq is

much more rugged and inaccessible than the one of Nunap Kigdlinga and has an appearance similar to an alpine valley glacier.



*Figure 7: Glacier mouth of Sermeq Kujalleq. For location of the image refer to Figure 86. Image by Simon Schudel (July 2018).*

## 2.2. Regional Setting

### 2.2.1. Greenland Ice Sheet (GrIS)

An ice sheet is defined as an ice body larger than 50'000 $km^2$, covering the entire landscape in its central areas. After the Antarctic ice sheet, the Greenland Ice Sheet (GrIS) is the smaller one of the two currently existing ice sheets in the world. It measures 1,736,000 $km^2$ and contains around 2.6 million $km^3$ of ice, equivalent to almost 7m of global sea-level rise (Benn & Evans 2010; Dowdeswell 2006).

One of the fundamental principles in glaciology is the distinction between ablation zone and accumulation zone of an ice body. The accumulation zone describes the part of the glacier or the ice sheet where the annual accumulation exceeds the annual ablation, while the ablation zone is the part where the annual ablation exceeds the annual accumulation. Because the ice at the boundary between these two areas is in an equilibrium (in an annual timescale), it is called equilibrium line. Ice sheets can also be separated into different functional areas, such as ice domes, the elevated central parts with slow ice flow velocities, ice streams with higher flow velocities transporting the ice towards the margins and fast-flowing outlet glaciers, where most of the ablation happens through calving at the marine-terminating glacier fronts (Benn & Evans 2010).

The study site of this thesis is situated at an elevation of about 300-700 m.a.s.l. and therefore still well below the equilibrium line altitude, which is currently located at about 1000 m.a.s.l. in this area (Håkansson et al. 2014), and thus considered to be located in the ablation zone of the GrIS. It is not characterized as one of the above-mentioned typical functional areas. It is slow-flowing, but too peripheral to be considered as a part of an ice dome. Instead it is simply a slow-flowing ice margin that is not directly affected by any ice stream or outlet glacier. The accumulation zone of the study site is not directly the focus of this study but is obviously inseparably connected to it.

Despite a thickening trend above 2000 m.a.s.l., recent studies of the GrIS have shown that there is a pronounced development towards a more negative total mass balance (Pritchard et al. 2009; Zwally et al. 2011). This development in total mass balance is the result of two main influences: The surface mass balance (SMB = runoff + sublimation – precipitation), as well as

the mass loss caused by ice dynamics (Rignot & Kanagaratnam 2006). This dynamic thinning is triggered by the retreat, thinning and increased velocity of outlet glaciers, which propagates upstream – a process that has reached all latitudes of Greenland (Davis & Sun 2004; Joughin et al. 2010; Pritchard et al. 2009; Rignot & Kanagaratnam 2006; Zwally et al. 2011). The role and importance of these two influences is not entirely clear and may depend also on the analyzed time-scale: Rignot & Kanagaratnam (2006) found that Greenland's mass loss has doubled between 2000 and 2005 and identified the SMB to be responsible for about one third of the mass loss of the GrIS, while glacier dynamics at ocean margins are responsible for the most drastic changes. This finding is supported by Pritchard et al. (2009). Kjeldsen et al. (2015) on the other hand state that while short-term dynamic variability may affect the mass balance, the driving factors for changes in the GrIS mass balance, at least in a long-term context, are the SMB variabilities. These variabilities may not follow a clear trend, as the study by Box (2013) suggests: The effect of increasing air temperatures may be partly compensated by increasing accumulation. However, other studies (e.g. Hanna et al. 2011) conclude that the SMB has in fact decreased in the last century.

It is also important to notice that there are regional differences across the GrIS: Fast-flowing areas generally thin much more rapidly than slow flowing areas (Rignot & Kanagaratnam 2006; Pritchard et al. 2009; Kjeldsen et al. 2015). At the southwestern, predominantly land-terminating ice sheet margin for example, a positive dynamic mass contribution has been observed (Kjeldsen et al. 2015) with thickening rates of up to 44 ± 0.5cm/y between 1996 and 2005 (Pritchard et al. 2009). The opposite is true for e.g. the southeast and northwest, where marine-terminating glaciers play a stronger role and thinning rates of 1-2m/y are observed, leading to the above-mentioned dynamic thinning propagation upwards for distances of up to 120 km (Jakobshavn Isbræ) (Davis & Sun 2004; Kjeldsen et al. 2015; Pritchard et al. 2009).

### 2.2.2. Eqip Sermia Outlet Glacier

Eqip Sermia is a large marine-terminating outlet glacier of the GrIS with a very dynamic ice flow and large changes in ice extent and surface elevation over the past century. It is located only a few kilometers north of the AOI (see Figure 1). The first record of the glacier terminus location dates back to 1912 (de Quervain & Mercanton 1925). After a short phase of advancement until 1920, the glacier undulated backwards with both phases of stagnation and phases of faster retreat (Bauer 1955; Lüthi et al. 2016). This retreat can be linked with both oceanic and atmospheric temperature forcing, while a distinction between the two is difficult (Lüthi et al. 2016). Since 2000, the retreat of the terminus has accelerated drastically (see Figure 8), while the ice flow velocity experienced a significant increase, especially since 2010 (Lüthi et al. 2016; Rignot & Kanagaratnam 2006). The retreat takes place in a step-wise motion, like it is typical for marine-terminating glaciers affected by shallow areas in the fjord.
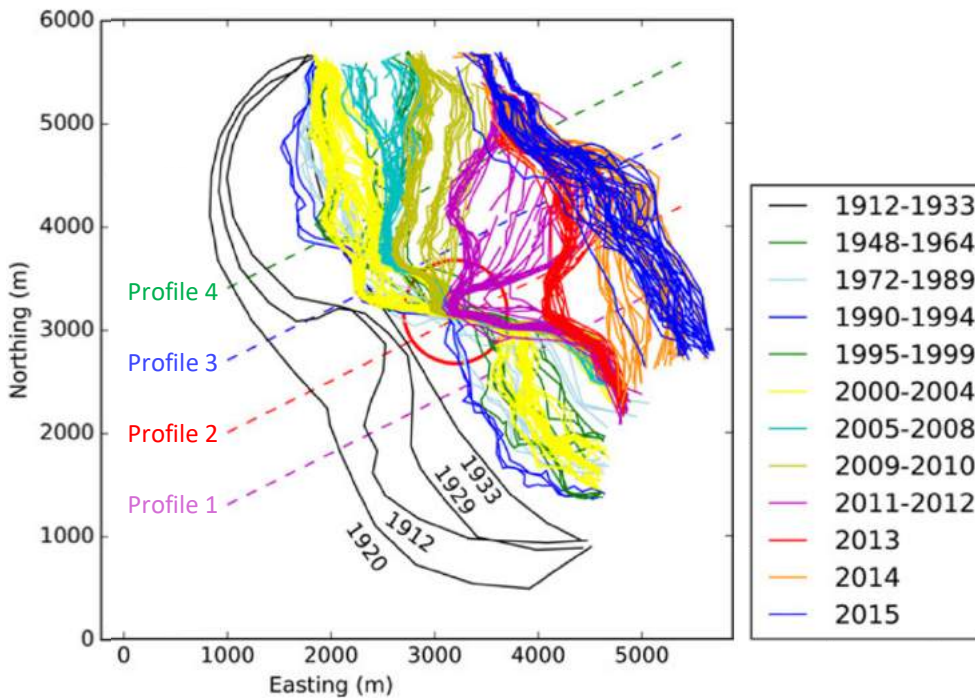
*Figure 8*: *Terminus positions of Eqip Sermia from 1912 to 2015 in map plan view (Polar Stereographic projection; EPSG:3413), offsets with respect to (206000, 2206000)). The red circle identifies a position of shallow bedrock with influence on the retreat. The longitudinal retreat profiles 1–4 are displayed in Figure 65. Adapted from Lüthi et al.* (2016: 645)*.*

The current terminus also rests on such relatively shallow area of the bay (ca. 100m deep), but the bedrock is known to reach depths of up to 400m further up (Morlighem, C. N. Williams, et al. 2017). If the terminus reaches this basin (see Figure 5), a fast retreat of up to 10km is possible, before reaching more shallow areas again (Lüthi et al. 2016). This could happen for several outlet glaciers in Greenland in the next decades. The effects include a dynamic thinning trend propagating up the ice sheet and could last for centuries (Joughin et al. 2010; Lüthi et al. 2016).

## 2.3. Exploration History

The ice sheet margin at Nunap Kigdlinga offers a comparably easy and short access from the fjord to the GrIS, which was especially important for material-intensive traversing expeditions. This was already discovered and utilized in the year of 1912 by a Swiss group of researchers surrounding Alfred de Quervain and Paul-Louis Mercanton (Barr 2015; de Quervain & Mercanton 1925). For this reason, this location was regularly visited and studied in the last century. The following paragraphs provide a short overview.

### 2.3.1. De Quervain and Mercanton 1912

After his first Greenland expedition to the area of Uummannaq in 1909, de Quervain returned in 1912 with the goal of traversing the GrIS to Ammassalik (Tasiilaq). The group of seven Swiss researchers underwent extensive training in dog sledging and arctic survival before going ashore in Quervainshavn, the bay of the Eqip Sermia glacier terminus. From there it was a comparably easy and short trip to the ice edge, where a base camp was set up. The group then split in an eastern group led by Alfred de Quervain and a western group led by Paul-Louis

Mercanton. The eastern group comprised of four people who managed to become only the second successful expedition to cross the GrIS after Fridtjof Nansen in 1888, while the western group remained at the Kigdlinga ice margin to do extensive measurements including the mapping of both the sheet margin and Sermeq Kujalleq, measuring ice flow velocity as well as meteorological parameters etc. (Barr 2015; de Quervain & Mercanton 1920; de Quervain & Mercanton 1925; Mercanton 1914; Rabot & Mercanton 1913). Note that the two main publications from 1920 and 1925 are virtually identical. In this paper, only the earlier and slightly more detailed version of 1920 will be cited.



*Figure 9*: *Footage of the 1912 Swiss Expedition under Alfred de Quervain. Map of the ice sheet crossing (left). Hand-colored photographs of the expedition ship 'Fox' in front of the Eqip Sermia calving front (center) and the expedition team on the highest point of their ice sheet crossing (right). Images from de Quervain & Mercanton* (1920) *and the ETHZ Library Image Archive* (2019).

Regardless of undoubtedly important results in glaciological research, there is another aspect of the expedition which should not go unnoticed and should be viewed critically from today's point of view: Like all scientific actions in Greenland at the time, the expedition was connected to colonialist developments and the Swiss researchers also participated in the colonialist race science by breaking open gravesites in order to measure and document skulls of the Inuit (de Quervain & Mercanton 1920; Müller 2016).

### 2.3.2. French Expeditions (EPF and EGIG)

The next major expeditions to the area were organized by *Expéditions Polaires Françaises* (EPF), which started off in 1947 as a private organization founded by Paul-Emile Victor and funded by the French government (LeSchack 1964). Apart from several expeditions to Antarctica, six summer campaigns and two winter campaigns were conducted in Greenland from 1948 to 1953. The working area consisted mainly of the Eqip Sermia glacier terminus as well as the GrIS, which was explored on several trajectories, delivering first important data about its thickness (Bauer 1953; Bauer 1954; Bauer 1955; Holtzscherer & Bauer 1954; LeSchack 1964). However, the area of Nunap Kigdlinga was also further examined and measured (Bauer 1968c; Tschaen 1959).

With the efforts to strengthen the French claims in the Antarctic Territories, EPF in particular and polar research in general became more and more influenced by politics. This eventually led to the EPF being a quasi-public organization representing France. The focus shifted to

Antarctica (Terre Adélie) and the Islands of Crozet, Kerguélen, New Amsterdam and St. Paul, where France had territorial claims. It was only thanks to international efforts by Austria, Denmark, France, Germany and Switzerland, that the works of EPF in Greenland were succeeded by the new organization *Expédition Glaciologique Internationale au Groenland* (EGIG) founded in 1956, which was to organize expeditions roughly every five years (LeSchack 1964). Four extensive summer expeditions followed the traces of the earlier Swiss and French expeditions. Apart from the main task of (re)measuring the GrIS (Hofmann 1964; Seckel 1977a; Seckel 1977b), there were reconnaissance flights (Bauer 1968b; Bauer & Carbonnell 1968) of the ice margin area and parts of the ice sheet (see also chapter 4.1), as well as measurements of elevation and movement in the terminus area of Eqip Sermia (Bauer 1968a; Bauer & Carbonnell 1968) and the ice margin area of Nunap Kigdlinga (Bauer 1968c). For more information on leveling and velocity data from the EGIG campaigns, refer to chapters 4.4 and 4.5.



*Figure 10*: Leveling measurement of point B-21 by EGIG in 1959 (top) and a similar point of view photographed in 2018 (bottom, Simon Schudel). Historic photo from Bauer (1968c). Note Eqip Sermia in the background: The large lateral moraine visible today more or less marks the ice level of 1959. For the location of the 2018 image, refer to Figure 86 in Appendix C.

### 2.3.3.    W. Zick 1972

After the discontinuation of the EGIG program, German Researchers W. Zick and Prof. Dr. Thyssen visited Eqip Sermia and the Kigdlinga ice sheet margin specifically to re-measure parameters measured by EGIG, such as ice flow velocity and levelings (Zick 1972).

# 3. Background

## 3.1. Other Land-Terminating Ice Margin Research

As stated earlier, much of the land-terminating ice margin research is based on reconstructions for the whole Holocene. Larsen et al. (2016) use eight lake records to reconstruct the Holocene evolution of the Qassimiut lobe in South Greenland. While the Qassimiut lobe does contain some passive land-based ice, it is mostly made up of fast-flowing marine-terminating outlet glaciers. Weidick et al. (2004) also focus on the late quaternary development of the same area, by looking at geological data and paleoclimatic information (ice sheet cores), but both papers make little to no distinction between marine- and land-terminating margins in their results. There is a focus on the Holocene development for land-terminating margins specifically in the papers of Ahlstrøm et al. (2008), Carrivick et al. (2017), Håkansson et al. (2014), Lesnek et al. (2018), Levy et al. (2016) or Mernild et al. (2012).

The Paakitsoq ice margin close to Ilulissat and therefore relatively close to the AOI is an example of such a land-terminating margin studied in detail: Ahlstrøm et al. (2008) assessed the Paakitsoq basin near Ilulissat in light of future ice sheet hydropower potential. However, they focused on producing a new bedrock and surface map of the ice sheet in order to predict the future discharge, rather than studying the historic development of this land-terminating ice sheet margin. This was made up for by Håkansson et al. (2014), who used records of proglacial threshold lakes to look at the retreat of the land-based margin in light of the Holocene climate change. They found that the present-day ice margin position was reached about 6500y ago and has likely remained more or less stable. Currently, a down-wasting of 3.5m/y is measured.

The whole western GrIS margin was studied by Kelley et al. (2012), again with a temporal focus on the whole Holocene. Their study is one of the few with specific information on the retreat of land-terminating ice margins. As Figure 11 shows, distinguishing between land- and marine-terminating ice margins is crucial due to the completely different magnitudes of changes in these areas. In the section where the AOI of this thesis is located, a retreat of about 400m has been measured since the late Holocene Maxima (Little Ice Age, LIA). This is more than the mean retreat of 340m for land-terminating glaciers, but more than the median of 0m (!) for the same group of glacier-margins.
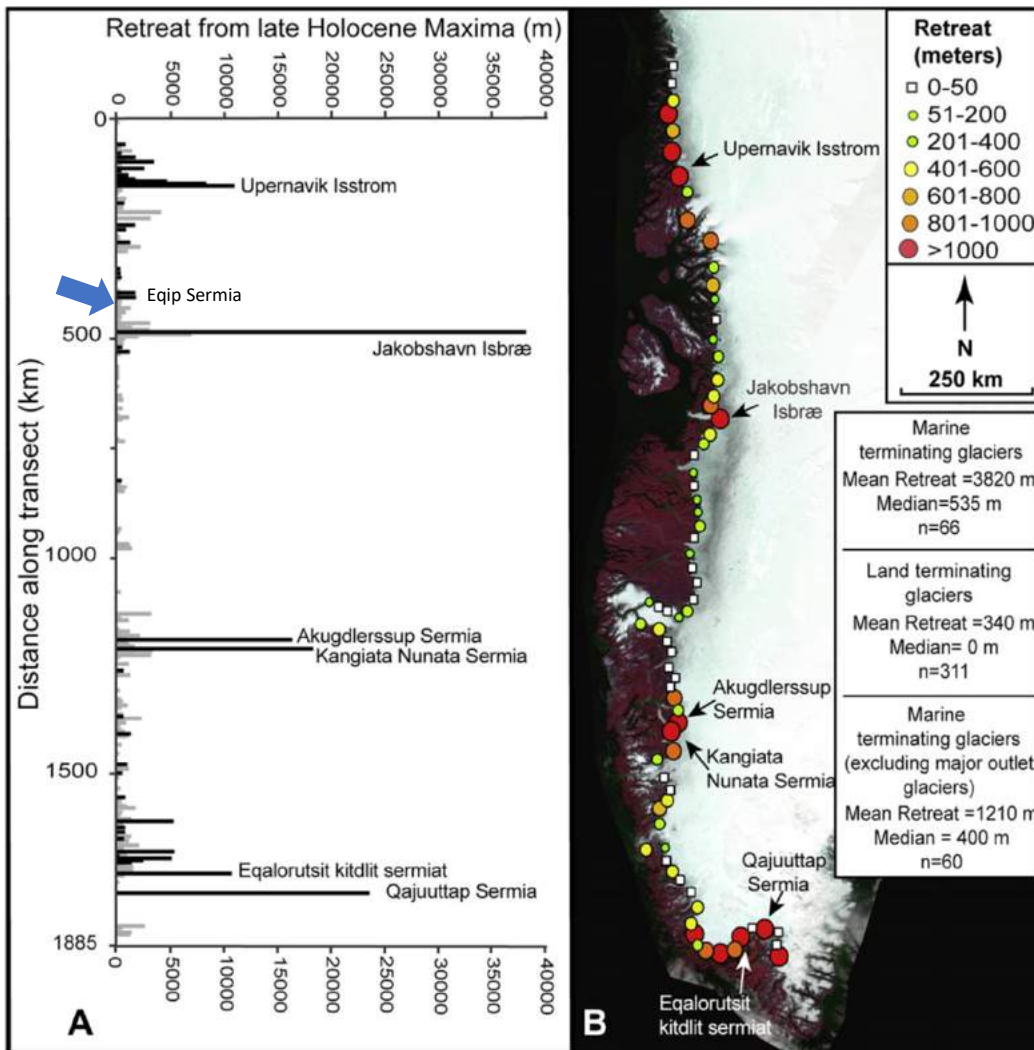
*Figure 11*: (A) Ice-margin retreat measured in western Greenland plotted as distance from the northern end of the survey; large outlet glaciers are labeled; gray bars denote retreat of land-terminating ice margin, black bars denote retreat of marine-terminating ice margins. The blue arrow marks the area of interest in this thesis just south of Eqip Sermia. (B) MODIS image of western Greenland showing average ice-margin retreat from the late Holocene maximum to the 2000s AD. Symbols indicate average retreat over a 25-km-long segment of ice margin, each comprised of 5 individual measurements spaced every 5 km. Adapted from Kelley et al. (2012: 97)

Levy et al. (2016) also make a distinction between land- and marine-terminating glaciers and compute the yearly retreat rates of the early and middle Holocene: In southeastern Greenland the marine-terminating outlet glaciers displayed retreat rates of 70-100 m/y, whereas the terrestrial margins in the Kangerlussuaq region only reached a retreat rate of about 25m/y. Mernild et al. (2012) describe similar differences in modern retreat rates between marine- and land-terminating glaciers in East Greenland between 1971 and 2012. The area studied by Bjørk et al. (2012) is also located in Southeast Greenland. For the 2000-2010 decade they too measured retreat rates about four times higher for the marine-terminating glaciers compared to land-terminating glaciers. However, for all other earlier decades they studied, the retreat rates are very similar (see Figure 12).
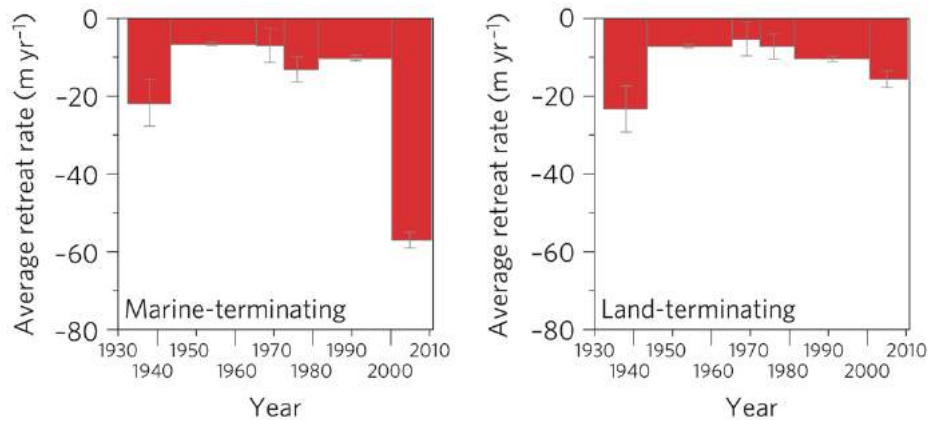
*Figure 12*: *A closer look at marine- and land-terminating glaciers in Southeast Greenland. Frontal changes are shown as rates during six observation periods from 1933 to 2010. Aggregated frontal retreat rates, with measuring uncertainty for each period. Error bars reflect the measuring uncertainty for each observational period. Adapted from Bjørk et al.* (2012)*.*

Sole et al. (2008) went a step further and looked at thinning rates of both selected marine- and land-terminating ice margins in all of Greenland. While they observed a very strong increase in marine-terminating outlet glacier thinning between the 1990s and the 2000s, land-terminating glaciers statistically did not undergo any thinning in the same period. Thus, they came to the conclusion, that the retreat and thinning of marine-terminating glaciers must have been sparked by a controlling mechanism, which has no effect on the land-based ice margins. Holland et al. (2008) describe a large influence of warm subsurface ocean waters on the velocity and thinning rate of Jakobshavn Isbræ.

In terms of velocity of land-terminating ice margins, there is not much specific data. However, some coarse-resolution flow velocity datasets are available for the whole GrIS (e.g. Joughin et al. 2010; Joughin et al. 2015). This dataset yields velocities of about 20m/y between 2017 and 2018 (see Figure 6). The interactions between melt water runoff and ice flow velocity at land-based ice margins were studied by Fitzpatrick et al. (2013), who find that an increase in melt-water leads to an increase in net flux. However, contradicting results were published by Tedstone et al. (2015). They analyzed the influence of melt water on the decadal flow velocities at land-terminating margins in Central West Greenland and came to the unexpected result that increased melt water may actually slow down the velocity on a decadal scale, making these margins even more resilient to climate change than previously thought. On a seasonal time-scale, the velocity of land-terminating margins in West Greenland has been studied by Lemos et al. (2018). They find the velocity to be strongly linked to temperature and recorded speed-ups of up to 32% in summer.

## 3.2.    Digital Elevation Models

A digital elevation model (DEM) is a dataset with the three components Easting, Northing and elevation for each data point. Usually the data points are arranged in a regular grid and are displayed as a raster. The term digital terrain model (DTM) is often used interchangeably, but actually also includes other variables that can be generated from a DEM, namely gradient, aspect, etc. (Bhardwaj et al. 2016; Fisher & Tate 2006). Apart from that, the term DTM is used to set it apart from a digital surface model (DSM). DSMs describe the topmost measurable surface and therefore include all objects on top of the terrain such as vegetation and buildings. DTMs on the other hand only consider the actual terrain altitude, therefore disregarding all cover on top of the terrain (Bhardwaj et al. 2016; Maune et al. 2001), but including ice. Due to the climate and remoteness of the study site, the effect of vegetation or artificial buildings is negligible, which is why the distinction between DTM, DSM and DEM is of no further importance in this study and the terms DTM and DEM may be used interchangeably.

The elevation data needed for DEMs is collected in many different ways, affecting the resulting DEMs greatly (e.g. Eineder & Holzner 2000; Frey & Paul 2012). Measuring elevation has changed over the course of history. While the first scientific elevation data was collected in laborious levelings (e.g. de Quervain & Mercanton 1920), photogrammetry offered a massive simplification of the process. Overlapping optical aerial images could now provide elevation data for large areas at the time.

With the introduction of digital photogrammetric systems in the 1990s, the processing became faster and more efficient given the according metadata (Baltsavias 1999). Unlike the passive optical sensors used for photogrammetry, sensors using RADAR (Radio detection and ranging) or LIDAR (Light detection and ranging) have the advantage of being independent of weather or daylight. Mounting these sensors on satellites or airborne vehicles enabled elevation measurements on a global scale. This diversification of elevational data can create issues of comparability: Rignot et al. (2001) showed that synthetic-aperture Radar (SAR) signals can penetrate ice and snow by 10m and more, which needs to be considered, if compared to a DEM with elevation data of a different source.

With technical improvements an increase in both temporal and spatial resolution was a logical consequence. Satellites enable the gathering of regular elevation footage in unprecedented spatial resolution. This has culminated in datasets such as the ArcticDEM (see chapter 4.3.2), with a temporal resolution of a few months and a spatial resolution of 2m. That is an impressive development considering that in 1996 a DEM of the GrIS with a spatial resolution of 2km was considered 'high resolution' (Ekholm 1996).

## 3.3. Structure from Motion (SFM)

### 3.3.1. Functionality

As the name suggests, SFM is a technique to generate structural data from a moving imaging platform. One of the main advantages of SFM is that it can work solely with optical imagery and that it does not require any camera or ground control information, like it is needed for traditional photogrammetry techniques (Fonstad et al. 2013; Smith et al. 2015). Furthermore, it can be applied to objects of all size: Snavely et al. (2006) have used it to generate 3D models of buildings, while in combination with UAVs it can also be used to generate DEMs of entire mountains (Mertes et al. 2017; Paredes et al. 2017).

To attain a 3D model of an object or a landscape surface, the following steps have to be executed (see Figure 13 for a visualization):

1.  Firstly, the object is photographed from many different angles. For landscape surfaces these can be overlapping aerial images, whereas both oblique or nadir images can be used (Smith et al. 2015). It is important that all images are taken in similar lighting conditions.
2.  An image algorithm, e.g. Scale Invariant Feature Transform (SIFT; Lowe 2004), then determines prominent points on the images, which are ideally identifiable in different scales and image perspectives. This way they can serve as tie points that can be detected and correlated in overlapping images from different angles (Fonstad et al. 2013; Smith et al. 2015).
3.  Using bundle adjustment algorithms, this allows computing the relative distances between the points and the camera positions, while at the same time determining both the intrinsic (e.g. focal length, radial distortion) and extrinsic camera parameters (e.g. X, Y, Z, roll, pitch & yaw). Both the image points and the camera locations can now be placed in a 3D environment: a sparse point cloud including the positions of the imaging platform is generated (Mertes et al. 2017; Smith et al. 2015; Westoby et al. 2012).
4.  If working with a landscape surface, georeferencing is necessary for geoscientific applications. There are different ways of introducing positional data. Either GPS-data values are assigned to visible GCPs on the images (Westoby et al. 2012), or GPS-data is collected of each of the camera positions during the imaging campaign (Turner et al. 2014). A combination of both is also possible and generally more accurate (e.g. Ryan et al. 2015). After the input of georeferencing data, the bundle adjustment can be repeated in order to optimize the image alignment (Smith et al. 2015).
5.  Using Multiview Stereo (MVS) Image Matching, e.g. patch-based MVS (Furukawa & Ponce 2010), other 'non-prominent' image points are also placed in the 3D environment, which results in a dense point cloud (Fonstad et al. 2013; Smith et al. 2015; Westoby et al. 2012).
6.  Now all the points can be connected to form a continuous surface. This can be a mesh (triangulated irregular network, TIN), which is often the final product when working on a 3D model of a small object. With georeferencing and scaling in place, it can also be directly exported to a DEM in raster format (Westoby et al. 2012).

**Step 1**

Overlapping aerial images

**Step 2**

Determining of prominent points (SIFT, left)

Correlation in overlapping images (right)

**Step 3**

Bundle adjustment

Creation of sparse point cloud

Calculation of camera parameters

**Step 4**

Georeferencing

**Step 5**

MVS Image Matching

Creation of dense point cloud

**Step 6**

Export as DEM Raster
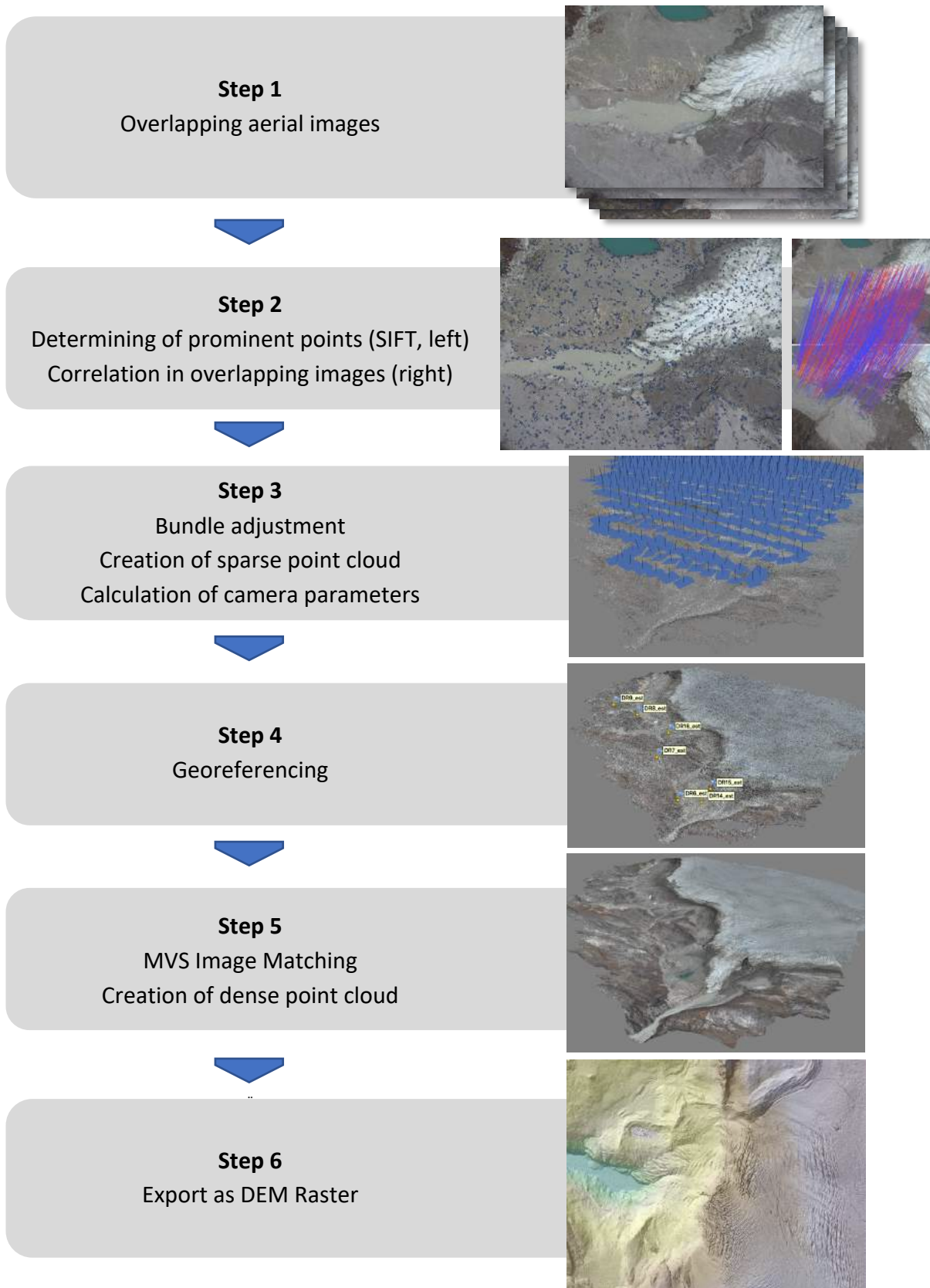
*Figure 13*: *Structure from Motion workflow illustrated with images from the DR16 working process.*

There are often several possible image algorithms for each of the above-mentioned steps. However, popular commercial SFM programs used in geosciences like *Pix4DMapper*, *Agisoft Photoscan* and *Eos PhotoModeler Scanner* are often criticized for being 'black box' programs that do not disclose the algorithms used. They do not allow many individual adjustments in the parameters and lack confirmability (Niederheiser et al. 2016; Smith et al. 2015). Nonetheless, several studies in different circumstances found only minor differences in the results when running the same dataset with *Agisoft Photoscan* and the open-source program *Mic-Mac*, which allows for more direct influence from the author (Burns & Delparte 2017; Jaud et al. 2016; Niederheiser et al. 2016).

### 3.3.2.    Use in Glaciology

The rise of SFM in remote sensing is closely intertwined with the widespread introduction of unmanned aerial vehicles (UAVs, drones) in the 2000s, when their possibilities for mapping and remote sensing in science was starting to be recognized (Bhardwaj et al. 2016).

SFM has been adopted in several scientific disciplines, such as Geomorphology, Glaciology, Hydrology etc. (Smith et al. 2015; Westoby et al. 2012). Glaciology has been especially welcoming for UAV and SFM techniques, due to the often rugged and inaccessible landscapes, as well as the comparably large areas of interest: terrestrial laser scans are both costly and often cannot offer ideal viewing angles, while the combination of UAVs and SFM provides a fast, comparably cheap and effective alternative for data collection (Westoby et al. 2012). The high resolution possible with this technique also gives it an advantage compared to satellite data: In Svalbard or in Antarctica for example, the share of environmental remote sensing studies (published before 2015) where UAVs were utilized, is already exceeding 25% (Bhardwaj et al. 2016).

Typical applications of SFM in glaciology include monitoring glacier dynamics both for alpine valley glaciers (e.g. Immerzeel et al. 2014; Rossini et al. 2018) and marine-terminating glaciers (e.g. Jouvet et al. 2017; Ryan et al. 2015). SFM is used to generate DEMs and orthophotos (e.g. Solbø & Storvold 2013) as well as for surface mapping (e.g. Kraaijenbrink et al. 2016) and has also been applied to historical aerial and terrestrial images in the context of glaciology and in consequence for the calculation of surface elevation changes using DEM differencing (e.g. Denzinger 2018; Mertes et al. 2017; Mölg & Bolch 2017).

## 3.4.    Melt Modelling

Glacier melt is complex, and many parameters play a role. To model glacier melt, there are generally three common approaches. The Energy Balance Model (EBM), Temperature Index Model (TIM) and Enhanced Temperature Index Model (ETIM). The EBM is based on physical equations describing the energy balance at the glacier surface (see Equation 1). The assumption is that the difference between the energy going into the glacier and the energy going out of the glacier describes the melt (Arnold et al. 1996; Braithwaite 1995; Braithwaite & Olesen 1990).

$$Q_{melt} = SW_{in} + SW_{out} + LW_{in} + LW_{out} + Q_{sens} + Q_{latent} \qquad \textit{Equation 1}$$

$SW$ stands for the short-wave radiation. The relation between $SW_{in}$ and $SW_{out}$ is determined by the albedo. $LW$ stands for the long-wave radiation. $Q_{sens}$ describes the turbulent sensible heat flux, while $Q_{latent}$ describes the turbulent latent heat loss (caused by evaporation). Some of these values cancel themselves out and whatever is left is available for melt ($Q_{melt}$). If this value turns out to be negative, it describes the geothermal flux of cooling ice.

The TIM on the other hand is an empirical model based on the assumption that there is a linear relation of air temperature and the melt rate (see **Equation 2**). The most common TIM used is the Positive Degree Day Model (Hock 2003; Braithwaite 1995).

$$melt = MF \cdot \sum_{t1}^{t2}(T_{air} - T_T) \qquad for\ T_{air} > T_T \qquad \textit{Equation 2}$$

$MF$ stands for melt factor, has the unit of md$^{-1}$C$^{-1}$ and hence describes the melt in m per one degree air temperature per day. In order to calculate the melt, this melt factor is multiplied with the cumulative mean daily temperature above a threshold temperature $T_T$. This is the temperature where melt is assumed to start. Usually this is 0°C but may differ depending on the application.

The third commonly used model (ETIM) was developed by Pelliciotti et al. (2005) and combines elements of both previous models. It is essentially a TIM that includes information about shortwave radiation and the albedo (see **Equation 3**). $SWF$ stands for a Shortwave Factor, $\alpha$ for the albedo.

$$melt = \sum_{t1}^{t2} MF \cdot (T_{air} - T_T) + SWF(1 - \alpha) \cdot SW_{in} \qquad for\ T_{air} > T_T \qquad \textit{Equation 3}$$

# 4. Available Data

## 4.1. Aerial Imagery

There are several sources of aerial imagery for Greenland throughout the last century and they are all centrally collected in the so-called *AirBase* database by the Danish Agency for Data Supply and Efficiency (*Styrelsen for Dataforsyning og Effektivisering* – SDFE, previously Geodetic Institute, then National Cadaster and Survey of Denmark, and Danish Geodata Agency) (Korsgaard et al. 2017). However, not all of the images known to exist are yet accessible through the SDFE. There are several possible explanations for this including misplacement, mislabeling or not being indexed and scanned yet. An overview of all known aerial images is presented in **Table 1**.

*Table 1*: *Overview of the aerial images available for Eqip Sermia (ES), Nunap Kigdlinga (NK) and Sermeq Kujalleq (SK). Note that the images of 1953 were provided by A. Bjørk from the SDFE, but apart from a mention in Bauer* (1968a) *no records of these images were found.*

| Year | Exact Date | Source | Coverage (ES/NK/SK) | View of direction | High resolution available |
|------|-----------|--------|---------------------|-------------------|---------------------------|
| **1949** | 18.07.1949 | Hansen (1968) | ES, NK, SK | oblique | No |
| **1953** | 03.07.1953 | SDFE | ES | nadir | Yes |
| **1957** | 07.07.1957 | Bauer (1968b) | ES | nadir | Yes |
| | 07.07.1957 | Bauer (1968b) | NK, SK | nadir | No |
| | 12.07.1957 | Bauer (1968b) | ES | nadir | Yes |
| | 14.07.1957 | Bauer (1968b) | NK, SK | nadir | No |
| | 17.07.1957 | Bauer (1968b) | ES | nadir | Yes |
| **1958** | 15.07.1958 | Bauer (1968b) | ES | nadir | No |
| | 18.07.1958 | Bauer (1968b) | NK, SK | nadir | No |
| **1959** | 25.06.1959 | Bauer (1968a) | ES, NK, SK | nadir | Yes |
| **1964** | 29.06.1964 | Bauer & Carbonnell (1968) | ES (NK, SK?) | nadir | No |
| | 12.07.1964 | Bauer & Carbonnell (1968) | ES, NK, SK | nadir | Yes |
| **1985** | 09.07.1985 | Korsgaard et al. (2017) | ES, NK, SK | nadir | Yes |

Hansen (1968) includes an aerial image from the 18th of July 1949 (see Figure 14) in his publication on glaciogeological and sedimentological research at Eqip Sermia and Nunap Kigdlinga. This is the earliest known aerial image of the area, but the original negatives are currently not available. Generally, the terminus of Eqip Sermia is more regularly covered than the ice margin. The first image available in high resolution was taken on 3rd of July 1953 by the SDFE, while

the EPF expedition of the same year still relied on terrestrial leveling to determine the position of the Eqip Sermia terminus (Bauer 1955). In 1957/58 EGIG produced aerial images of Eqip Sermia and other glacier termini of Western Greenland (Bauer 1968b). In those campaigns, there were also flights covering the Nunap Kigdlinga ice margin area. Unfortunately, the original images of both the film roll *MV2* of the reconnaissance flight on the 7th of July 1957 as well as the film roll *MV107* of the detailed aerial survey on the 15th of July 1958 (Bauer 1968b) are nowhere to be found at the SDFE, where all the other images of these campaigns are stored today. Thus, the first high-resolution aerial imagery of Nunap Kigdlinga and Sermeq Kujalleq available was acquired on the 26th of June 1959 as part of a larger surveyed area including Eqip Sermia terminus (Bauer 1968a). The data of this flight was used in this thesis to generate a DEM through SFM (see chapter 5.3.1). Another flight of the whole area was conducted by EGIG in 1964 (Bauer & Carbonnell 1968). Unfortunately the image overlap in the area of Nunap Kigdlinga and Sermeq Kujalleq was insufficient in order to create a digital elevation model, but it was used to delineate the ice extent (see chapters 5.9 and 6.1).

During the years of 1978, 1981, 1985 and 1987, the SDFE carried out aerial surveys of the whole non-glaciated areas of Greenland including the ice-margins. The study site of this paper was covered in 1985. Korsgaard et al. (2016) used this imagery to create the AeroDEM (see chapter 4.3.1).



**Figure 14**: *Earliest known aerial image of Eqip Sermia, Nunap Kigdlinga and Sermeq Kujalleq, taken by the Geodætisk Institut (now SDFE) on 18th of July 1949 facing East. Image from Hansen* (1968: 307).

## 4.2.   Satellite Imagery

The first satellite imagery of the area stem from US army observation satellites (Corona, Argon, Lanyard – KH1-4), which in the meantime has been declassified (USGS 2008). Later, the LANDSAT mission started delivering the first regular imagery, starting with Landsat 1 in 1972 (USGS 2016). However, it was only with the ASTER instrument, that the spatial resolution reached a useful level (pixel size of 15x15m) in order to be considered in this thesis. This data was used to determine the retreat lines of Sermeq Kujalleq starting in 2003 (see chapter 5.9). About 5 years ago ASTER was again surpassed by instruments with a higher spatial resolution, such as the Sentinel satellites of the European Copernicus program (European Commission 2015).

## 4.3. Existing DTMs

In this chapter, an overview of the existing ready-to-use DEMs of the study site is presented. Because the main aim of this study is change detection, only snapshot DEMs (DEMs with a single time stamp) are considered. Composite DEMs computed from a series of data from different points in time, such as the GimpDEM (Howat et al. 2014), AsterGDEM2 (Slater et al. 2011; Tachikawa et al. 2011), SPIRIT-DEM (Korona et al. 2009), WorldDEM™ (Airbus Defence & Space 2018) as well as the ALOS PRISM 3D (EORC & JAXA 2018; Tadono et al. 2014) were therefore disregarded. Additionally, only high-resolution DEMs were considered, since that is a necessity with such a small study site. This was an issue with other ready-to-use DEMs, such as the Viewfinder Panorama DEM (De Feranti 2014) or the TanDEM-X by the DLR (Bartusch et al. 2009). An overview is presented in Table 2.

*Table 2: Overview of the most common ready-to-use DEMs (ordered alphabetically). Marked in orange are factors that lead the dataset to be disregarded in this study* (Airbus Defence & Space 2018; Bartusch et al. 2009; De Feranti 2014; EORC & JAXA 2018; Frey & Paul 2012; Howat et al. 2014; Korona et al. 2009; Korsgaard et al. 2016; NGA & NSF 2018; Slater et al. 2011; Tachikawa et al. 2011; Tadono et al. 2014)*. The GimpDEM is marked with a (\*) because it is a composite, but due to the interesting time frame it covers, it was considered nonetheless. SPOT-DEM (\*\*) on the opposite fulfilled all requirements, but the available dataset only covered the year 2014, for which there are ArcticDEM scenes with much higher resolution.*

| Dataset Name | Resolution | Composite/Snapshot | Study site coverage |
|---|---|---|---|
| AeroDEM | 25m | Snapshot | Yes |
| ALOS PRISM 3D | 30m | Composite | Yes |
| ArcticDEM | 2m | Composite/Snapshots | Yes |
| ASTER Snapshot DEMs | 30m | Snapshot | Yes |
| AsterGDEM2 | 30m | Composite | Yes |
| GimpDEM* | 30m | Composite | Yes |
| SPIRIT-DEM | 40m | Composite | Yes |
| SPOT-DEM** | 40m | Snapshot | Yes |
| SRTM DEM | 30m | Snapshot | No |
| TanDEM-X | 90m | Composite | Yes |
| ViewfinderPanorama DEM | 100m | Composite | Yes |
| WorldDEM™ | 12m | Composite | Yes |

### 4.3.1. AeroDEM

Korsgaard et al. (Korsgaard et al. 2016) published a DEM of the entire ice-free areas as well as most of the GrIS margins of Greenland. It is based on aerial photographs from 1978 to 1987 and was created using BAE System's digital photogrammetric application SOCET SET. Different GCPs as well as altimetry data, acquired by the *Geoscience Laser Altimeter System* (GLAS), which is onboard the ***I****ce,* ***C****loud and* ***L****and* ***E****levation* ***Sat****ellite* (ICESat), was used to correct and co-register the dataset. The DEM is provided in a resolution of 25x25m. The aerial images of the study area of Nunap Kigdlinga and Sermeq Kujalleq used for the AeroDEM stem from flights in 1985 (see chapter 4.1), which is the reason this dataset will be referred to as AE85 from now on in this thesis. Along with the DEM, Korsgaard et al. (Korsgaard et al. 2016) also published a reliability mask, roughly identifying points that were generated using photogrammetry and points that were interpolated. Unfortunately, only a narrow strip of ice close to the margin consists of reliable, photogrammetrically calculated data points, whereas large areas further up the ice sheet, especially in the Nunap Kigdlinga area, consist of unreliable, interpolated data points (see also chapter 5.6.2).

### 4.3.2. ArcticDEM

The ArcticDEM (Porter et al. 2018) is a relatively new product of the collaboration of the National Geospatial-Intelligence Agency (NGA) and the National Science Foundation (NSF) of the United States with an unprecedented coverage and spatial resolution in the Arctic. As Morin et al. (2016: 1) put it, the new dataset *"… catapult[s] the Arctic from the worst to among the best mapped regions on Earth"*. The entire land area of the Arctic north of 60° latitude, as well as the entire areas of Alaska, Greenland and Kamchatka is covered by a composite DEM mosaic with a very high spatial resolution of 2m. It is based on optical stereo imagery from the polar-orbiting Worldview-1, 2 and 3 satellites (*DigitalGlobe*) from the years of 2010 to 2017. These images were then photogrammetrically processed with TIN-based Search-space Minimization (*SETSM*) software (Morin et al. 2016; NGA & NSF 2018). This dataset offers many new opportunities and the ArcticDEM has already been utilized in several publications, such as Candela et al. (2016), Dai et al. (2018) or Dai & Howat (2017).

Composite DEMs are not very suitable for change detection over time, because they are made from data acquired throughout a longer time span. Luckily, the producers of the dataset acknowledge this by providing the individual time-stamped DEM sets ('strips') that make up the final composite DEM. The newest release of the dataset (released on 28th of September 2018) not only provides higher spatial resolution for the composite DEM, but also new time stamps (NGA & NSF 2018). From now one, the composite ArcticDEM will be referred to as 'ADcomp', while the individual snapshots will be referred to as 'ADYY', whereat 'YY' stands for the year of acquisition.

ADcomp is registered to ICESat altimetry data. However, the individual time-stamped DEMs only contain metadata describing the x-, y- and z-offsets, without actually having been translated (NGA & NSF 2018). This is later compensated by co-registering them to the composite DEM (see chapter 5.5).

### 4.3.3.  ASTER Snapshots

Apart from tiles of the AsterGDEM mentioned earlier, the EarthData Search Engine by Nasa also allows for downloads of snapshot DEMs (U.S./Japan ASTER Science Team 2007). These DEMs are photogrammetrically generated using the nadir-viewing and backward-viewing Bands 3 of an ASTER image acquired by the Visible Near Infrared (VNIR) sensor and finally provided as an orthorectified DEM. There is no weather evaluation done and many scenes contain a lot of artefacts caused by clouds, water surfaces etc. The available images were therefore individually checked in order to select usable scenes. From a total of 197 scenes covering (at least partly) the area of interest, 25 scenes were downloaded for closer inspection. Based on quality and temporal coverage, three scenes were selected for this paper: One from 9th of June 2003, one from 9th of July 2010 and one from 7th of July 2016 (from now on they will only be referred to as AS03, AS10 and AS16 respectively).

### 4.3.4.  GimpDEM

The GimpDEM was created by Howat et al. (2014) as part of the Greenland Ice Mapping Project (GIMP). The goal was to improve the spatial resolution of existing DEMs and achieve better results, especially in the ice margin areas of the GrIS. To do so, several existing datasets were combined, such as the Photo-enhanced Bamber DEM (Bamber et al. 2001; Scambos & Haran 2002), the ASTER GDEM2 (Slater et al. 2011; Tachikawa et al. 2011) or the SPIRIT DEM (Korona et al. 2009). The latter two are also listed in Table 2. All this data was then referenced to ICESat altimeter data obtained in the years 2003 to 2009, which makes this DEM a temporal composite with all the limitations associated with such a dataset. Howat et al. (2014: 1512) also state that they *"… focus on generating a continuous surface and … ignore temporal changes in ice elevation"*. Due to the fact that the time between 2003 and 2009 turned out to be a very interesting period with profound surface elevation changes, it was decided to nonetheless consider this dataset. The dataset will be referred to as GD0309 from now on.

### 4.4.  20th Century Levelings

After the first levelings of 1912 by de Quervain & Mercanton (1920), there were several more by the EPF and EGIG expeditions, as well as in 1971 by Zick (1972). Especially the French expeditions have generated enormous amounts of data and it is difficult to keep the overview, since sometimes the coordinates and the altitude data is not of the same time and not published in the same report. Table 3 gives an overview of the available data. Obviously only data where both positional and elevation information were collected at the same time were considered for this thesis (namely 1912, 1948, 1952, 1953, 1959 & 1971).

*Table 3*: *Overview of the 20th century leveling data in the Nunap Kigdlinga and Sermeq Kujalleq area.*

| Year | Points in AOI | Source for coordinates | Source for altitude |
|------|---------------|------------------------|---------------------|
| **1912** | 19 | de Quervain & Mercanton (1920) | de Quervain & Mercanton (1920) |
| **1948** | 9 | Bauer (1968c) | Bauer (1968c) – only 4 points |
| **1950** | 9 | - | Tschaen (1959) |
| **1952** | 2 | Bauer (1968c) | Bauer (1968c) |
| **1953** | 1 | Bauer (1968c) | Bauer (1968c) |
| **1959** | 7 | Bauer (1968c) | Bauer (1968c) – only 4 points |
| **1968** | 5 | - | Seckel (1977a) |
| **1969** | 4 | - | Bauer (1968c) |
| **1971** | 4 | Zick (1972) | Zick (1972) |

This leveling data is used to complement the planar elevation data of the DTMs, especially in times, when there is no DTM available. In one instance (1959), leveling information is also used to better fit the DTM to the measured elevations (see chapter 6.4.2). An overview of all existing elevation datasets as well as the newly generated DTMs within this thesis are displayed in Figure 15.
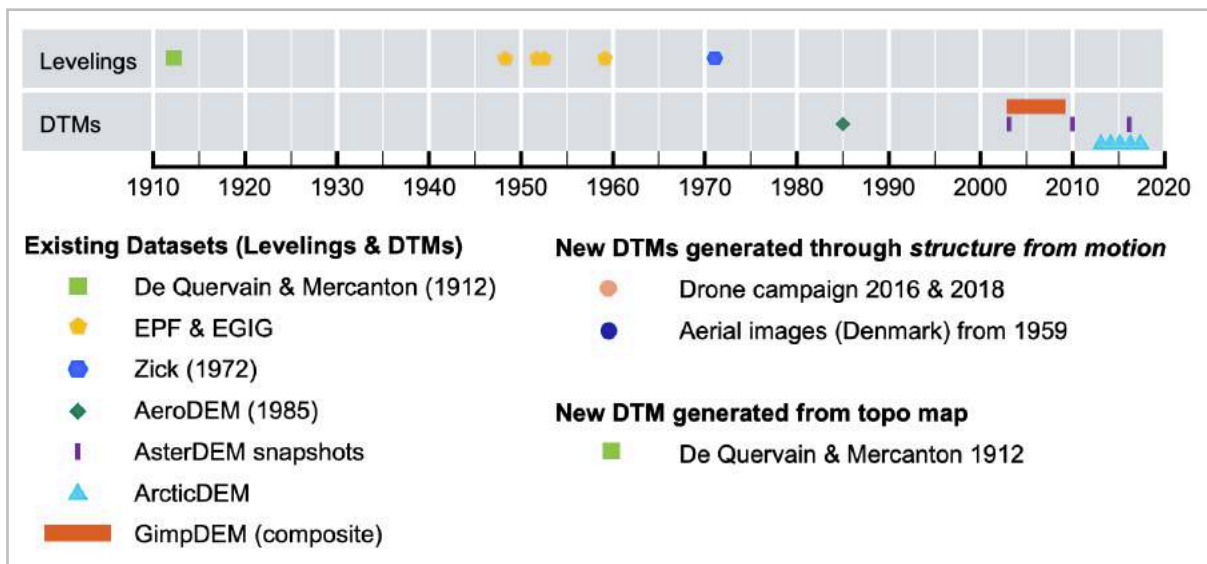


*Figure 15*: *Overview of the available elevation data in the time between 1912 and 2018. The creation of the new DTMs listed on the right will be explained in detail in chapters 5.2.2, 5.3.1 and 5.4.*

## 4.5.     Velocity Data

For the Eqip Sermia outlet glacier terminus, there are quite regular velocity measurements over the years. Lüthi et al. (2016) provide a detailed list. In-situ measurement data is a bit sparser for the ice sheet margin. De Quervain & Mercanton (1920) also included velocity values in their topographic map of Nunap Kigdlinga and Sermeq Kujalleq of 1912. Later, the EGIG missions determined the location and elevation for several control points across the whole ice sheet. These levelings were undertaken in 1948, 1959 and 1968. For the period between 1948 and 1959 velocity values have been calculated (Bauer 1968c). Unfortunately for the 1968 measurements only the elevations are provided (Seckel 1977a; Seckel 1977b), but not the coordinates, which does not allow the retrieval of velocity data (see also Table 3). The points in proximity to the ice margin were later repeated by Zick (1972), who calculated velocities between 1959 and 1971. Later velocity data is inferred from satellite or aerial images (see chapter 5.10).

## 4.6.     Climate Data

For the AOI there are no direct long-term measurements available. The Department of Geography of the University of Zurich (GIUZ) runs several Automated Weather Stations (AWS) in the area of Eqip Sermia and Eqi Camp. Especially interesting for this research is the station at the ice-margin of Eqip Sermia, due to similar elevation and surroundings in comparison to the AOI of this research. Air temperature [°C], precipitation [mm], relative humidity [%], Wind [m/s] as well as wind direction [°] are measured parameters (Walter 2016). These parameters are measured at about 1.5m above ground. Available data include the years 2014 and 2018.
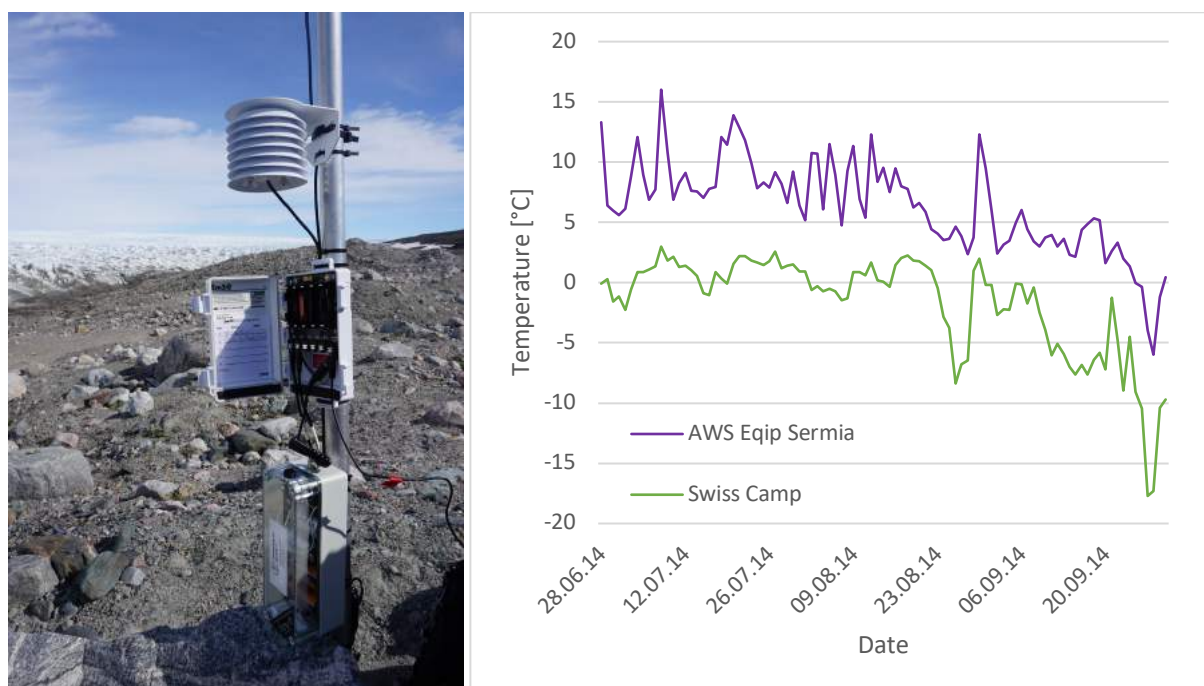


*Figure 16*: *Automated Weather Station run by the GIUZ at the Eqip Sermia ice margin (left). Comparison of the available datasets in daily temporal resoultion. Displayed is a period of three months in 2014 (right).*

For long-term weather data, the closest station is located about 70km in Southwest direction in Ilulissat (see Figure 17). It is run by the Danish Meteorological Institute (DMI). Three different stations (1873-1960, 1961-1992, 1991-today) ensure a consistent series of measurements dating back almost 150 years (Cappelen 2018). For this research the dataset with monthly average temperatures was used (Dataset ID: gr_monthly_all_1784_2017: 4221). Due to the proximity of this station to the ocean, this data obviously experiences large oceanic influences which may not be present at the ice margin (see Figure 18).

The opposite is true for the data at the Swiss Camp, the closest weather station on the ice sheet (see Figure 17). It is located at about 1100m.a.s.l. and is part of the Greenland Climate Network (GC-NET), providing daily temperature data since 1995 (Box & Steffen 2000).

Another source for temperature data used in this research is Box (2013). He generated a gridded 5x5km dataset for the whole GrIS with reconstructed climatic surface mass balance as well as air temperatures (near-surface) by combining meteorological station records, ice cores and regional climate model outputs. For this research, the output for the same location as in Lüthi et al. (2016), which were generated for Eqip Sermia, was used.
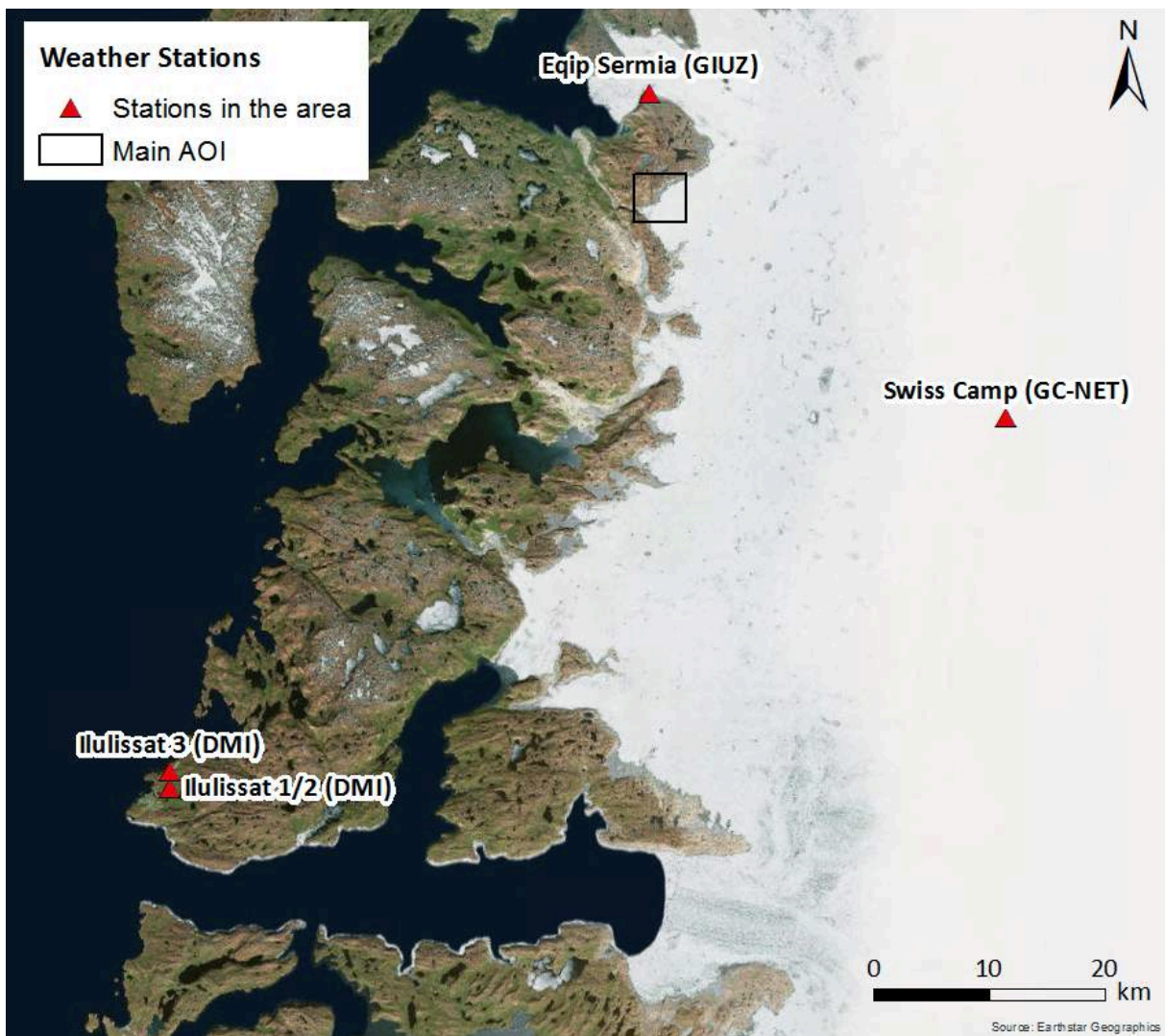


**Figure 17**: Locations of the weather stations in the area, which were used for this thesis.
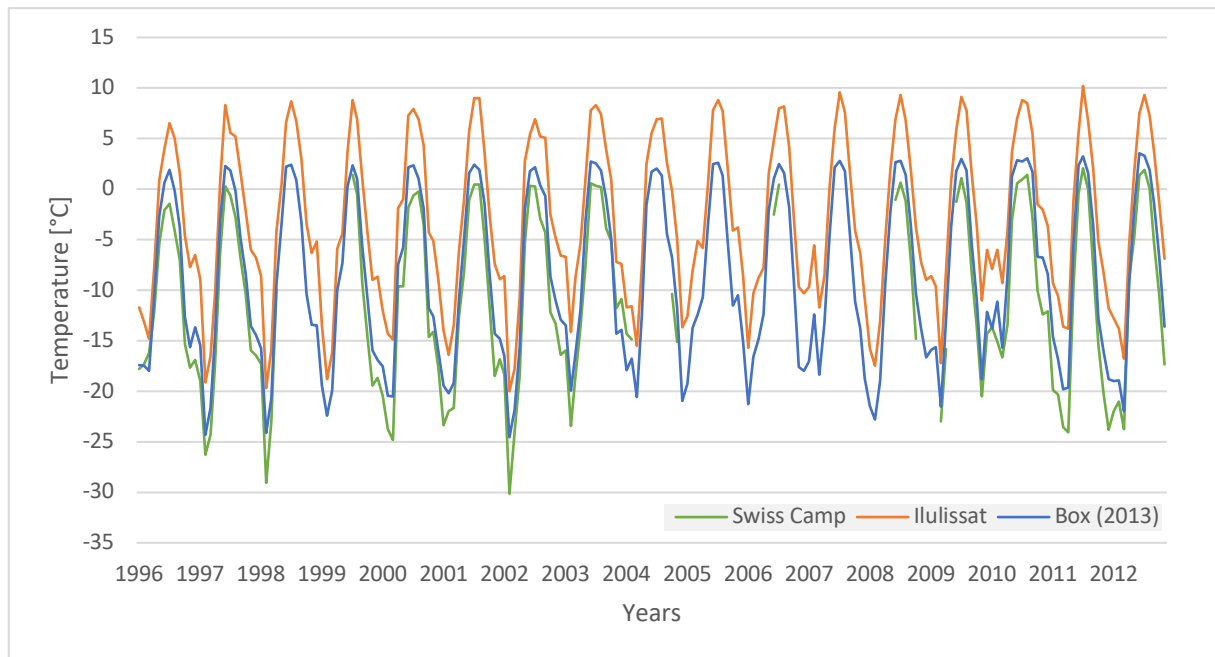
***Figure 18****: Comparison of monthly averages of the available long-term temperature datasets.*

# 5. Methods

Apart from the existing data presented in chapter 4, data from a 2016 field campaign was also available. The most current data was gathered in the 2018 fieldwork between July 2$^{nd}$ and July 16$^{th}$ 2018, which was conducted as part of a larger research campaign with several researchers from the GIUZ, as well as the Laboratory of Hydraulics, Hydrology and Glaciology (VAW) of the Swiss Federal Institute of Technology (ETHZ). Tents and an old hut from the EGIG expeditions served as a basecamp (see Figure 93 in Appendix C). The Eqi Tourist Camp also located at this site does not only have geographical ties to the research history of this area: A grandson of a Greenlandic member of the de Quervain expedition of 1912 (de Quervain & Mercanton 1920) is an employee at the camp today.

A drone flight delivered the aerial imagery needed to create a high-resolution DTM with the help of SFM. Other important data collected in 2018 includes differential GPS measurements of ground control points. Some of them were artificially placed on the ice sheet, while prominent features in the landscape, such as large, stable boulders, were used as control points in non-glaciated areas. Last but not least, historical reference points from de Quervain & Mercanton (1920) as well as the EPF/EGIG expeditions (Bauer 1968c), were re-measured in order to provide calibration data.

## 5.1. Workflow Overview
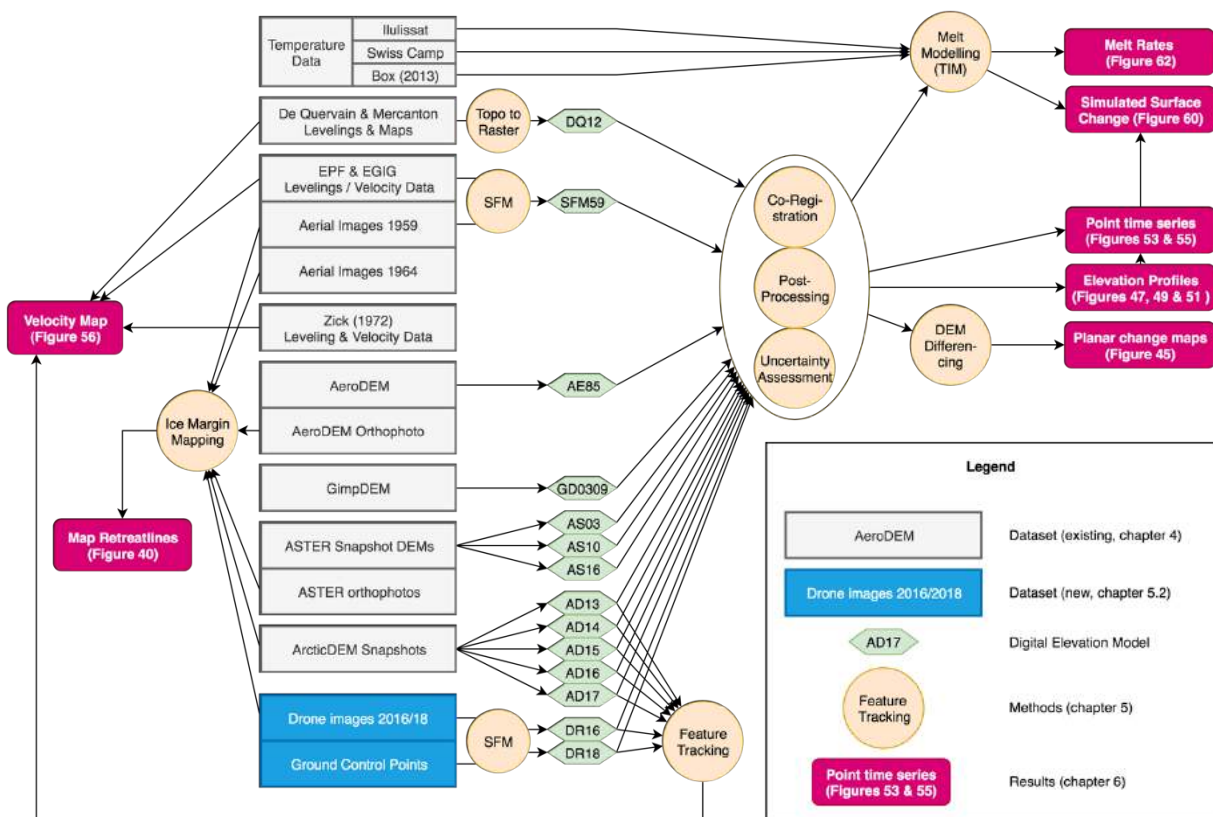


***Figure 19****: Simplified overview of the thesis workflow (generated using draw.io). An enlarged version is available in Appendix E.*

As Figure 19 shows, the main tasks of this thesis are connected to the generation, alignment, comparison and assessment of DEMs. Other work includes the generation of the ice flow velocity map and the map of the Sermeq Kujalleq retreat lines.

## 5.2. Drone Data

The choice of drone depends mostly on the flight range as well as the camera specifications. Only fixed wing drones achieve velocities high enough to cover areas as large as this projects' area of interest. It is important that all images of one survey are taken within a short time period, in order to avoid changing conditions in terms of sunlight, cloud cover, meltwater, etc. Hence the goal was to cover the whole area of interest in one flight. In 2016, an *eBee* drone was used to conduct the survey, while an *X8 Skywalker* drone was used in 2018.

*Table 4*: Specifications of the two drones used for this paper. Images by Simon Schudel (2016, 2018).

| | eBee (2016) | X8 Skywalker (2018) |
|---|---|---|
| **Picture** |  |  |
| **Wingspan** | 1 m | 2 m |
| **Weight** | 0.7 kg | 5 kg |
| **Max. flight duration** | 50 min | 4 hours |
| **Max. flight distance** | 33 km | 200 km |
| **Camera** | Sony DSC-WX220 (Sony Lens G) | Sony Alpha 6000 (16mm pancake lense) |

In 2016, the flights were planned and executed by Prof. Dr. Andreas Vieli. Due to the limited range of the eBee drone, five individual flights were necessary in order to cover the whole study site. The flights covered a total distance of about 90 km with take-offs and landings at the site. The pictures were taken from an average altitude of 1100 m.a.s.l. (the altitude was adapted depending on ground altitude and was always 500m above ground).

The X8 Skywalker drone (see e.g. Jouvet et al. 2017), provided and operated by Dr. Guillaume Jouvet, and used in 2018, has a higher velocity and longer max. flight duration, which allowed for the whole area of interest to be surveyed in one single flight with take-off and landing directly at the basecamp. The total flight time was about 3 hours. In total, a distance of about 150 km was covered. The pictures were taken at an average overlap of 70% side-wise and 95% in the direction of the flight from an altitude of 800 m.a.s.l.. Unlike in 2016, the altitude was kept constant throughout the flight, which leads to quite varying image overlap percentages in areas of low terrain and areas of high terrain (see Figure 20, bottom right). A higher flight

altitude would have technically been possible, but it was kept at 800 m in order not to conflict the air traffic as well as the drone flight permission granted by the Greenland air traffic authority. The drone used in 2018 even had a differential GPS receiver (see also 5.2.1) on board, providing accuracies in the range of centimeters when georeferencing the camera locations. This is an important addition to the available input variables, which has not been available until very recently (James et al. 2017).
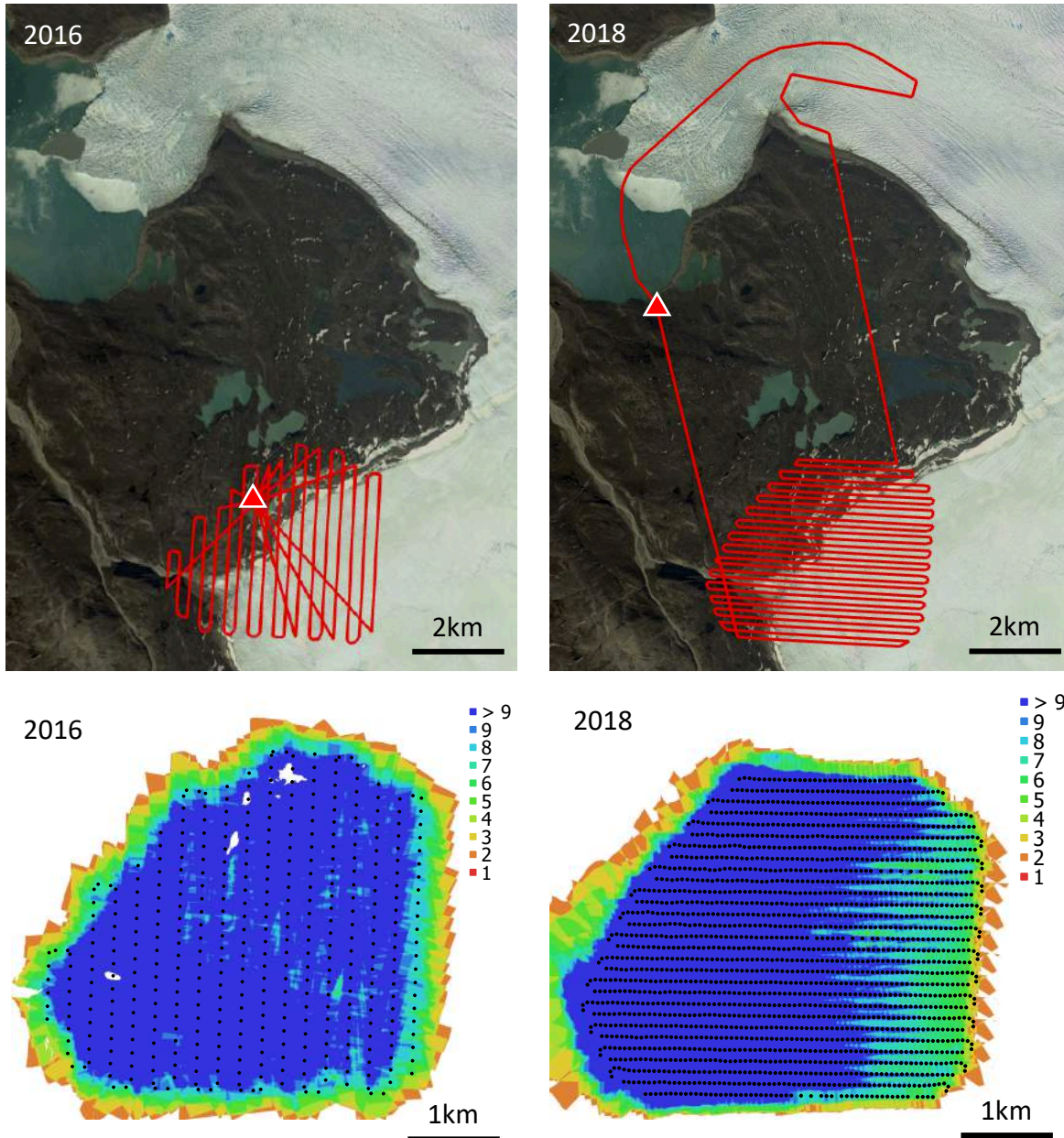


*Figure 20*: *Preliminary flight plans of 2016 and 2018. The red triangles mark the spot of take-off and landing. With data from Google Earth* (2018) *(top). Camera locations and image overlap as presented in the* Agisoft Photoscan *reports (bottom).*

### 5.2.1. Ground Control Points (GCPs)

Unfortunately, there were no ground control points (GCPs) measured in 2016. However, in 2018 the area of interest was dotted with eleven control points, which were spread out across the whole extent (see Figure 21 or Figure 24).
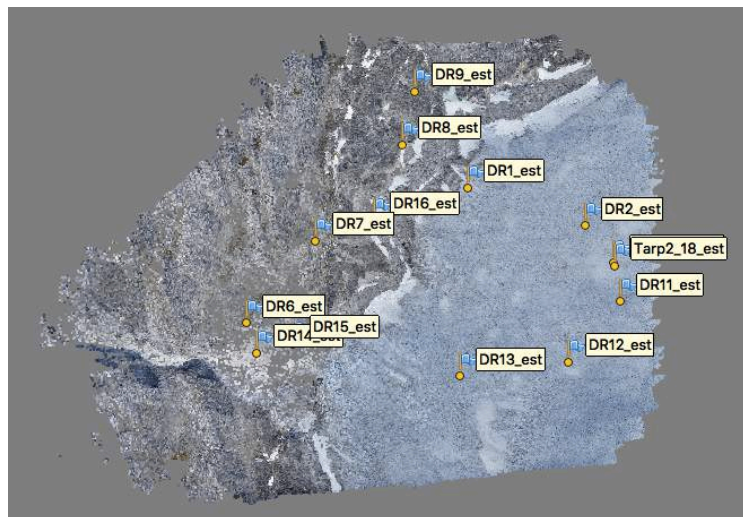


*Figure 21*: *Screenshot of a nadir view of the sparse point cloud of the 2018 data including GCPs in* Agisoft Photoscan.

On the ice sheet, the GCPs consisted of distinctive green tarps with an area of around 1.5m$^2$. They were measured in the center with a Leica GPS SR-530 (GPS antenna 302). For the control points in the non-glaciated areas, prominent stable-terrain features, such as large boulders were pre-selected before the fieldwork using a preliminary orthophoto from the 2016 drone images. This ensured that the selected points would be well visible from the bird's eye view. These points were then located in the field, checked for the stable-terrain criterion before being measured again using the Leica GPS SR-530. Processing the drone data in SFM, this positional data provided control points for both the 2016 and the 2018 drone DTMs. This approach was chosen to enhance the comparability of the two drone DTMs despite the fact that there were no ground control points measured in 2016.

In order to get the most accurate measurements possible, the GCPs were measured with a differential GPS. This technique is characterized by two measurement devices running simultaneously. The first device is the base-station and is not moved during the whole measurement campaign. Due to the long measurement period (several hours), the exact position of this station is known, which allows the station to determine slight biases between the continuous pseudo-range measurements and the computed geometric range. These small biases are caused e.g. by ionospheric and tropospheric delay, receiver noise or receiver clock offsets. The second device is used as a rover and all the points of interest are measured with this device. In post processing, the rover measurements can then be corrected for pseudo-range measurement errors using the base-station measurements (Kaplan & Hegarty 2006). The positional data of the GCPs can then be differentially processed, which in this case yielded accuracies in the range of cm. Unfortunately, the base-station at Eqi Camp (see Figure 1 for location and Figure 22 for photo) encountered a malfunction leading to a gap in the reference data. The affected GCPs (DR8, DR9, DR11, DR12 and DR13, see Figure 21) in consequence only yielded accuracies of 3 - 6m.

### 5.2.2. SFM Processing in *Agisoft Photoscan*

The original drone photos and the exact positional information about the camera (2018) were the only input data used to start the process (see also 3.3.1). The initial alignment was done in the setting of 'high accuracy' for both datasets with enabled generic preselection and reference preselection. The latter takes the positional data of the camera position (if available) into account for the alignment, which is a way to accelerate the process but does not have any other effect on the output data. The resulting sparse point clouds consisted of 256'934 tie points (2016) and 828'511 tie points (2018) respectively (see Table 5).



*Figure 22: The base-station of the differential GPS measurements at Eqi Camp.*
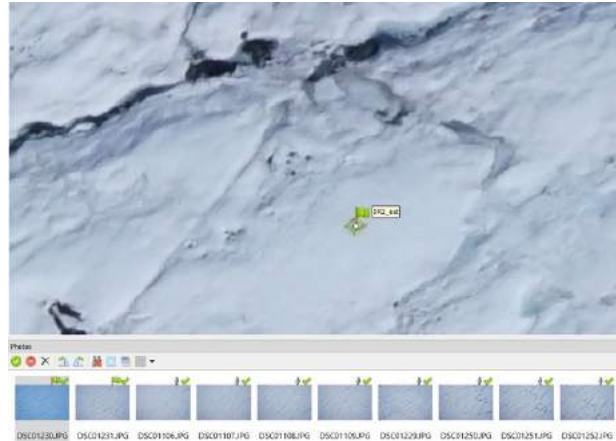


*Figure 23: Marking GCPs in the original drone images of 2018 (*Agisoft Photoscan *Screenshot)*

In a next step, the GCPs were marked on all images, where they are visible (see Figure 23). Doing so after the initial alignment is much faster and easier, because after placing the first marker, the software can estimate the location of the marker on all other images used for alignment. For the marker positions on these other images only minor adjustments are necessary. The marked GCPs were then attributed with the exact coordinates and expected errors attained by the differential GPS measurements and processing.

*Agisoft Photoscan* offers the possibility to optimize the camera alignment by taking into account the positional information of the GCPs. Both the estimated point cloud and the estimated internal and external camera parameters are altered in this step. This offers a possibility to remove possible non-linear deformations (Agisoft LLC 2018). However, as a consequence of the relatively high uncertainty of some GCPs, this uncertainty translates into the DEM, if the camera alignment is optimized according to them. As you can see in Figure 24, there is a clear relation between the uncertainty of the GCPs and the resulting DEM with optimized camera alignment. In case of 'DR12' this means for example, that the difference between a DEM generated without camera alignment optimization and a DEM generated with camera alignment optimization is around 7m. It was therefore decided, not to optimize the camera positions before generating the DEM from the dense point cloud. The resulting root mean square error (RMSE) of the generated model in respect to the GCPs is described in Table 5.
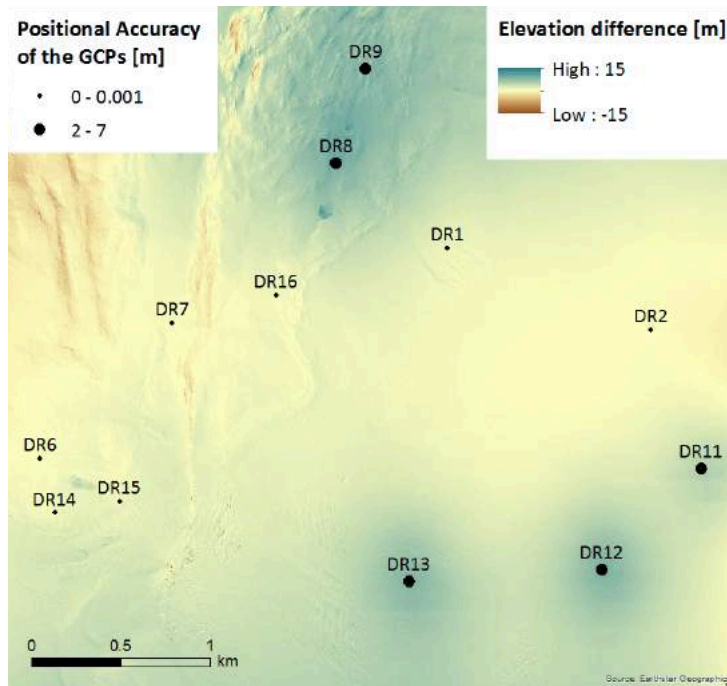
*Figure 24*: *Dh-grid of two versions of the 2018 drone DEM: The first one without camera optimization, the second one with camera optimization taking into account the marked GCPs.*

Generating the dense point cloud is a time-consuming process and for the 2016 DEM it took 2h 25min to generate the depth maps and an additional 1h 34min to generate the dense cloud. This was done with a quality setting of *'high'* and the filtering mode on *'aggressive'*. For the much higher resolution 2018 dataset it was therefore decided to run the dense point cloud generation in *'medium quality'* mode, which still took 1d 10h for the depth map generation and an additional 3h for the dense point cloud generation. The depth filtering was kept in the *'aggressive'* setting. As Gindraux et al. (2017) state, the effect of the different depth map qualities on the final DEM is very small and does in most cases not justify the much higher computational time required to run a *'high quality'* setting. The DEMs were then directly created from the dense cloud and the optional step of creating a mesh was ignored. From now on, the 2016 drone DEM will be referred to as DR16, while the 2018 drone DEM will be referred to as DR18.

*Table 5*: *Comparison of the final parameters of SFM products generated from the 2016 and 2018 drone footage.*

|  | DR16 | DR18 |
| --- | --- | --- |
| **Number of drone images used** | 406 | 1926 |
| **Amount of points in sparse cloud (tie points)** | 256'934 | 828'511 |
| **Amount of points in dense cloud** | ca. 222 million | ca. 860 million |
| **Ground resolution** | 15.3 cm/pix | 8.3 cm/pix |
| **DEM resolution** | 30.7 cm/pix | 16.5 cm/pix |
| **DEM point density** | 10.6 points/m$^2$ | 36.8 points/m$^2$ |
| **3D RMSE in respect to GCPs** | 6.40 m | 0.42 m |

35

## 5.3.    SFM on Historic Aerial Images

### 5.3.1.    1959 Aerial Images

The 1959 aerial images (see chapter 4.1) were provided by Anders Anker Bjørk of the SDFE and are scans from contact-copies scanned at 600dpi. The dataset covers an area of about 394km$^2$ including Nunap Kigdlinga, Sermeq Kujalleq and the Eqip Sermia terminus. It is made up of 9 images taken from a flying altitude of around 8300m.

The images were pre-processed in *Adobe Lightroom* (Version 5.7.1). The scans were rectified and cropped in order to remove the frames caused by the photographing and scanning process. Additionally, the images were harmonized in terms of brightness and contrast. Nonetheless, three images had areas of over- or underexposed pixels. Regions of bright ice are especially prone to this problem and one of the images did concern the area of Nunap Kigdlinga and Sermeq Kujalleq. Since this area was only covered by three images (see Figure 25), the points in the overexposed areas led to some artefacts in the data, which were later removed by high noise detection (see chapter 5.6.1).
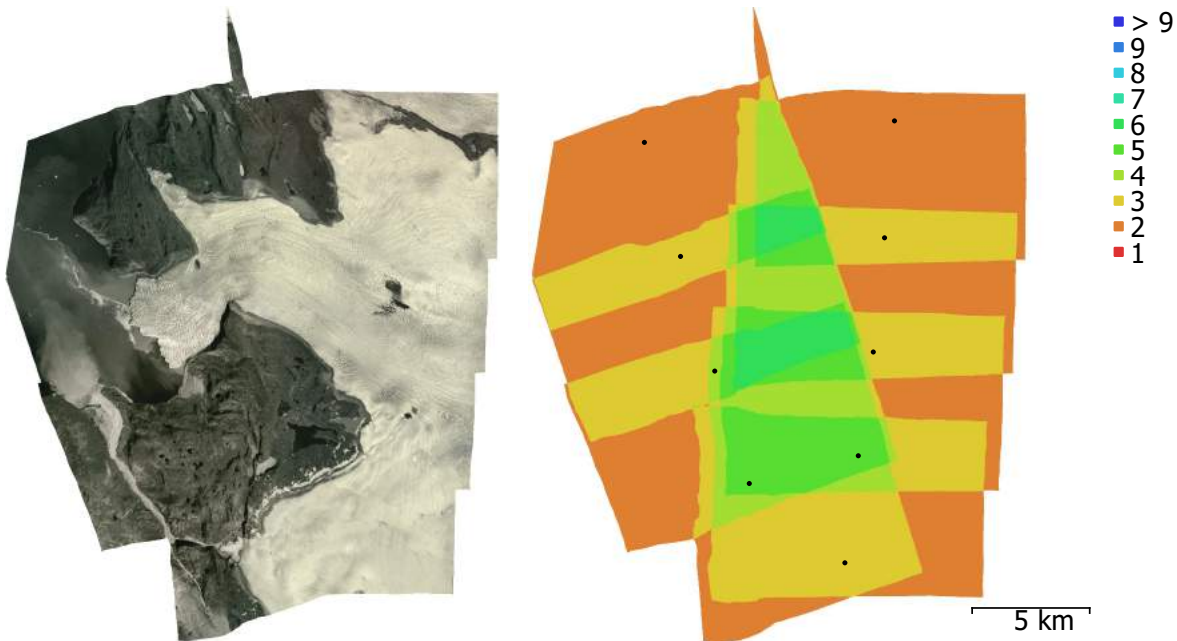


*Figure 25*: *Orthophoto (left) and camera locations and image overlap (right) of the SFM59.*

In *Agisoft Photoscan*, the central markers on each of the four image sides were masked in order to exclude these pixels from the aligning process that followed. Since there was no positional information available for the camera positions to use as input data, the alignment parameter was set on *'generic preselection'* only, while the accuracy was set to *'high'*. The amount of tie points amounted to around 14'000 (see also Table 6).

The positional information could only be introduced after the alignment process. This was done using GCPs from the 1985 orthophoto (see chapters 4.1 and 4.3.1), which was one of the highest resolution orthoimages available and was also temporally closer to the date of acquisition of the 1959 aerial images than other sources. However, that should not matter, because only points in stable terrain were taken into account for the georeferencing. In total, 19 points

were selected, which were visible both on the 1985 orthophoto as well as on the 1959 aerial images. If possible, the GCPs were selected to not be situated in steep areas, because the positional error tends to be higher in those areas.
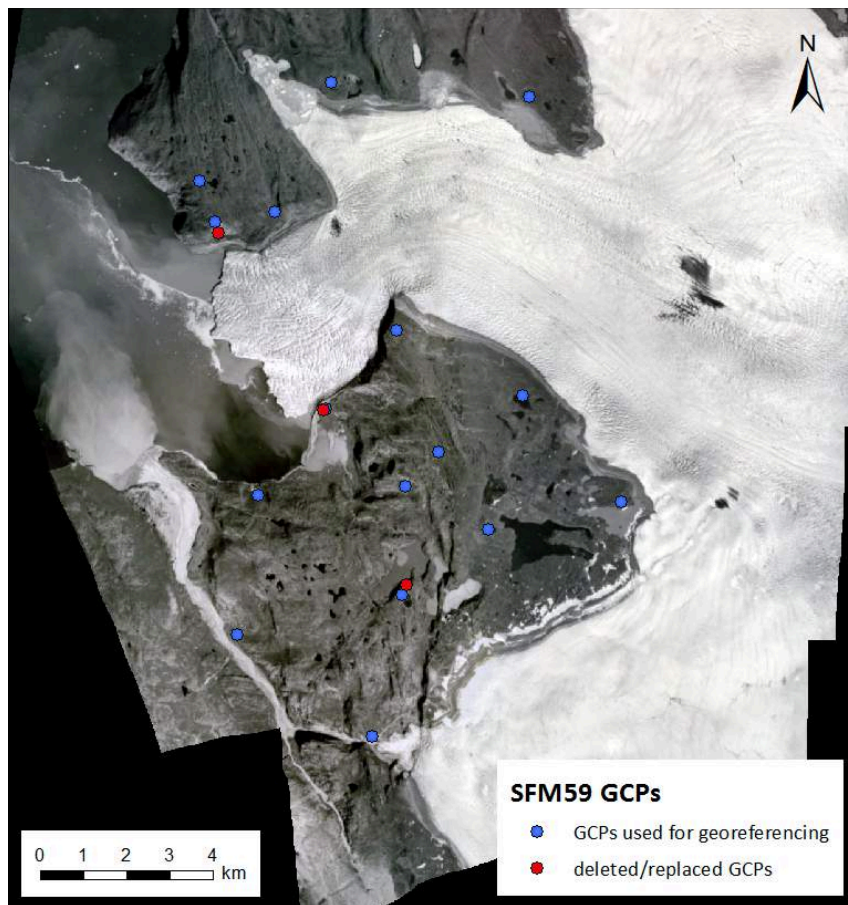


*Figure 26*: GCPs used to georeference the 1959 aerial images in Agisoft Photoscan.

In an iterative process, both the estimations of the camera locations were optimized according to the GCPs and the GCPs with the highest errors were eliminated or replaced (see Figure 26). In the end, 16 GCPs with a total error of 27.8m were used to georeference the model. The total x-, y- and z-errors amounted to 8.8m, 13.7m and 22.5m respectively. Now the dense point cloud could be generated, which was done in *'high quality'* mode with *'aggressive'* depth filtering. Just as for the drone datasets, the DEM was directly calculated from the dense point cloud, without going through the additional step of creating a mesh. This DEM is referred to as SFM59 from now on. In Table 6 the parameters of the final SFM products of this dataset are listed.

*Table 6*: *Parameters of the final SFM products generated from the 1959 aerial imagery*

|                                                 | SFM59               |
|-------------------------------------------------|---------------------|
| **Number of images used**                       | 9                   |
| **Amount of points in sparse cloud (tie points)** | 14'433            |
| **Amount of points in dense cloud**             | ca. 17.8 Mio        |
| **Ground resolution**                           | 2.25 m/pix          |
| **DEM resolution**                              | 4.51 m/pix          |
| **DEM point density**                           | 0.049 points/$m^2$  |
| **3D RMSE in respect to GCPs**                  | 27.8 m              |

### 5.3.2.    1985 Aerial Images

As discussed in chapter 4.3.1, the AeroDEM of 1985 has a series of limitations, especially on bare ice. In an effort to improve the data quality, the original imagery provided by A. Bjørk (SDFE) was imported to *Agisoft Photoscan*. However, it soon became clear that an improvement of data quality was not possible without going through extensive additional effort. It was therefore decided to use the AeroDEM itself, rather than a re-generated SFM-model.

## 5.4. Topo to Raster

The first existing laminar data of Nunap Kigdlinga and Sermeq Kujalleq consists of two topographic maps generated from leveling data and terrestrial photogrammetric mapping (de Quervain & Mercanton 1920). In order to compare this data to modern elevation data, the maps had to be converted to DEMs. In order to get a continuous raster dataset, an interpolation is necessary. *ArcMap* offers several tools to do this, such as Inverse Distance Weighting (IDW), Spline, Kriging or Natural Neighbor interpolation (Childs 2004). However, for topographic data the *Topo to Raster* method is the most fitting, since it was specifically designed to work with contour lines, incorporating the approach by Hutchinson (1989). However, it can take different input data formats into account, such as line features (contour lines and streams), points (e.g. summits) as well as areas (e.g. lakes) and creates a hydrologically correct DEM incorporating all this information, while preserving the input data (Childs 2004; Hutchinson 1989; Pellitero et al. 2016).

In this study, the workflow consisted of the following steps (see Figure 27):

1. Georeferencing the scanned maps of de Quervain & Mercanton (1920). This was done with clearly identifiable reference points, which were re-measured in the 2018 field campaign using a differential GPS (Leica SR-530).
2. Manual digitization of all relevant map features (contour lines, streams, benchmarks, water bodies). The water's edge of ponds and lakes is considered as a line of equal elevation treated like the contour line dataset.
3. Running the Topo to Raster tool with a maximum of 20 iterations as suggested by Hutchinson et al. (2011), generating a preliminary DEM (2m raster). The drainage enforcement was turned off in this step, in order to keep terrain sinks in the dataset, since hydrological correctness is not necessarily true on ice surfaces (cf. Pellitero et al. 2016).
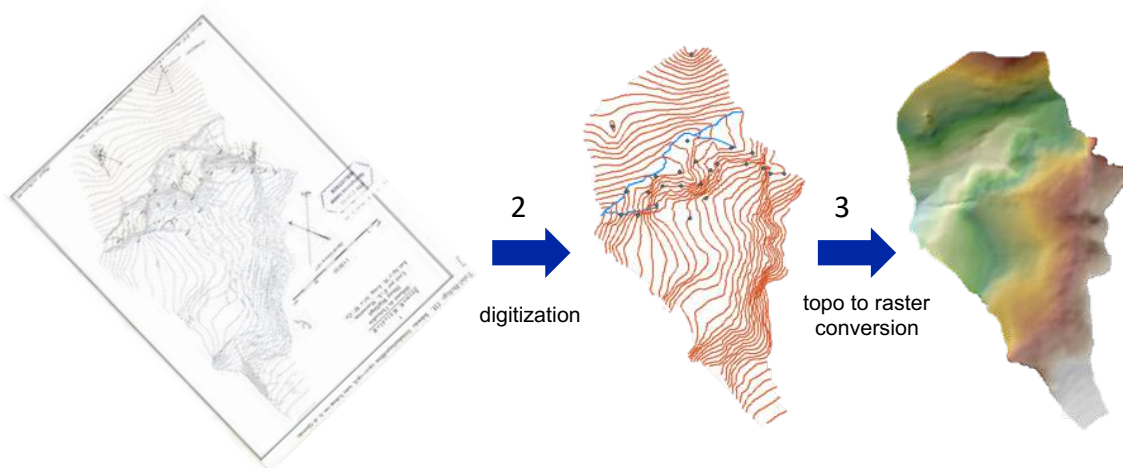


*Figure 27*: *Steps 2 and 3 of the* Topo to Raster *workflow using the example of the Sermeq Kujalleq map of 1912* (de Quervain & Mercanton 1920)*. For a large version of the original map, see Figure 73 in Appendix A.*

## 5.5. Co-Registration

In order to rule out any systematic errors in the comparison of different DEMs, it is necessary to determine systematic shifts in x-, y- and z-direction. To do so, a so-called 'master DEM' is defined, which is considered as the main reference to which all other 'slave DEMs' are fitted. When determining these horizontal and vertical biases, changes in the landscape over time should not play a role. Thus, only areas considered as long-term stable terrain are taken into account (see chapter 5.5.3).

For this thesis, the co-registration methodology by Nuth & Kääb (2011) was applied. This approach has become somewhat of a standard and has been successfully used in several instances, such as by Dai et al. (2018), Denzinger (2018), Korsgaard et al. (2016) or Mölg & Bolch (2017). It focuses on analyzing three potential biases:

1. The geo-location of the data (x, y and z)
2. An elevation-dependent bias
3. Biases related to the acquisition geometry of the data

An elevation-dependent bias was detected for one dataset (see chapter 6.2.1), but not systematically checked for within this thesis. The biases related to the acquisition geometry of the data were not considered, because it would go beyond the scope of this thesis.

Thus, the geo-location bias is the only systematic bias analyzed and corrected in this thesis. It can be determined by solving Equation 4.

$$\frac{dh}{\tan(\alpha)} = a \cdot \cos(b - \psi) + c \qquad \textbf{\textit{Equation 4}}$$

where

$$c = \frac{\overline{dh}}{\tan(\bar{\alpha})}$$

Here, *dh* stands for the calculated elevation difference values for the stable terrain areas between the master DEM and the slave DEM. $\alpha$ describes the slope, $\psi$ the aspect. The variables *a* and *b* describe the magnitude and the direction of the horizontal shift vector to be applied to the slave DEM respectively. *c* is the mean vertical bias between the two DEMs over stable terrain (Korsgaard et al. 2016; Nuth & Kääb 2011).
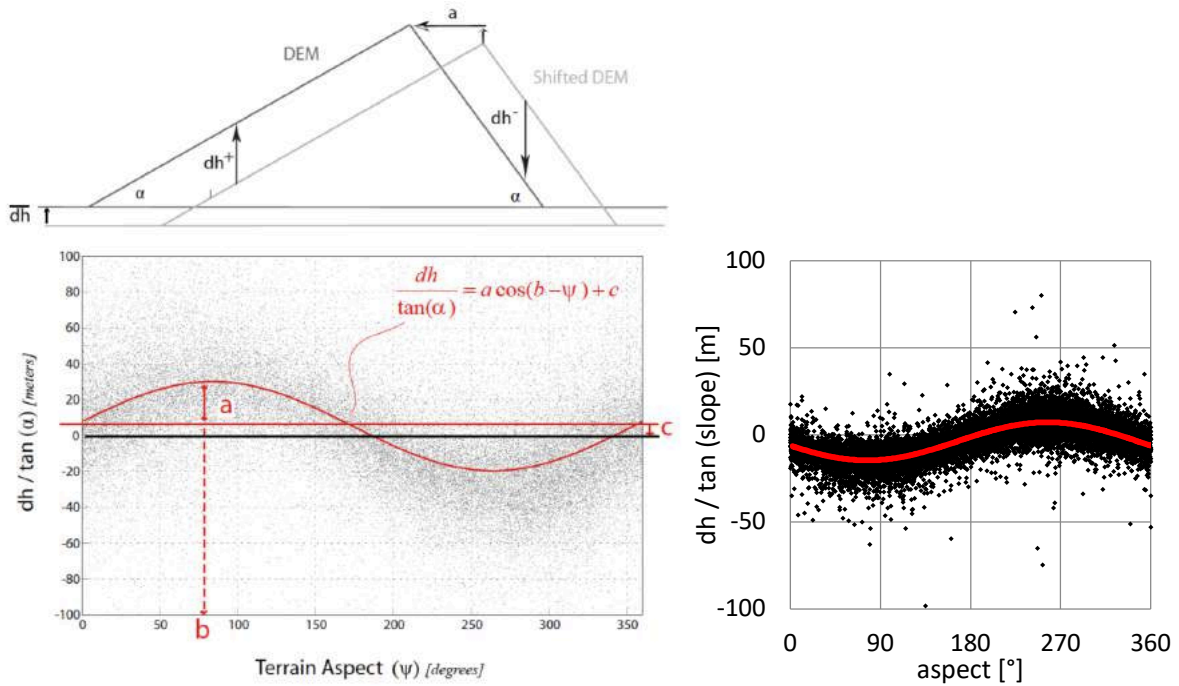
**Figure 28**: Co-registration shifts and their influence on the relationship of $\frac{dh}{tan(\alpha)}$ (left, figure by Nuth & Kääb 2011: 36). Example of the first co-registration iteration for AD17 (right).

If there is in fact an offset, the relationship between slope and aspect results in a sinusoidal curve (see Figure 28). The unknown parameters *a*, *b* and *c* are then approximated by solving the equation with a least-squares minimization. As a next step, the actual offset in x-, y- and z-direction can be calculated using the following equations (Kääb 2005; Nuth & Kääb 2011):

$$\Delta x = a \cdot \sin(b) \qquad \qquad \textit{Equation 5}$$

$$\Delta y = a \cdot \cos(b) \qquad \qquad \textit{Equation 6}$$

$$\Delta z = \frac{c}{\tan(\bar{a})} \qquad \qquad \textit{Equation 7}$$

These offsets are then applied to the initial slave DEM, before calculating a new dh-grid between the master DEM and the fitted slave DEM. These steps are repeated iteratively up to three times (see chapter 5.5.4).

### 5.5.1. Preparation of the DEMs

Before starting the co-registration process, all available DEMs have to be harmonized in terms of the geographical reference system as well as spatial resolution. All the DEMs used in this thesis are listed Table 7 (note that from now on, all DEMs will only be referred to by the code listed in the first column). For the geographical reference system, it was decided to use the *WGS84 / NSIDC Sea Ice Polar Stereographic North* reference system (EPSG:3413). This is also the dataset in which the ArcticDEM and the GimpDEM are delivered. The ASTER DEMs as well as the AeroDEM were transformed from UTM22N in *ArcMap*. All other sources (DQ12, SFM59, DR16 and DR18) were georeferenced directly in the selected geographic reference system during the process of their generation.

The original spatial resolution of the datasets varies considerably, as is visible in Table 7. For simplicity and comparability reasons, it was decided to create two groups – one with a resolution of 2m, one with a resolution of 10m. All datasets except the ArcticDEMs, which were already in the correct resolution, were therefore resampled to match the resolution of their respective group. For most of the lower resolution DEMs that led to an upscaling from 25 or 30m resolution to 10m resolution, which proved to be an efficient way to minimize 'tiling' effects associated with the reprojection of datasets with similar, but not equal pixel size (e.g. 25m and 30m). All resampling to a higher resolution was done using the *'bilinear interpolation'* approach, all resampling to a lower resolution was done using the *'nearest neighbor'* procedure. It is important to note that this has an influence on the pixel density, but the spatial resolution of the data is still that of the original resolution.

*Table 7*: *Overview of the comparable DTMs used in this thesis, ordered by acquisition date. GD0309 and ADcomp (\*) are composites and the exact acquisition dates are unknown.*

| Code | Source | Elevation Acquisition Date | Original Resolution [m] | Resampled Resolution [m] |
|---|---|---|---|---|
| **DQ12** | Topographic map (de Quervain & Mercanton 1920) | 13.08.1912 | N/A | 2 |
| **SFM59** | Aerial Images, SFM | 25.06.1959 | 4.5 | 10 |
| **AE85** | AeroDEM (Korsgaard et al. 2016) | 09.07.1985 | 25 | 10 |
| **AS03** | ASTER snapshot | 09.06.2003 | 30 | 10 |
| **GD0309** | GimpDEM (Howat et al. 2014) | 2003-2009* | 30 | 10 |
| **AS10** | ASTER snapshot | 09.07.2010 | 30 | 10 |
| **AD13** | ArcticDEM | 11.08.2013 | 2 | 2 |
| **AD14** | ArcticDEM | 04.07.2014 | 2 | 2 |
| **AD15** | ArcticDEM | 24.10.2015 | 2 | 2 |
| **AD16** | ArcticDEM | 11.03.2016 | 2 | 2 |
| **AS16** | ASTER snapshot | 07.07.2016 | 30 | 10 |
| **DR16** | Drone images, SFM | 24.08.2016 | 0.3 | 2 |
| **AD17** | ArcticDEM | 21.08.2017 | 2 | 2 |
| **ADcomp** | ArcticDEM | 2011-2017* | 2 | 2 |
| **DR18** | Drone images, SFM | 08.07.2018 | 0.2 | 2 |

For the three ASTER datasets, a further pre-processing step was necessary. Some areas of these DEMs contain heavy artefacts caused by clouds, which generate areas of large noise (see chapter 4.3.3). Thankfully, these areas are often rather obvious to see and can therefore be manually masked. The false-color image of the same scene was also considered. For some of the datasets, this step reduced the area of stable terrain available for comparison.
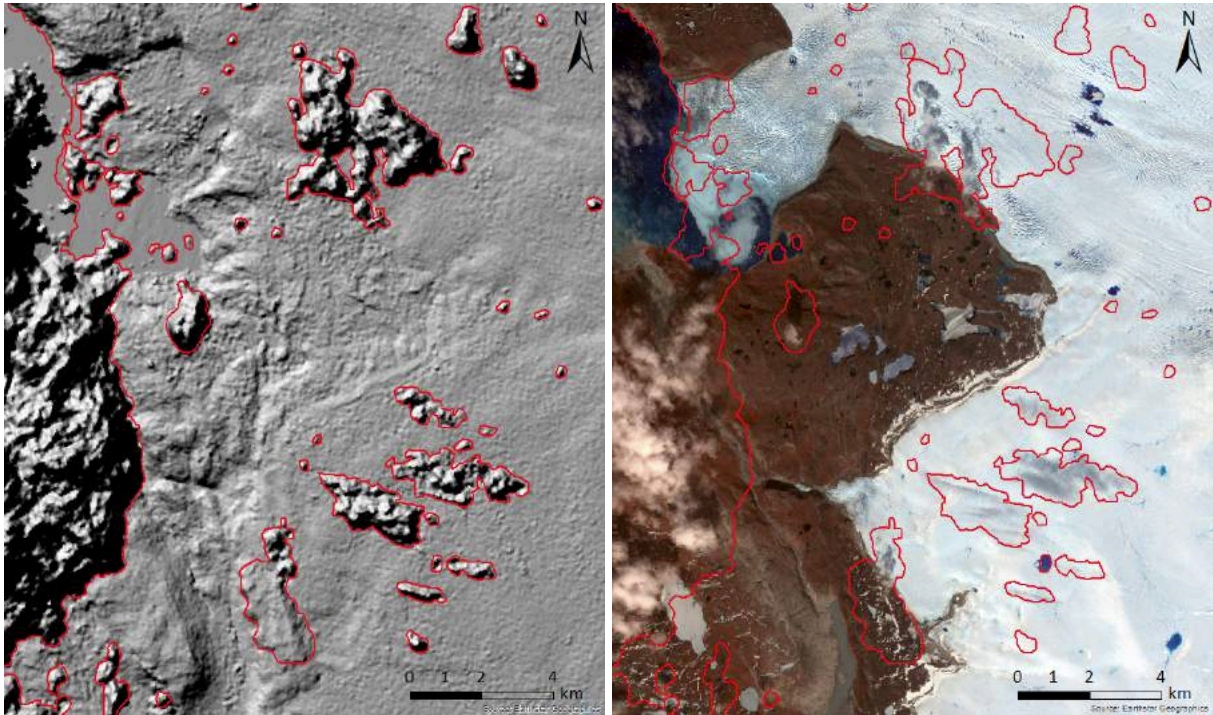


*Figure 29*: Manual selection of cloud artefacts in the AS03 DEM (left) and false-color orthophoto (right). Outlined in red are the masked areas. With data from U.S/Japan ASTER Science Team (2007).

### 5.5.2. Selection of Master DEM

When comparing several DEMs with each other like in this thesis, it is important to keep the same master DEM throughout the whole process, even if comparing two different slave DEMs. The selected DEM therefore serves as the main reference for all other DEMs and should be high quality, high resolution and with complete coverage of the area of interest.

For this paper, two datasets fulfilled these criteria: The ArcticDEM snapshot dataset of 21st of August 2017 and the composite ArcticDEM (v.3.0). In order to evaluate the two possible datasets, the differential GPS measurements taken in the field were taken as a reference. In total 16 measurements with accuracies of less than 0.001m were considered. The measured elevation was compared to both the elevation data of ADcomp and AD17 (see Table 8).

*Table 8*: *Comparing the differential GPS measurements from 16 GCPs with the respective values of the ArcticDEM composite (v.3.0) and the 2017 ArcticDEM snapshot.*

| Differences in comparison to differential GPS measurements | ADcomp | AD17 |
|---|---|---|
| **Median [m]** | 0.52 | -1.28 |
| **Mean [m]** | -0.10 | -0.98 |
| **Standard deviation [m]** | 2.24 | 1.19 |

Even though the standard deviation of the 2017 ArcticDEM snapshot differences is slightly smaller than those of the composite, both the median and the mean differences of all GCPs are smaller than the 2017 ArcticDEM snapshot. This is an indication of a higher accuracy for the composite. Additionally, it is a patchwork of the best quality snapshots throughout the last decade and has been registered to ICESat altimetry information prior to release and has therefore been cross-checked (NGA & NSF 2018). Considering all this information, the ArcticDEM composite v.3.0 was selected as the master DEM for all co-registration procedures.

### 5.5.3. Determination of Stable Terrain

This thesis covers a timespan of more than a century and hence the stable terrain should be an area of solid ground only. Several masks were applied to the area in order to remove all areas of potential movement. First, a GEUS shapefile with surface classifications provided by Dr. P. Rastner was used to remove all water bodies and ice surfaces as well as fluvial plains of rivers, which obviously undergo massive changes over time and therefore do not qualify as stable surfaces. The goal was then to also exclude all moraines because they consist of loose material which is more prone to movement than bare rock or also vegetation covered areas. A preliminary map of the different moraine complexes in the study area was provided by Prof. Dr. A. Vieli and adapted for this purpose. Following the recommendations of PD Dr. T. Bolch, the area of stable terrain was further constrained by eliminating areas with slopes >30° because these steep areas are known to bear higher uncertainties, especially concerning elevation values. All slopes of <10° were also eliminated, because aspect uncertainties in flat areas are known to be high. This also had the additional benefit that all water bodies not previously removed were securely eliminated.
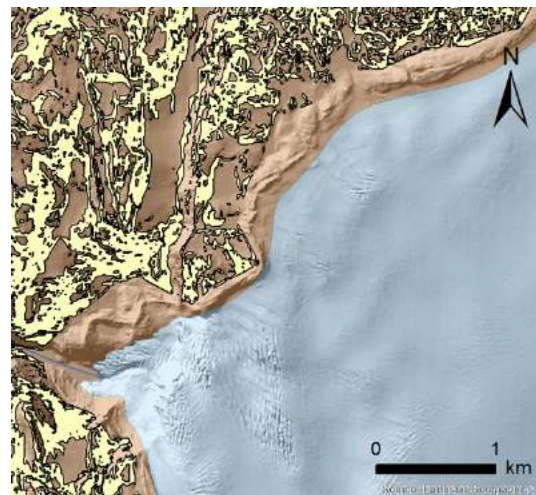


*Figure 30*: *The stable terrain (marked in yellow) used for the co-registration as well as for the uncertainty calculations. The hill shade in the background is from the ADcomp dataset.*

### 5.5.4. Co-Registration Workflow

Due to the different capabilities of the used applications *ArcMap* and *Excel*, the typical work-flow consisted of three isolated steps. Each step was automated as much as possible in the respective program using *ArcGIS Modelbuilder* and an Excel-file developed by Chris Nuth.

- Step 1 (*ArcMap*): Calculation of the dh-grid, slope and aspect. For each slave DTM dataset, these values on stable terrain were then translated to a point dataset and reduced to a more reasonable number of around 15'000 points.
- Step 2 (*Excel*): Here, the *'Solver…'* function was used to perform the curve fitting and calculate $\Delta x$, $\Delta y$, and $\Delta z$.
- Step 3 (*ArcMap*): The offsets of the initial slave DEM are corrected by applying the corrections calculated in Step 2.
- These three steps were then repeated iteratively as long as both the mean and the standard deviation of the dh-grid over stable terrain improved/became smaller. As soon as one of the two did not show any further improvements, the iteration process was stopped.

The improvements in the mean and standard deviation of the dh-grid over stable terrain, as well as final corrections applied to each of the datasets can be found in Table 13 and Table 14 in chapter 6.2.

### 5.5.5. Co-Registration of DQ12

Due to the fact that only a very small subset of the areas mapped in 1912 can be considered as stable terrain, co-registration in the traditional sense of the way was not possible. Additionally, the left side of the river on the Sermeq Kujalleq map (the only more or less stable terrain on the map) was *"not perfectly"* mapped, because of the loss of a photograph according to de Quervain & Mercanton (1920: 233). But since the reference points on the maps had been georeferenced to differential GPS measurements, no x- or y-offset was present. The vertical (z) offset was corrected using the only two clearly identifiable reference points in each of the two 1912 maps. For Nunap Kigdlinga these two points were 17.7 and 19.2 m off, resulting in a mean offset of -18.5m. A z-offset of -11.1m was detected for the map of Sermeq Kujalleq (-12.6 and -9.5m for the two points respectively). These mean offset values were then corrected for the whole map extent.

## 5.6. Post-Processing

### 5.6.1. Removal of High Noise Areas

After completion of the co-registration process, the DEMs can be further improved and cleaned by removing areas of high noise. The selected approach involves both a dataset with little noise (in this thesis ADcomp), as well as the dataset to be filtered (namely the four datasets AS03, AS10, AS16 and SFM59 with high noise areas). Figure 31 illustrates the workflow for the example of SFM59.

In Step 1, focal statistics are run for both datasets and the data ranges for 9x9 pixel windows are calculated (ADcomp on the top, SFM59 on the bottom). These are then subtracted from each other in step 2, thereby filtering out the rough terrain and leaving only the actual noise. In step 3 a threshold is applied to the range difference. In this case a threshold of -9m was chosen (for the three ASTER DEMs, a threshold of -12m was chosen). All pixels below this threshold are masked and disregarded for all further use. It was also considered to integrate a second, positive threshold. However, since positive values indicate areas where the range of the ADcomp is higher than the range of the SFM59, this could be an effect of the higher initial resolution of ADcomp and thus it was decided not to implement an additional positive threshold.

Also, note that the lower area of the Sermeq Kujalleq glacier tongue was exempt from the masking (see Figure 31, step 3). This is due to the fact that this area has a complex topography and rapid changes are not uncommon. It is therefore an area of 'naturally occurring' noise.
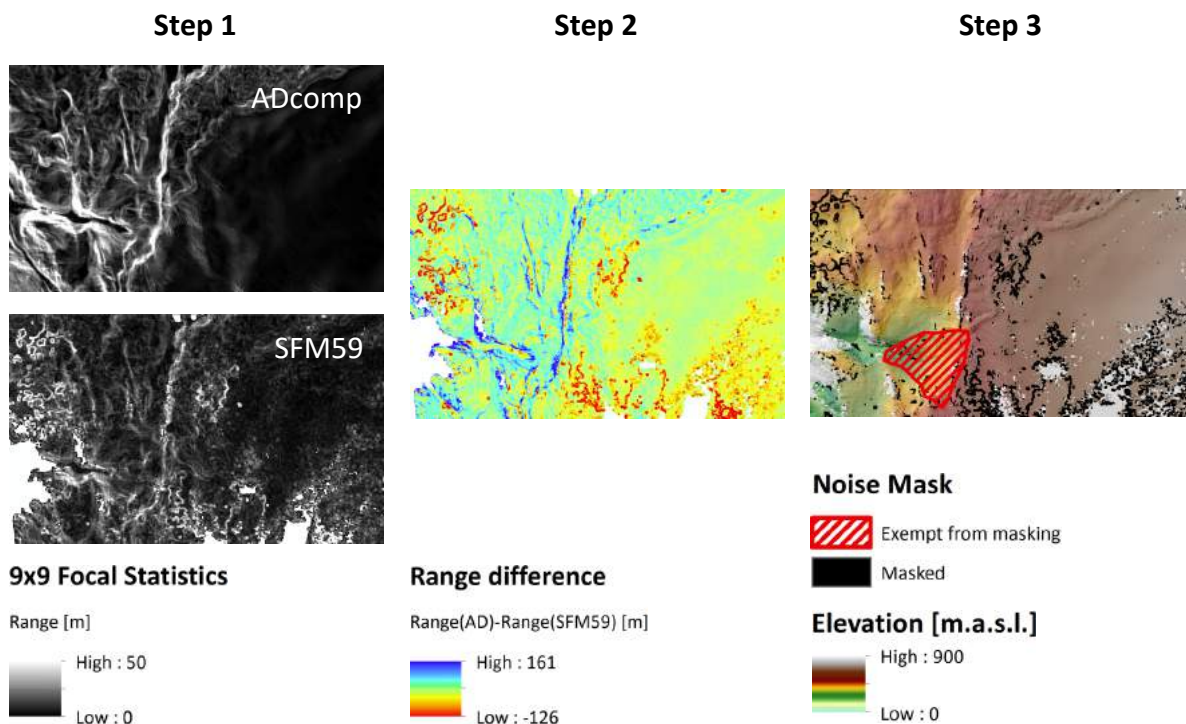


*Figure 31*: *Workflow for the removal of high noise areas for the example of SFM59. In step 1 the 9x9 range of the ArcticDEM composite is shown on the top, the one of SFM59 on the bottom.*

### 5.6.2. Removal of Interpolated Data

Most of the used datasets do not include interpolated data. In the creation of the SFM DEMs (DR18, DR16 and SFM59), the interpolation option was avoided. The only dataset including large amounts of interpolated data was the AeroDEM of 1985 (see chapter 4.3.1). However, Korsgaard et al. (2016) provide a reliability mask along with their dataset. A mask was generated according to their suggestions and only pixels with a Figure of Merit (FOM) ≥40 were considered in all further applications.

## 5.7. DTM Quality and Uncertainty Assessment

In order to assess the uncertainty of all DTMs, they are compared to the reference dataset ADcomp, which is also used as the master DTM in the Co-Registration process (see chapter 5.5.2). Here too, only areas of stable terrain are considered. All uncertainty values presented in this study are therefore relative to the stable terrain in the ADcomp dataset. The only exception are the RMSE values of the DTMs generated with SFM, which are with respect to the GCPs used as input data (see Table 5 and Table 6).

The most important relative descriptors of uncertainty, which are also used to evaluate the co-registration process, are the pixel standard deviation ($\hat{\sigma}$) and the mean error ($\hat{\mu}$). They are calculated according to Equation 8 and Equation 9. Their values are listed for each of the datasets before and after co-registration in Table 13 and Table 14 and present a rough first estimate of the general DTM quality after the Co-Registration (Mölg & Bolch 2017). The standard deviation is also used to define the error bars in all related figures.

$$\hat{\mu} = \frac{1}{n} \sum_{i=1}^{n} \Delta h_i$$

*Equation 8*

$$\hat{\sigma} = \sqrt{\frac{1}{(n-1)} \sum_{i=1}^{n} (\Delta h_i - \hat{\mu})^2}$$

*Equation 9*

However, the datasets used in this thesis are very diverse in terms of source data, resolution as well as uncertainties in the production of the DTM. In order to describe the DTM quality in more detail, further analysis is needed. Höhle & Höhle (2009) propose using a histogram, which displays the frequency and distribution of the sampled errors. However, for DEMs derived from SFM or photogrammetry, a normal (Gaussian) distribution of errors is usually not the case. This becomes obvious, if they are compared to the expected normal distribution of the same dataset (see Figure 32). This expected Gaussian distribution is calculated using the non-robust estimators standard deviation ($\hat{\sigma}$) and median. Höhle & Höhle (2009) prefer this visual approach to check for normality over statistical tests, which are often sensitive to outliers.
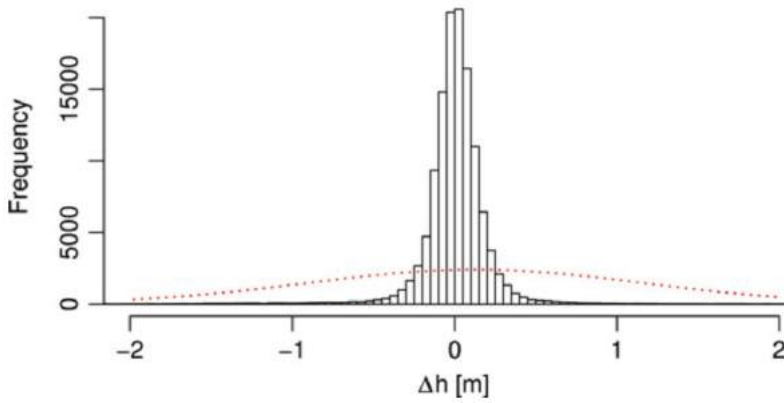
**Figure 32**: *Histogram of the errors Δh in meters. Superimposed on the histogram are the expected counts from a normal distribution with mean and variance estimated from the DEM data using non-robust estimators. For a better visualization the histogram is truncated at -2m and 2m. The mismatch between data and estimated normal curve is due to heavy tails. Figure from Höhle & Höhle* (2009: 399). *Note that the frequency is measured in number of pixels, while in this thesis it will be measured in percent of the total number of pixels, in order to make different resolutions comparable.*

These outliers, also referred to as *'heavy tails'* in the histograms, are common in DEMs derived from SFM or photogrammetry. Höhle & Höhle (2009) thus propose four additional, robust accuracy measures, which are suitable for non-normal error distributions (see Table 9).

**Table 9**: *Accuracy measures for DEMs as proposed by Höhle & Höhle* (2009: 401).

| Accuracy measure | Error type | Notational expression |
|---|---|---|
| **Median (50% quantile)** | $\Delta h$ | $\hat{Q}_{\Delta h}(0.5) = m_{\Delta h}$ |
| **Normalized median absolute deviation (NMAD)** | $\Delta h$ | $NMAD = 1.4826 \cdot median_j\left(\left|\Delta h_j - m_{\Delta h}\right|\right)$ |
| **68.3% quantile** | $\left|\Delta h\right|$ | $\hat{Q}_{\left|\Delta h\right|}(0.683)$ |
| **95% quantile** | $\left|\Delta h\right|$ | $\hat{Q}_{\left|\Delta h\right|}(0.95)$ |

The Normalized Median Absolute Deviation (NMAD) is introduced as a robust scale estimator, while the quantiles can be understood as follows: As an example, 95% of the errors displayed in the histogram will be between 0 and $\hat{Q}_{\left|\Delta h\right|}(0.95)$, which is the value of the 95% quantile. The 68.3% quantile was selected, because with a normal distribution, 68.3% of the error will fall within the interval $\mu \pm \sigma$ (Höhle & Höhle 2009).

## 5.8.    DEM Differencing

To determine the surface elevation changes over time, the co-registered DEMs listed in Table 7 were subtracted from the most current DEM, the DR18, according to Equation 10.

$$dh_{DEM1-DEM2} = DEM_1 - DEM_2$$    *Equation 10*

Where $dh_{DEM1\text{-}DEM2}$ is equal to the difference in elevation between the earlier and the later DEM. $DEM_1$ describes the later DEM (DR18), while $DEM_2$ describes the earlier DEM. There was also the idea to calculate the dh-grids between the successive datasets. However, this idea was abandoned due to the fact that uncertainties for the two compared datasets add up. So, if two datasets with high uncertainties are compared to each other, the uncertainty becomes so high, that a meaningful analysis of the changes is not possible. That is why DR18 was selected as the only reference dataset. DR18 has comparably low uncertainties, thus allowing a proper analysis.

For each calculation it was ensured, that both DEMs had the same spatial resolution. If necessary, the higher resolution DEM was therefore resampled using the *'nearest neighbor'* procedure, which is the go-to procedure when resampling to a lower resolution.

Unlike in most papers where the technique of DEM differencing is applied to one or more clearly definable glaciers (e.g. Denzinger 2018; Frey & Paul 2012; Mölg & Bolch 2017; Nuth & Kääb 2011), the AOI in this paper does not cover the entire glacial system and the borders of the AOI are somewhat arbitrary. This is the reason why further analysis like calculating the volume change or the mass balance do not make any sense in this example. Instead, the focus lies on analyzing the temporal surface elevation development of profiles (chapters 6.4.2 and 6.4.3) or even just single points (chapter 6.4.4).

## 5.9.    Ice Margin Mapping

In order to generate retreat lines for Sermeq Kujalleq, satellite and aerial images were used to delineate the ice border at different points in time. Table 10 provides an overview of the used datasets, their exact acquisition dates as well as the estimated mapping uncertainty, which mostly depended on the spatial resolution as well as the type of dataset. Generally, orthophotos were easier to map than DEMs and higher resolution images have less uncertainty than low resolution data.

*Table 10*: *The dates, sources and mapping uncertainties of the datasets used to create the retreat lines of Sermeq Kujalleq (see Figure 40). Note that the mapping uncertainty only depicts the uncertainty associated with the mapping process. Any uncertainties with the source data-set are not represented in this number.*

| Year | Exact Date | Source | Mapping Uncertainty [m] |
|------|-----------|--------|------------------------|
| **1912** | 13.08.1912 | de Quervain & Mercanton (1920) | ±5 |
| **1959** | 25.06.1959 | EGIG SFM orthophoto | ±15 |
| **1964** | 12.07.1964 | Aerial image EGIG | ±15 |
| **1985** | 09.07.1985 | AeroDEM orthophoto | ±15 |
| **2003** | 09.06.2003 | ASTER satellite image | ±30 |
| **2006** | 19.07.2006 | ASTER satellite image | ±30 |
| **2009** | 11.07.2009 | ASTER satellite image | ±30 |
| **2010** | 09.07.2010 | ASTER satellite image | ±30 |
| **2011** | 11.07.2011 | ASTER satellite image | ±30 |
| **2012** | 10.07.2012 | ASTER satellite image | ±30 |
| **2013** | 22.07.2013 | ASTER satellite image | ±30 |
| **2014** | 18.07.2014 | ASTER satellite image | ±30 |
| **2015** | 24.10.2015 | Arctic DEM | ±15 |
| **2016** | 24.08.2016 | Drone campaign 2016 | ±5 |
| **2017** | 21.08.2017 | ArcticDEM | ±15 |
| **2018** | 08.07.2018 | Drone campaign 2018 | ±5 |

## 5.10.   Determination of Ice Flow Velocities

When talking about ice flow velocities, it is important to realize that ice flow is not consistent for all ice depths and is usually the fastest at the surface. It mostly depends on the ice thickness and surface slope, but bed topography, melt water as well as the temperature of the ice also play a role (Benn & Evans 2010). The measurements in this thesis are constrained to the surface ice flow velocities.

### 5.10.1. Feature Tracking 2013-2018

In order to gain information on current surface ice flow velocities, the two high-resolution orthophotos and DEMs generated from the drone footage of 2016 and 2018 were utilized. They have a high degree of detail, which allows for the identification of different features on the ice, such as cracks, crevasses, supraglacial meltwater channels, areas of discoloration etc. Feature tracking on the GrIS is certainly connected to some uncertainties, since the GrIS lacks any permanent features transported on the ice such as large boulders. Hence many of these features are highly variable, but features like certain moulins, supraglacial river and creek bends as well as large cracks in part keep their form over the period of the two years and remain clearly distinguishable. From now on, they are referred to as 'stable features' in this thesis (not to be mistaken with 'stable terrain', cf. chapter 5.5.3). Figure 33 illustrates the problem nicely: The two images show the same area of Sermeq Kujalleq in 2016 (top) and 2018 (bottom). While the large crevasses in the western part of the picture occur on the same spot, they do not keep their form over the years and therefore no stable features can be traced over time. It is different for the meltwater channels in the center and east of the images though. While some channels change their form quite drastically, certain bends and curves stay relatively stable and can be recognized in both images. The fact that not all features behave in the same way is the main reason, why no automated feature tracking software was used, and a manual selection of stable features was necessary.
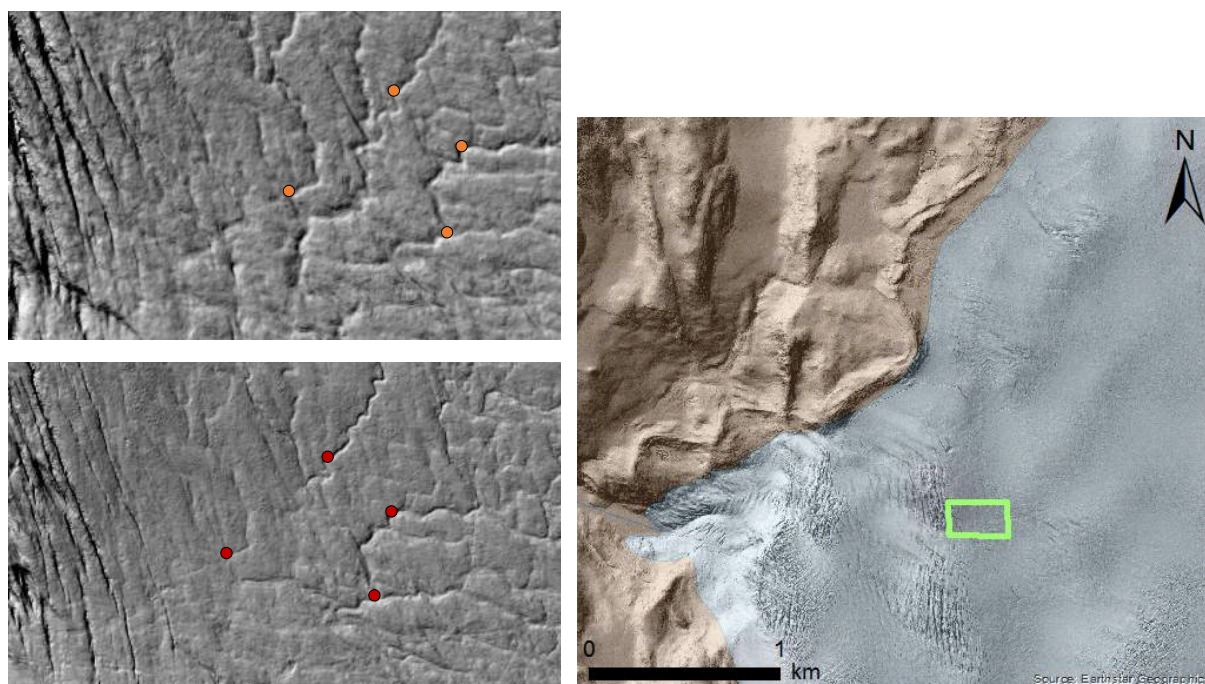


*Figure 33*: Example of four stable features on DR16 (top left, orange) and DR18 (bottom left, red) used for the velocity calculation between 2016 and 2018. The position of the example is marked on the right. See Figure 35 for a map of all used points.

Stable features were searched for and marked in the whole area of interest. The ArcticDEM scenes from 2013 to 2015 with a resolution of 2m enabled a traceback even further back in time. However, due to the lower resolution, fewer stable features were found for this period. In one case a feature was even traceable for the whole duration between 2013 and 2018.

### 5.10.2. Uncertainty and Control Measurements

Since all of these features could also change over time, this has to be considered as an uncertainty. Especially because any change in form (e.g. downstream propagation of supraglacial river curves) would likely be only downwards. If this is the case, a systematic error in these flow velocity estimations cannot be ruled out. To see if the data is reasonable, there were also measurements of three clearly identifiable artificial items on the ice, most likely remains of tents and other equipment from the EGIG / EPF missions. This concerns two bundles of tarp (see Figure 34) as well as a piece of wood close



*Figure 34*: *Differential GPS measuring of old EGIG tarps as in-situ control measurements of DEM-derived velocity detection. Note that they are partly frozen to the ice and are therefore not easily moved by wind.*

to today's ice border. All these items were measured in-situ with a handheld GPS with an uncertainty of around 5m in 2016 and a differential GPS with an uncertainty of about 1cm in 2018. In Figure 35, these three control points are marked with triangles.
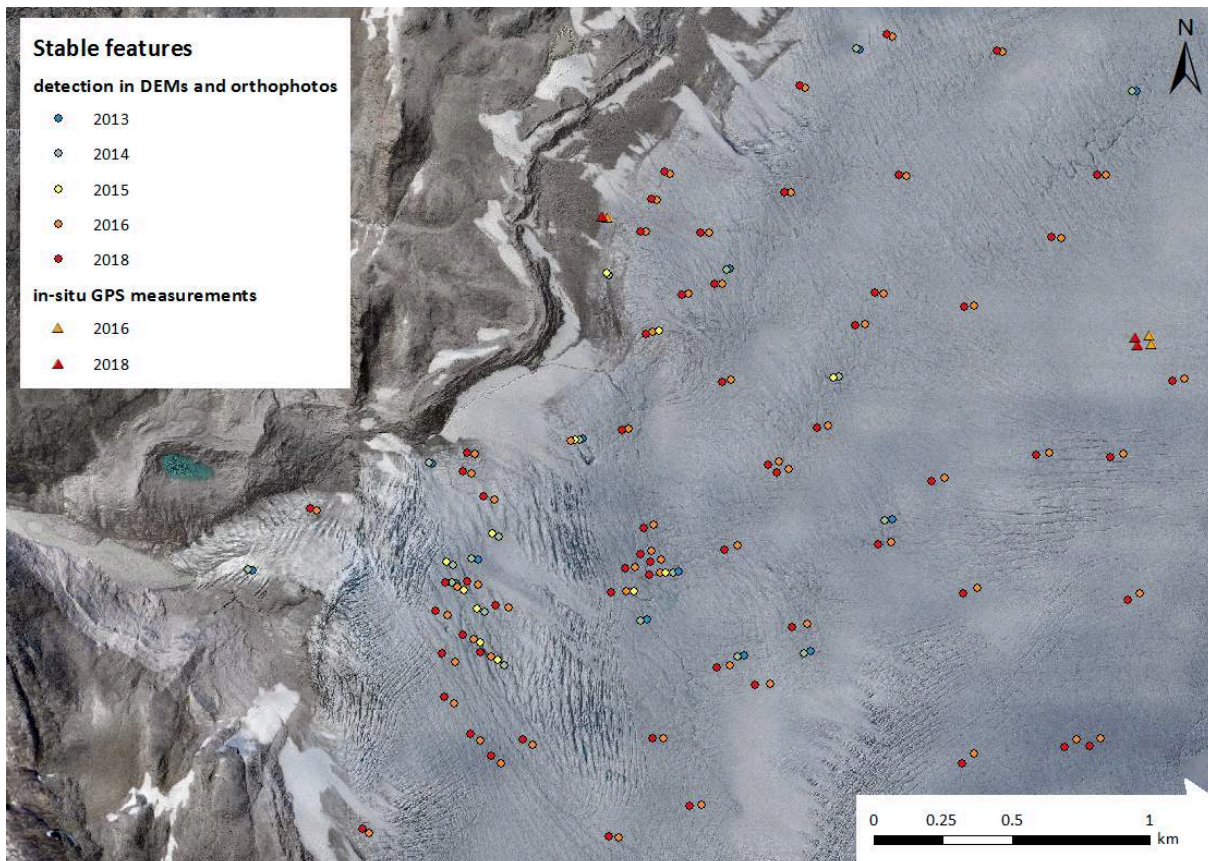


*Figure 35*: *Overview of the stable features used to derive flow velocities for the period of 2013 to 2018. The background image consists of the orthophoto and a hill shade of the 2018 drone DEM.*

## 5.11. Temperature Forcing

In order to check whether the measured surface elevation changes are connected to developments in temperature, it is important to try to reconstruct the measured surface elevation changes with the help of temperature data. To do so, one of the melt models described in chapter 3.4 will be adapted to simulate surface elevation change rather than melt/ablation. When selecting which model to use, it is important to look at the required data inputs: Both the EBM as well as the ETIM require shortwave radiation information as input data. This information is measured at the Swiss Camp weather station, but there are no long-term records available. In fact, air temperature data is the only option for long-term data of a century or more (see chapter 4.6). In consequence, a TIM, or to be more specific, a Positive Degree Month Model was selected, thus taking the average monthly temperatures as an index for the surface elevation change. Due to the fact that very long durations are of interest, this model should still provide sufficient results, whereas the EBM and ETIM model were generally developed for analyses with higher temporal resolution. If the reconstructed surface elevation from the temperature dataset agrees with the measured surface elevation change, it can be assumed that there is a connection between the temperature changes and the surface elevation changes.

### 5.11.1. Basic Assumptions

Due to the limited available data, four simplifying assumptions were made (see also Figure 36). The importance of the ignored parameters in the area are discussed in chapter 7.1.5.

1. The ablation is solely dependent of the temperature $>T_t$ (threshold temperature). All dynamic influences are neglected.
2. The air temperature behaves the same for the whole AOI
3. The measured surface elevation changes are only a combination of ablation and ice recharge from the ice sheet accumulation zone. Precipitation is ignored.
4. The ice recharge rate from the accumulation zone remains constant over time.
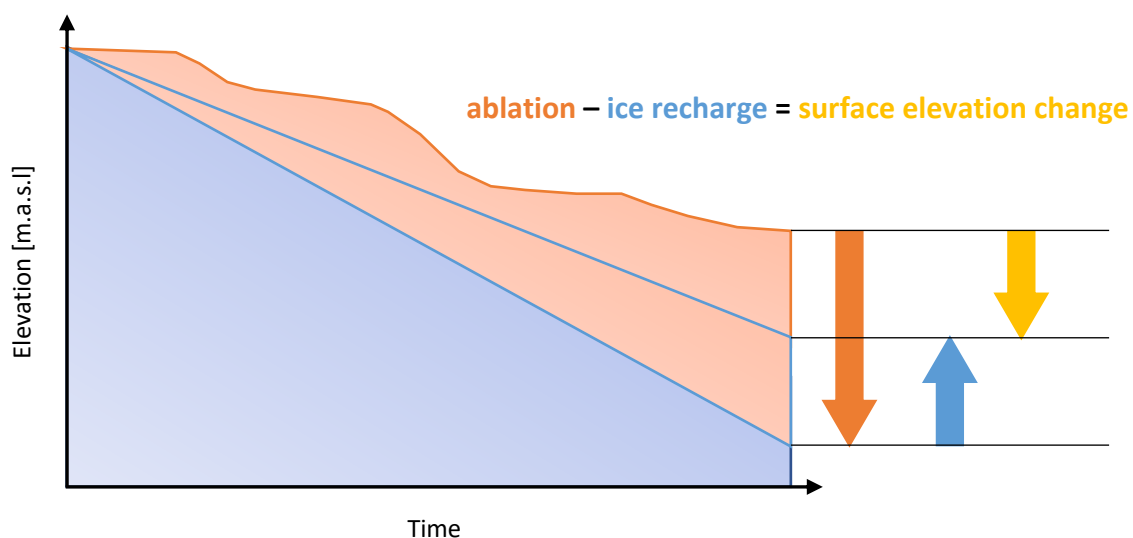


*Figure 36*: Simplified model of ablation, ice recharge and surface elevation change. Note that the ablation is assumed to be temperature-dependent, while the ice recharge is assumed to be constant.

53

### 5.11.2. Adapted Positive Degree Month Model

The regular TIM is usually used to model the melt over a single day or a single ablation period, which is then calibrated by in-situ ablation measurements. However, as mentioned above, there is one main difference for the application in this thesis, which calls for adaptions in the model: The calibration data derived from the DTMs consists of surface elevation change data, rather than ablation data.

Thus, when adapting the model to surface elevation change, which consists of both ablation as well as the ice flow, it is necessary to incorporate the ice recharge. That is the ice that constantly flows towards the margin and partly compensates the ablation at a given measurement point. For the calibration of the model, it is necessary to know the recharge rate temperature ($RRT$), which is essentially the theoretical temperature that would be needed to melt the monthly recharge (see chapter 5.11.3). For simplicity reasons, it is assumed that this is a constant (see chapter 5.11.1).

The adapted positive degree month model used in this thesis is described by Equation 11.

$$SEC_p = \left( PDM_p - \sum_{i=1}^{p} RRT \cdot i \right) \cdot PDMMF \qquad \textbf{\textit{Equation 11}}$$

Where

$$PDMMF = \Delta h \cdot \left( PDM_n - \sum_{i=1}^{n} RRT \cdot i \right)^{-1} \qquad \textbf{\textit{Equation 12}}$$

$$PDM_p = \begin{cases} \sum_{i=1}^{p}(T_i - T_t) & for\ T_p > T_t \\ 0 & for\ T_p \leq T_t \end{cases} \qquad \textbf{\textit{Equation 13}}$$

$SEC_p$        = simulated surface elevation change [m]

$T$        = air temperature (monthly value) [°C]

$T_m$        = monthly average temperature (e.g. January average) [°C]

$T_t$        = threshold temperature [°C]

$p$        = any given month

n        = number of observed months

$PDM$        = sum of monthly temperatures above $T_t$ [°C]

$RRT$        = assumed recharge rate temperature [°C]

$PDMMF$        = positive degree month melt factor [m/month/°C]

$\Delta h$        = measured cumulative surface elevation change between month 1 and n [m]

In order to simulate the surface elevation change for a given month ($SEC_p$), the cumulative assumed recharge rate temperature is subtracted from the sum of mean monthly temperatures (*PDM*) and then multiplied with the positive degree month melt factor (*PDMMF*). The PDDMF serves to align the measured cumulative surface elevation change $\Delta h$ with the cumulative temperatures. As mentioned above, the assumed recharge rate temperature (*RRT*) compensates for the surface elevation 'rise' caused by the constant ice flow from above. In other words, it is the temperature that would be needed to melt the monthly recharge. The different ways to calculate RRT are described in chapter 5.11.3.

### 5.11.3. Determining Recharge Rate Temperatures

The RRT is used to detrend the cumulative data – thus the question is, how this trend is determined. The underlying assumption with detrending is that the long-term mean represents an equilibrium state and only the deviations from this are to be taken into account.

For this thesis, two approaches are taken: One way to determine a trend is the approach with the deviation from the monthly temperature average for monthly positive temperatures ($\Delta T^+$). Another possibility is a trendline fitted to the cumulative temperature. Equation 14 shows how the detrending lines are calculated.

$$y = RRT \cdot x + b$$

*Equation 14*

$y$ = detrending line (dependent variable)

$RRT$ = assumed recharge rate temperature [°C]

$x$ = independent variable, month

$b$ = constant, equal to y, when x = 0

For both of these detrending lines, the RRT value is the slope. The final equations as well as the RRT and b values for both approaches can be viewed in Table 17. How these two approaches are executed in detail is explained below.

**Calibration of RRT Using Least Squares Trend Line**

The RRT is approximated with a trendline through the cumulative temperature data. The trendline or 'line of best fit' is calculated in *Microsoft Excel* using the least squares method and directly yields RRT as part of the trendline equation (see Equation 14). As stated above, the underlying assumption for detrending is that the long-term mean is in an equilibrium state. However, as the results will show, this is only the case before 2003 (see chapters 6.1 and 6.4). For that reason, the trendline is only generated for the time period between 1912 and 2003.

**Calibration of RRT Using $\Delta T^+$**

The deviation from the monthly temperature average for monthly positive temperatures ($\Delta T^+$) is inspired by Lozowski et al. (1989), who used cumulative monthly mean temperature anomalies to describe interannual climate variability. In this research it is used as a way to calibrate the recharge rate – something that to the authors knowledge has not been done before. Figure 37 visualizes the $\Delta T^+$-approach. The black line represents the cumulative

deviation from the monthly average if $T_p > T_T$. The different blue lines are detrended cumulative temperatures with different RRT values. Thus, the RRT value is selected as such, that the detrended cumulative temperature (positive degree months) align with the cumulative $\Delta T^+$ (see also Equation 15).

The offset of the detrending line on the y-axis for the first month recorded (*b in* Equation 14) is set to be equal to 0 for all datasets (see also Table 17). This is due to the fact that the deviations from the monthly average are also cumulated from the first month and therefore start at 0.

$$RRT = \left( \sum_{i=1}^{n} (T_i - T_T) - \sum_{i=1}^{n} \Delta T^+{}_i \right) \cdot n^{-1} \qquad \textit{Equation 15}$$

Where

$$\Delta T^+{}_p = \begin{cases} T_p - T_m & \text{for } T_p > T_t \text{ and } T_m > T_t \\ T_p - T_t & \text{for } T_p > T_t \text{ and } T_m \leq T_t \\ 0 & \text{for } T_p \leq T_t \end{cases}$$

$T$              = air temperature (monthly value) [°C]

$T_m$            = monthly average temperature (e.g. January average) [°C]

$T_t$            = threshold temperature [°C]

$p$              = any given month

n               = number of observed months

$RRT$            = assumed recharge rate temperature [°C]

$\Delta T^+$            = deviation from monthly average if $T_p > T_T$ [°C]
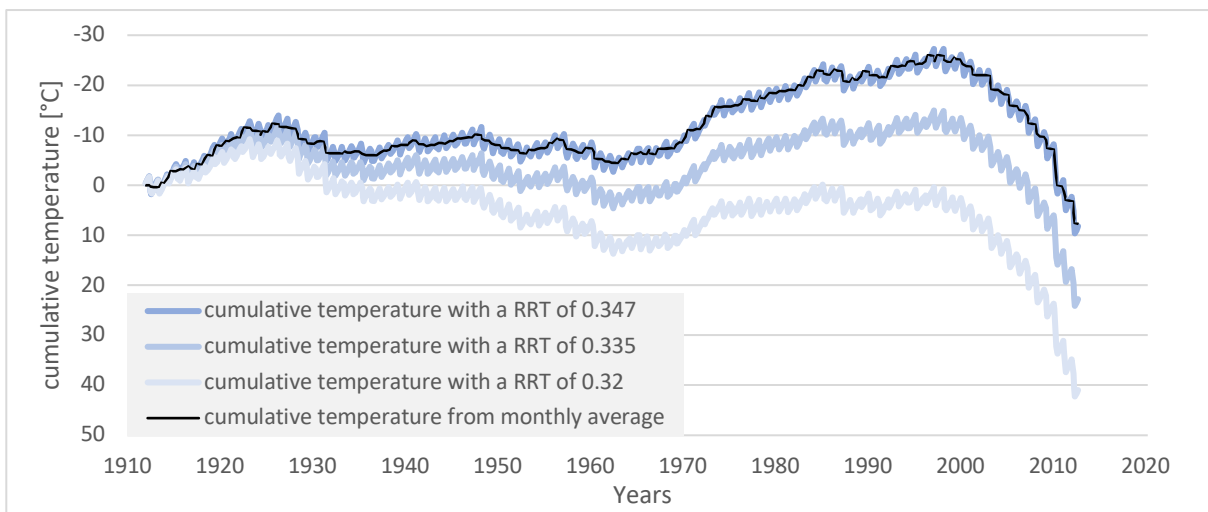


***Figure 37**: The cumulative deviation from the monthly average ($\Delta \text{T}^+$) in comparison with detrended cumulative temperatures using RRT. The curve with the calculated RRT is marked in dark blue. Other values are displayed to visualize the impact of different assumed RRTs. Exemplary temperature data from Box (2013). Note that the y-axis is inverted for ease of comparison.*

### 5.11.4. Determining the Threshold Temperatures

One important thing to note is the definition of temperatures above the temperature threshold ($T_t$). For both the *PDM* and $\Delta T^+$, a value of 0 is assumed, if the temperature of any given month ($T_p$) is smaller than $T_t$. This is in contrast to other studies (e.g. Lüthi et al. 2016), where the monthly average ($T_m$) is the decisive factor that needs to be larger than $T_t$. In practice, that would mean only considering months with a positive monthly average temperature (thus, the melting season – e.g. June, July, August). It was decided to do it differently in this paper, because all temperature anomalies above $T_t$ have an effect on glacier melt.

It was decided that for this thesis a threshold temperature ($T_t$) of 0 °C will be used. For the dataset of Box (2013), which was generated for an area very close to and about on the same elevation as the AOI, $T_t$ was therefore defined as 0 °C. However, the other two datasets are from a different region and elevation and there is therefore a temperature gradient (lapse rate) present. One way to align them, is to employ the general dry adiabatic lapse rate, which determines that temperature changes with a rate of about -0.98 °C/100m of increasing elevation (Hemond & Fechner 2015). This is a rather general approach though and may not represent the actual data very accurately. A data centered approach reduces this risk. Since mostly the positive temperatures play a role for glacier melt, it was decided to simply look at the mean of the warmest month of each of the years where the three datasets overlap for this thesis. The offset between the means was then inversed to get the threshold temperature $T_t$ (see Table 11).

*Table 11: Overview of the long-term temperature datasets and their offsets to each other.*

| temperature dataset | mean of warmest month (1996-2012) | difference to Box (2013) ($\triangleq -T_t$) |
|---|---|---|
| **Swiss Camp** | 0.7 °C | -1.8 °C |
| **Ilulissat** | 8.3 °C | +5.8 °C |
| **Box (2013)** | 2.5 °C | ±0 °C |

### 5.11.5. Calculating Melt Rates

Given the assumption that ablation (surface melt) is made up of a combination of the surface elevation change as well as a constant recharge (see Figure 36), we can now aim to calculate the total melt and the melt rates for the periods of known surface elevation change.  To do so, we first have to convert the assumed recharge rate temperature (*RRT*) to the actual recharge rate (*RR*) in m/month. Since the relation between temperature and melt is described by the positive degree month melt factor (*PDMMF*), Equation 16 will deliver the *RR*. Thus, the *RRT* is multiplied by the *PDMMF* in order to calculate the actual recharge rate (RR) in meters per month. Because they are calculated with the melt factor, the results are essentially negative melt values and in order to get the surface rise (positive recharge rate) values, they have to be inverted. The results for *RR* and all temperature datasets are shown in Table 17.

$$RR = -(RRT \cdot PDMMF)$$
<div align="right">*Equation 16*</div>

$RR$ = recharge rate [m/month]

$RRT$ = recharge rate temperature [°C]

$PDMMF$ = positive degree month melt factor [m/month/C°]

With the *RR* value known, it is possible to calculate the melt rate in m/y between two times for which the elevation is known (thus the acquisition date of a DEM). This is done by solving Equation 17, where the calculation of the uncertainty is included. The uncertainties of the two datasets being compared are added, divided by the amount of days and then multiplied by 365. Hence the uncertainty of the elevation change per duration is not only dependent of the uncertainty associated with the input datasets, but also of the duration between the acquisition of the earlier and later dataset, whereat a shorter duration will increase the uncertainty.

$$mr_{1,2} = \left( [(h_2 \pm \sigma_2) - (h_1 \pm \sigma_1)] \cdot \frac{365}{t} \right) - (12 \cdot RR)$$
<div align="right">*Equation 17*</div>

Where

$mr_{1,2}$ = melt rate between time 1 and time 2 [m/y]

$h_2$ = elevation of the later dataset [m]

$\sigma_2$ = uncertainty associated with the later dataset (standard deviation) [m]

$h_1$ = elevation of the earlier dataset [m]

$\sigma_1$ = uncertainty associated with the earlier dataset (standard deviation) [m]

$t$ = duration between acquisition of the earlier and the later dataset [d]

$RR$ = monthly recharge rate [m/month]

# 6. Results

## 6.1. Ice Extent

The ice sheet margin at Nunap Kigdlinga is rather diffuse and often covered by a lot of snow and moraine material, which makes distinguishing the exact position of the margin rather difficult (see also Figure 3). Additionally, the margin has hardly moved at all over the last century, as can be seen in Figure 38. The lake in the foreground is still present, albeit shallower than in 1912. The moraine in the background is still roughly at the same position, but has considerably lowered, as is apparent on the image on the right, where both the current moraine crest is visible, as well as the historic one is marked (orange). More images showing the Nunap Kigdlinga forefield over time can be found in Appendix C (Figure 87).



*Figure 38*: Nunap Kigdlinga ice sheet margin in 1912 and 2018 as seen from Sondagsfjell (facing north-east). The GrIS surface and the lake extent of 1912 are marked in the 2018 image in orange and blue respectively. Images taken by P.L. Mercanton (de Quervain & Mercanton 1920) and S. Schudel.

The ice margin at Sermeq Kujalleq on the other hand has undergone a strong retreat since the first recordings in 1912. In total, an area of about 0.7 km² became exposed from the ice (see Figure 40). The 1912 margin depicts the furthest advance recorded, but the other ice margin positions recorded between then and 2003 (namely 1959, 1964 and 1985) are all comparably similar. Unfortunately, the scanned oblique aerial image of 1949 (see Figure 14), is not sufficient for mapping, but it does show Sermeq Kujalleq in a similar extent as in 1912 and 1959. While the data coverage is unevenly distributed (higher data availability in recent years), it is clear that the major phase of retreat started only after 2003. The last 15 years showed an almost linear retreat with the 2018 position receded further than ever directly recorded before. In the steep area of Sermeq Kujalleq there is now also a rock window, which first appeared in 2014 and has increased in size since then (see Figure 39). A lake of about 12'000m² has formed behind the large terminal moraine (see Figure 91 in Appendix C).



*Figure 39*: First image of the rock window (red circle) in the Sermeq Kujalleq glacier. Image by M. Lüthi (2014).
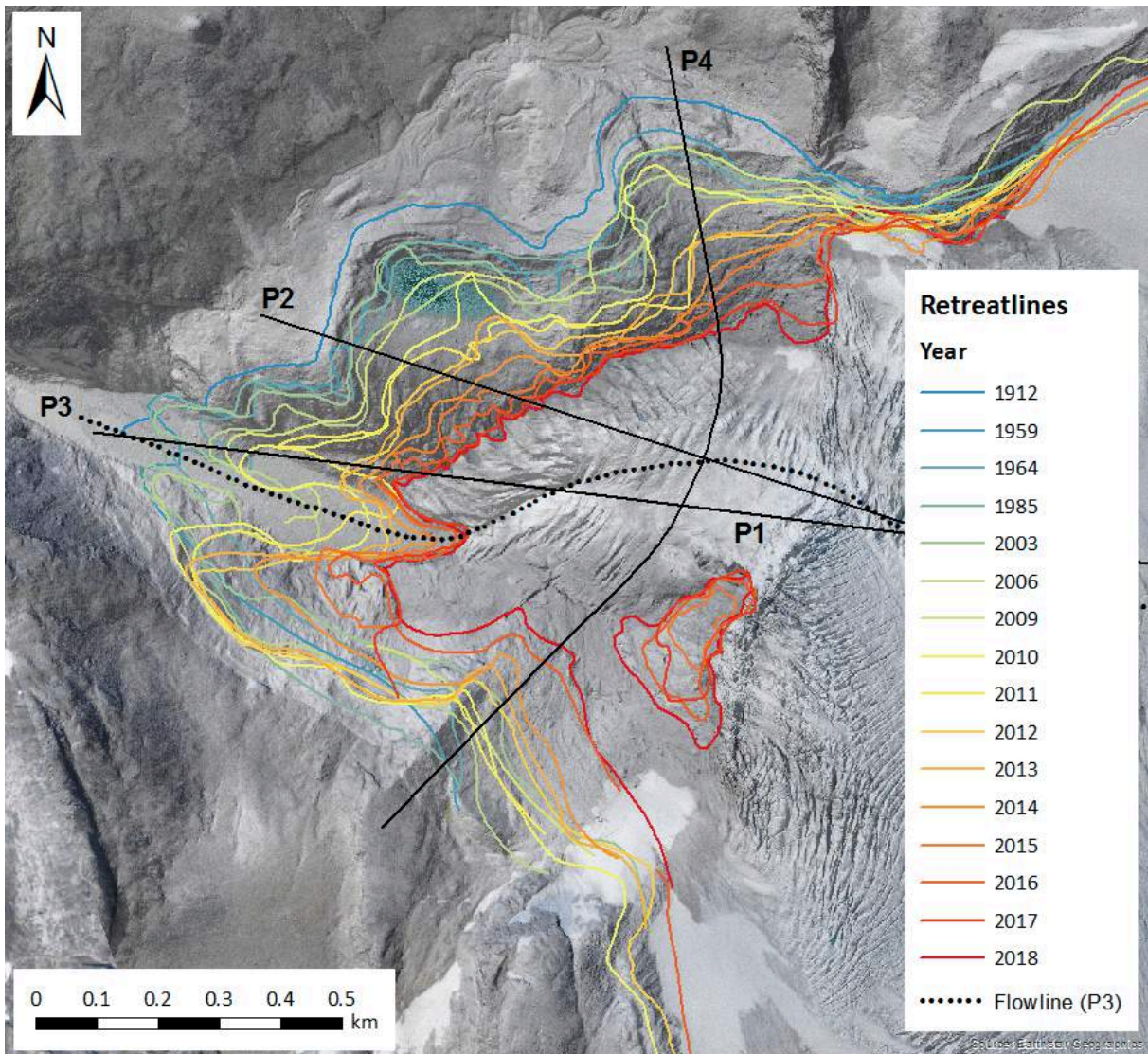
**Figure 40**: *Retreat of the Sermeq Kujalleq ice lobe from 1912 to 2018. For the different sources, refer to Table 10. The background image consists of the orthophoto and hill shade of the 2018 drone campaign. Marked are also the different profiles P1 – P4.*

**Table 12**: *Qualitative assessment of the trend of the analyzed retreat lines marked in Figure 40 based on the terminus character, namely steepness and form. 'A' stands for 'advancing', 'S' for 'stagnant' and 'R' for retreating. For more information about the datasets of each year, refer to Table 10.*

| 1912 | 1959 | 1964 | 1985 | 2003 | 2006 | 2009 | 2010 | 2011 | 2012-2018 |
|------|------|------|------|------|------|------|------|------|-----------|
| A | S | R/S | A/S | A/S | R/S | A/S | R | R/S | R |
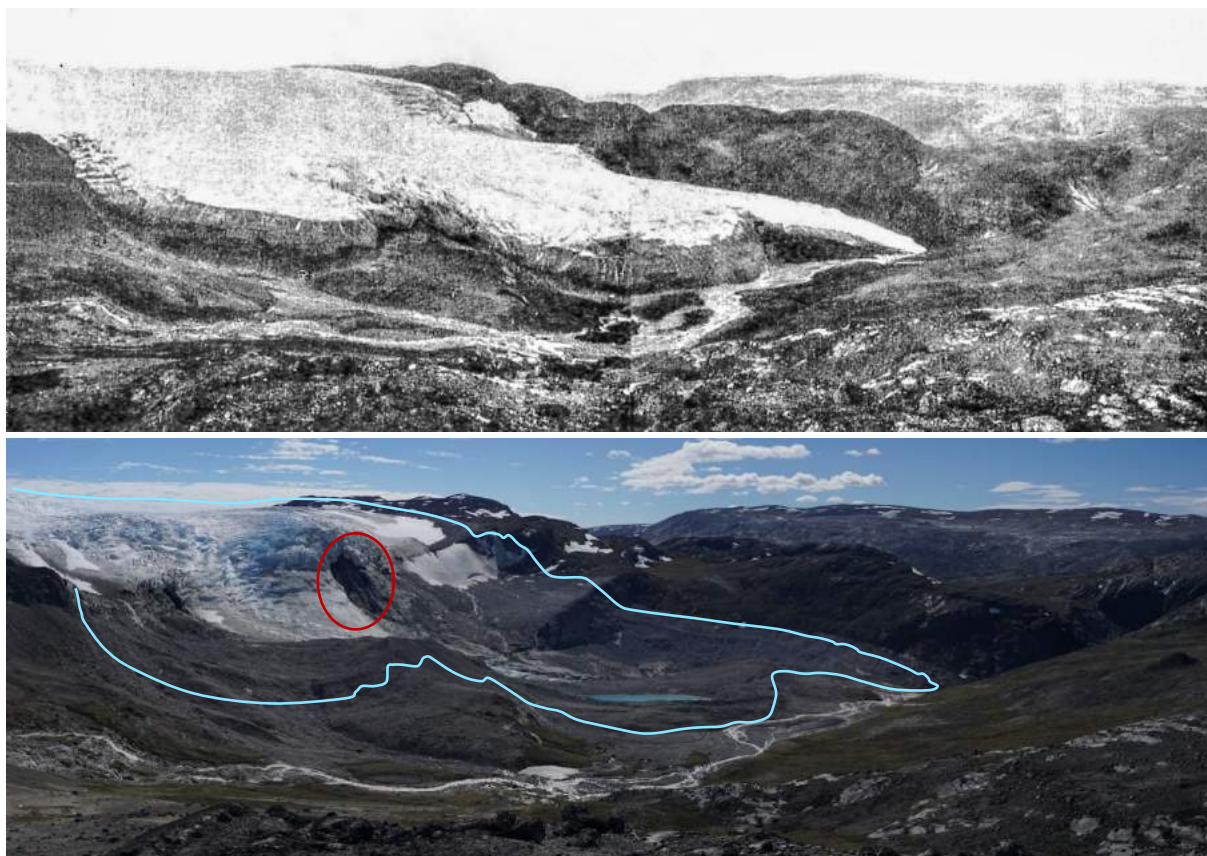
***Figure 41***: *Sermeq Kujalleq in 1912 and in 2018 as seen from de Quervain and Mercantons reference point 'A' (see Figure 73 in Appendix A or Figure 86 in Appendix C for location) facing south. The ice extent of 1912 is marked on the 2018 image in light blue. Pictures taken by P.L. Mercanton* (de Quervain & Mercanton 1920) *and Simon Schudel. Note the increased size of the rock window (red circle) in comparison with 2014 in Figure 39.*

These general quantitative observations also agree with the brief qualitative assessment of the character of the glacier terminus as described in Table 12. The appearance of the glacier termini can hint towards the recent development of the glacier (retreat, stagnation or advance) on a qualitative level (Benn & Evans 2010). Typically, an advancing glacier showcases a rather steep, convex terminus with a round, lobe-like shape, while a retreating glacier terminus often displays a rather flat terminus with a less uniform margin. Of course these are very vague descriptions and are highly subjective to the viewer, but the assessment of the available aerial imagery shown in Table 10, as well as the terrestrial imagery (1912, 2016, 2018 – see also Figure 41) is still rather clear: While there are mixed results until 2009, the retreat tendency in the last decade has been very strong. The only position recorded with a clearly advancing terminus was in 1912. The textbook example with the steep, convex terminus is perfectly visible in the top image of Figure 41. The terminus in 1912 is even described to override patches of vegetation (salix repens, rhododendron laponicum), an indication that the glacier had reached an area previously non-glaciated for a long period (de Quervain & Mercanton 1920; Rabot & Mercanton 1913).

## 6.2. Co-Registration

For all analyzed DTMs, the co-registration process improved the mean error as well as the standard deviation in comparison with the stable terrain of the master DEM (ADcomp). Two to three iterations of the co-registration process were necessary, until the two control values reached their possible optimum. The total applied corrections for all three directions x, y and z depended a lot on the dataset, but datasets of the same origin and acquisition technique usually had very similar corrections. A full overview of the results of the co-registration is presented in Table 13 for all datasets with a resampled resolution of 2m and in Table 14 for all datasets with a resampled resolution of 10m. For the higher resolution DEMs, the mean error could be reduced to less than ±0.1m, while the standard deviation was usually reduced by about 1-2m to a value of 1-4m. The total applied corrections differed considerably for x, y and z. For the x-axis, corrections of up to -12.3 m were necessary, while for z-axis, corrections of not more than 3m were executed.

*Table 13: Results of the co-registration process of all DEMs in 2m resolution. Included is descriptive information (mean and standard deviation) on the difference-grid of the stable terrain before and after the co-registration. Also included is the number of co-registration iterations needed to get the best result. The last columns contain the total corrections applied in x-, y- and z-direction.*

| Dataset | | Dh of the stable terrain before and after co-registration [m] | | Nr. of Iterations needed | Applied corrections [m] | | |
|---|---|---|---|---|---|---|---|
| | | Mean | Std. deviation | | $\Delta x$ | $\Delta y$ | $\Delta z$ |
| DR18 | before | +1.93 | 3.48 | 3 | -9.6 | -1.6 | +1.8 |
| | after | -0.01 | 2.62 | | | | |
| DR16 | before | +3.32 | 5.09 | 2 | -9.9 | +1.6 | +3.0 |
| | after | +0.09 | 4.05 | | | | |
| AD17 | before | -0.75 | 3.53 | 3 | -12.3 | -3.6 | -1.1 |
| | after | -0.04 | 1.37 | | | | |
| AD16 | before | -1.55 | 3.24 | 2 | -9.9 | -6.7 | -1.8 |
| | after | -0.04 | 1.47 | | | | |
| AD15 | before | +0.45 | 3.52 | 2 | -12.0 | -5.5 | -0.1 |
| | after | +0.03 | 1.12 | | | | |
| AD14 | before | +0.69 | 2.78 | 2 | -5.4 | -0.8 | +0.3 |
| | after | ±0.00 | 1.33 | | | | |
| AD13 | before | +0.09 | 2.63 | 2 | -8.6 | -2.8 | -0.1 |
| | after | +0.04 | 1.79 | | | | |

For the lower resolution datasets, the largest applied corrections as well as the most improved mean error were the ASTER datasets, as well as SFM59. Reductions of the mean error by 50m and more are common. Overall, the mean error is reduced to less than 0.3m, while the standard deviation was reduced by up to 12m. Still, the resulting standard deviations are rather high with values of 6-10m for the ASTER DEMs and 12.6m for SFM59. The applied corrections reached values of up to 92m ($\Delta y$ for SFM59) and 30-60m for the ASTER DEMs (especially in the x- and z-axis). This seems like a lot but considering the original data resolution of 30m for the ASTER DEM, these corrections all range between one and three pixels.

*Table 14: Results of the co-registration process of all DEMs in 10m resolution. Included is descriptive information (mean and standard deviation) on the difference-grid of the stable terrain before and after the co-registration. Also included is the number of co-registration iterations needed to get the best result. The last columns contain the total corrections applied in x-, y- and z-direction.*

| Dataset | | Dh of the stable terrain before and after co-registration [m] | | Nr. of Iterations needed | Applied corrections [m] | | |
|---|---|---|---|---|---|---|---|
| | | Mean | Std. deviation | | $\Delta x$ | $\Delta y$ | $\Delta z$ |
| AS16 | before | +49.37 | 14.52 | 3 | -61.3 | +12.8 | +46.8 |
| | after | +0.06 | 6.72 | | | | |
| AS10 | before | +52.82 | 9.72 | 3 | -33.0 | -8.9 | +51.4 |
| | after | +0.1 | 7.35 | | | | |
| AS03 | before | +54.32 | 12.84 | 3 | -41.7 | +0.6 | +52.5 |
| | after | +0.11 | 9.72 | | | | |
| GD0309 | before | +10.10 | 9.3 | 2 | +0.3 | -22.6 | +10.4 |
| | after | -0.46 | 7.85 | | | | |
| AE85 | before | +0.29 | 5.25 | 2 | -9.7 | -8.2 | -0.4 |
| | after | +0.23 | 4.89 | | | | |
| SFM59 | before | +38.15 | 24.09 | 3 | -71.6 | +92.4 | +34.9 |
| | after | +0.21 | 12.63 | | | | |

### 6.2.1.    Elevation-Dependent Bias for SFM59

As shown in Figure 42, the bias between ADcomp and SFM59 may be partly dependent of the elevation. There seem to be two clusters: One where it would be expected around 0 (outlined in orange). The other, marked in blue, shows a rather clear correlation between elevation and dh-values. Why this is the case could not be determined and would need further investigation. Most probable causes are effects of wrong estimations of camera locations (altitudes) and/or camera properties. The resulting effect will also translate into the DEM differencing process and affect those results. One example is  Figure 76 (Appendix B) where the 2018 drone DEM is subtracted from SFM59. The lowest areas in the valley are marked in red, which means that the SFM59 value is higher than in DR18, while the mountain tops are marked in green, which means that the SFM59 value is lower than in DR18. This could possibly be an effect of different spatial resolutions (see chapter 7.2.4), but in this case not just the valley floors and the mountain tops are affected, but whole lower and higher lying areas. In short, SFM59 has the tendency of overestimating low areas and underestimating high areas, which has to be remembered when analyzing results in connection to this dataset.
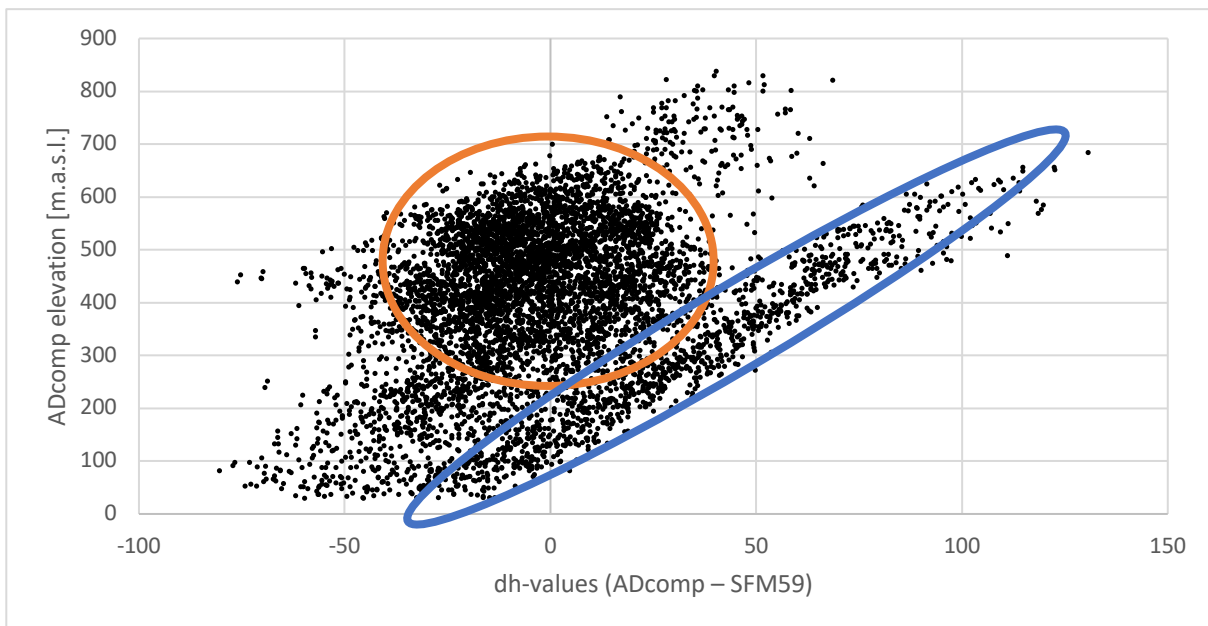


***Figure 42****: Elevation dependent bias of the DEM created with SFM from the 1959 aerial images. Two distinct clusters are delineated in orange and blue. Stable terrain of the whole extent of SFM59 was considered for this graph.*

## 6.3.    DEM Quality and Uncertainty Assessment

### 6.3.1.    Check for Normal Distribution

Firstly, the errors of each DTM are checked for normal distribution. As stated in Höhle & Höhle (2009) and in chapter 5.7, this is done on a visual basis. If compared to the expected Gaussian distribution Figure 43, the histograms of all datasets show a non-normal distribution of the errors $\Delta h$.
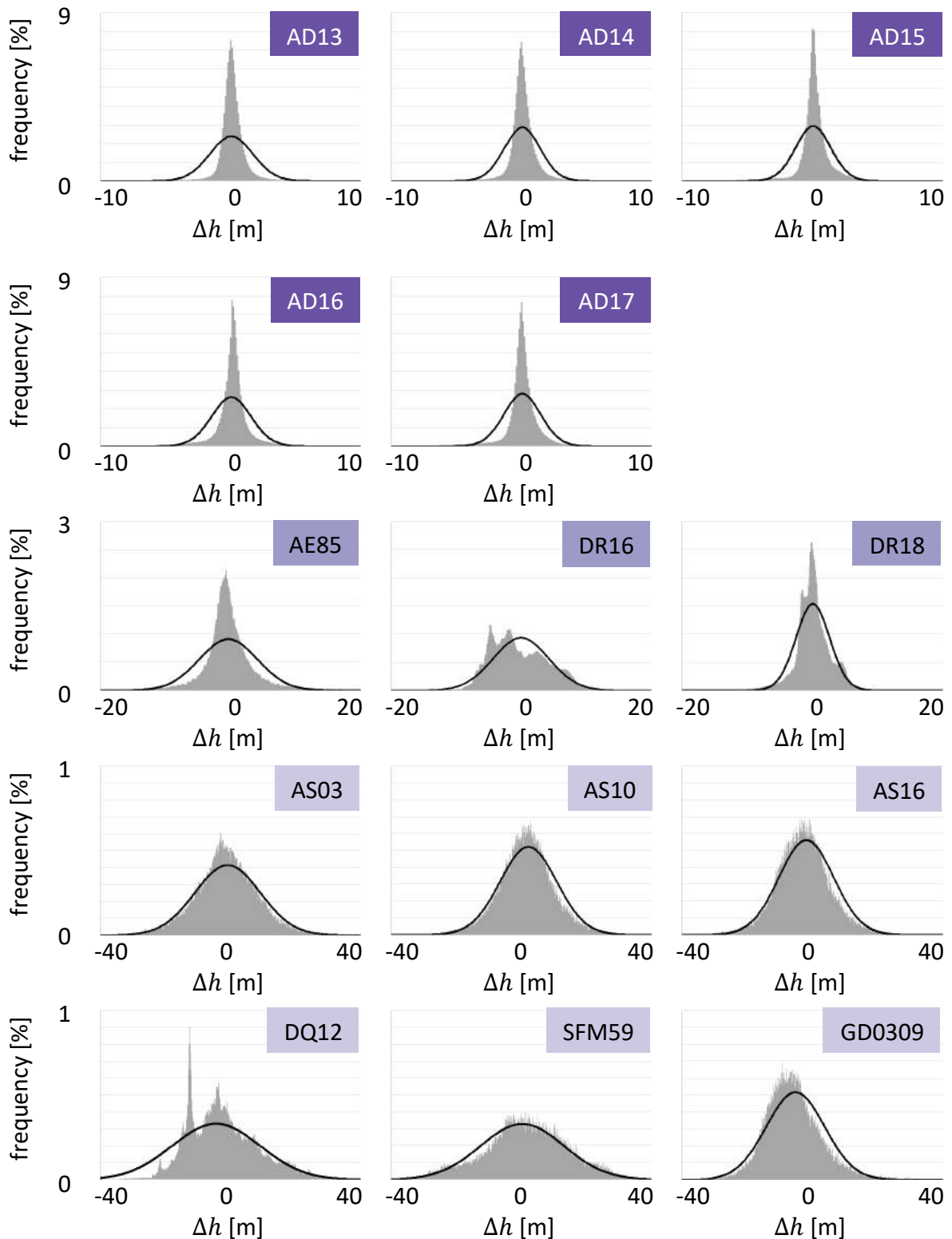
**Figure 43**: Histograms of the Δh-values for each of the DEMs over stable terrain (gray). In order to display histograms, the float pixel values were aggregated in classes of 0.1m. The frequency of each of these pixel-classes is marked in relation to the total number of pixels for ease of comparison (frequency in %, y-axis). Superimposed is the expected normal distribution of the respective dataset (black). Note that the datasets have been assigned to three different groups (1=dark purple, 2=purple, 3=light purple) with similar values for ease of comparison (see also Figure 44). Note that the graphs were truncated at ±10m for group 1, at ±20m for group 2 and at ±40m for group 3.

65

For ease of comparison, the datasets are assigned to three quality groups (see also Figure 44):

- **Group 1** (dark purple) consists of the ArcticDEM snapshots. Their errors are almost all within ±10m.
- **Group 2** (purple) consists of the AeroDEM (AE85) as well as the DroneDEMs. Their errors are almost all within ±20m.
- **Group 3** (light purple) consists of the ASTER DEMs, the DQ12, SFM59 and the Gimp-DEM. Their errors are almost all within ±40m.

Interestingly there is a dataset from each quality group for the year 2016 (see also Figure 48 and Figure 50). Due to the different spreading of errors for these three datasets, the histograms as well as the expected Gaussian distribution are very different from each other. For a visual comparison, the expected Gaussian distribution for each of those datasets is plotted in Figure 44.
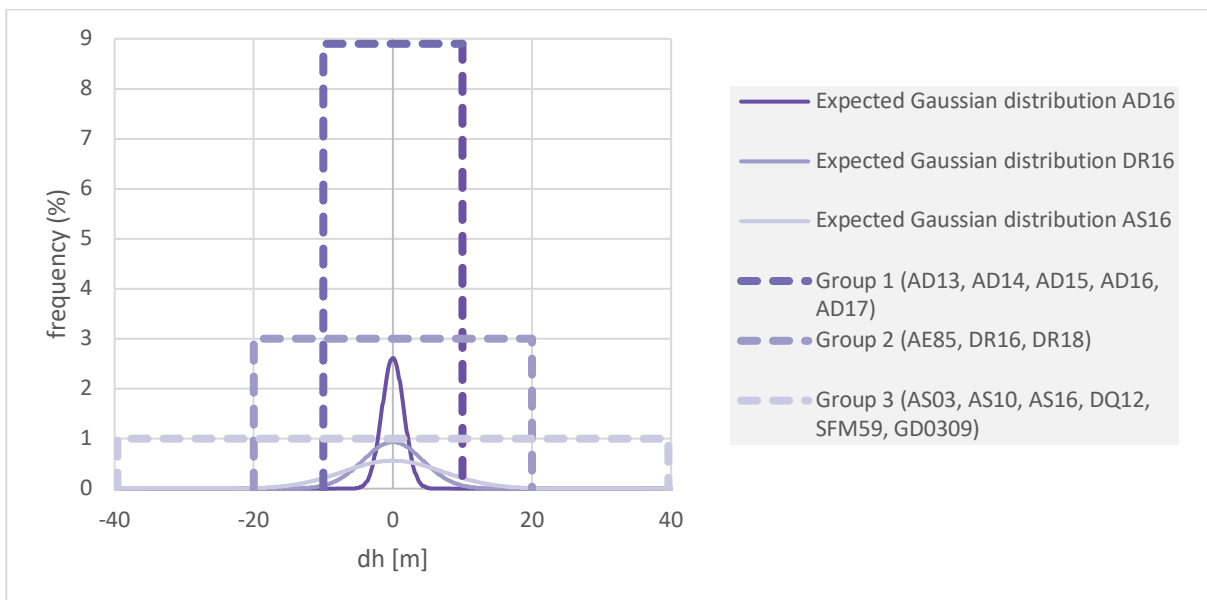


***Figure 44***: *Expected Gaussian distributions for different DEM qualities (exemplary datasets AD16, DR16 & AS16). Marked are also the extents of the graphs shown in Figure 43 for each of the three groups.*

### 6.3.2.  Robust Accuracy Measures

The fact that all datasets are non-normally distributed calls for robust accuracy measures for non-normally distributed datasets as proposed by Höhle & Höhle (2009). They are listed for all DTMs used in this thesis in Table 15 (for non-robust measures of uncertainty, namely the mean error and standard deviation, consider Table 13 and Table 14 in chapter 6.2). If they are ordered according to the NMAD, the same quality groups as in chapter 6.3.1 can be detected: The datasets in group 1 (dark purple) all have a NMAD of less than 0.7m, while datasets in group 2 (purple) have a NMAD of about 2-5m. The datasets of group 3 (light purple) have a NMAD of 6 to 12m.

*Table 15*: *Accuracy measures for the different DEMs used in this thesis. All data only relates to the stable terrain area (see chapter 5.5.3). The ArcticDEM composite was used as the reference dataset. The datasets are ordered by the NMAD. The colors represent the three quality groups (1=dark purple, 2=purple, 3=light purple).*

| | Resolution | NMAD [m] | 50% Quantile (Median) [m] | 68.3% Quantile [m] | 95% Quantile [m] |
|---|---|---|---|---|---|
| **AD15** | 2m | 0.59 | 0.04 | 1.52 | 5.31 |
| **AD13** | 2m | 0.62 | 0.01 | 2.19 | 10.93 |
| **AD17** | 2m | 0.64 | -0.02 | 2.00 | 6.67 |
| **AD14** | 2m | 0.64 | 0.00 | 1.92 | 8.03 |
| **AD16** | 2m | 0.65 | 0.13 | 2.05 | 6.31 |
| **DR18** | 2m | 1.99 | -0.10 | 2.93 | 6.23 |
| **AE85** | 10m | 2.30 | -0.27 | 3.35 | 11.62 |
| **DR16** | 2m | 4.80 | -1.03 | 5.13 | 8.41 |
| **AS16** | 10m | 6.39 | -0.83 | 7.15 | 15.67 |
| **AS10** | 10m | 6.64 | -0.54 | 7.45 | 17.31 |
| **GD0309** | 10m | 6.64 | -1.21 | 7.66 | 16.98 |
| **AS03** | 10m | 8.27 | -0.55 | 9.57 | 21.26 |
| **DQ12** | 10m | 10.26 | 0.75 | 10.45 | 23.64 |
| **SFM59** | 10m | 11.56 | 1.05 | 13.00 | 25.26 |

In general, it can be noted that the different data source seems to be the main factor influencing the data quality. Or in other words, all ArcticDEMs have very similar values, as do the ASTER DEMs. There is also a tendency in terms of the age of the data: The newer the data, the lower the NMAD value and therefore the higher the quality of the data. And last but not least, higher spatial resolution also leads to a better quality of the data. One thing to mention about the ArcticDEMs is that their high quality could be expected, because they are compared to ADcomp, which is made up of several ArcticDEM snapshots and is therefore naturally going to be very similar to single ArcticDEM datasets.

## 6.4.    Surface Elevation Changes

### 6.4.1.    Planar Surface Elevation Change Maps

The maps of surface elevation change between the different datasets and DR18 are presented in Figure 45 along with the ice extents of the two compared time periods. Note that the color scale is different for each of the comparisons. It is a 'minimum-maximum' color-stretch with the same color intensities for values above and below zero. For a detailed and enlarged overview of the comparisons, refer to Appendix B.

The surface lowering at the Sermeq Kujalleq terminus, which is the most striking development is visible in all comparisons. Other than that, it is also clearly visible that the rest of the ice has undergone a surface lowering before 2018. The different qualities of the datasets are also visible. The data gaps due to the removal of high-noise areas (see chapter 5.6.1) and the removal of interpolated data (see chapter 5.6.2) are especially frequent for SFM59, AE85 and the ASTER DEMs. Apart from AE85, these are also the datasets with the largest deviations in the non-ice-covered areas. Deviations of a couple dozen meters are possible in some of these datasets. A possible explanation can be found in chapter 7.2 and especially in chapter 7.2.4.

## DR18-DQ12



±143m

## DR18-SFM59



±145m

## DR18-AE85



±135m

## DR18-AS03



±139m

## DR18-GD0309



±112m

## DR18-AS10



±85m

## DR18-AD13



±57m

## DR18-AD14



±60m

## DR18-AD15



±45m

## DR18-AD16



±40m

## DR18-AD17



±32m

**Figure 45**: *Overview of the dh-grids of the time periods between the respective datasets and 08.07.2018 (DR18). The solid black line represents the ice extent at Sermeq Kujalleq in 2018, while the dotted line represents the ice extent of the time of the respective dataset. Enlargements of these images as well as the proper legends for each of the comparisons can be viewed in Appendix B.*

69

### 6.4.2.   Elevation Profiles Nunap Kigdlinga

For the Figures, where only the subarea of Nunap Kigdlinga is at the focus of attention (namely Figure 47, Figure 53, Figure 54), the SFM59 dataset showed a clear elevation bias (see also chapter 6.2.1) in comparison with the leveling data available from the same year (Bauer 1968c). In Table 16, the five control points which were measured in 1959 are compared to the SFM59 dataset and the mean z-offset is determined to be -16.4m. For all figures mentioned above, SFM59 was fitted to the leveling data by applying an offset correction of 16.4m.

*Table 16*: *Calculation of the necessary Z-offset correction in order to fit SFM59 to the levelings of the same year in the sub-area of Nunap Kigdlinga. The elevation from Bauer* (1968c) *was co-registered to the rest of the data with the elevation information of the control-point A14.*

| Points | Elevation from Bauer (1968c) [m] | | Elevation from SFM59 [m] | Offset of SFM59 [m] |
|---|---|---|---|---|
| | original | after co-registration (+26.4) | after co-registration | |
| **B 21** | 635.7 | 662.1 | 636.6 | **-25.5** |
| **B 23** | 709.5 | 735.9 | 720.9 | **-15** |
| **B 24** | 706.9 | 733.3 | 721.7 | **-11.6** |
| **BK 1** | 611.4 | 637.8 | 616.5 | **-21.3** |
| **Y** | 592.4 | 618.8 | 610.3 | **-8.5** |
| **Mean** | | | | **-16.4** |

The elevation profiles of this chapter were created along the profiles marked in Figure 46. For Nunap Kigdlinga this is P0 with additional points added from historic levelings. Some points which were not located directly on the profile were translated onto the closest point on the profile as mapped in Figure 46. For Sermeq Kujalleq, there is one longitudinal profile along the flow line of the glacier (P3), and one cross-section (P4).
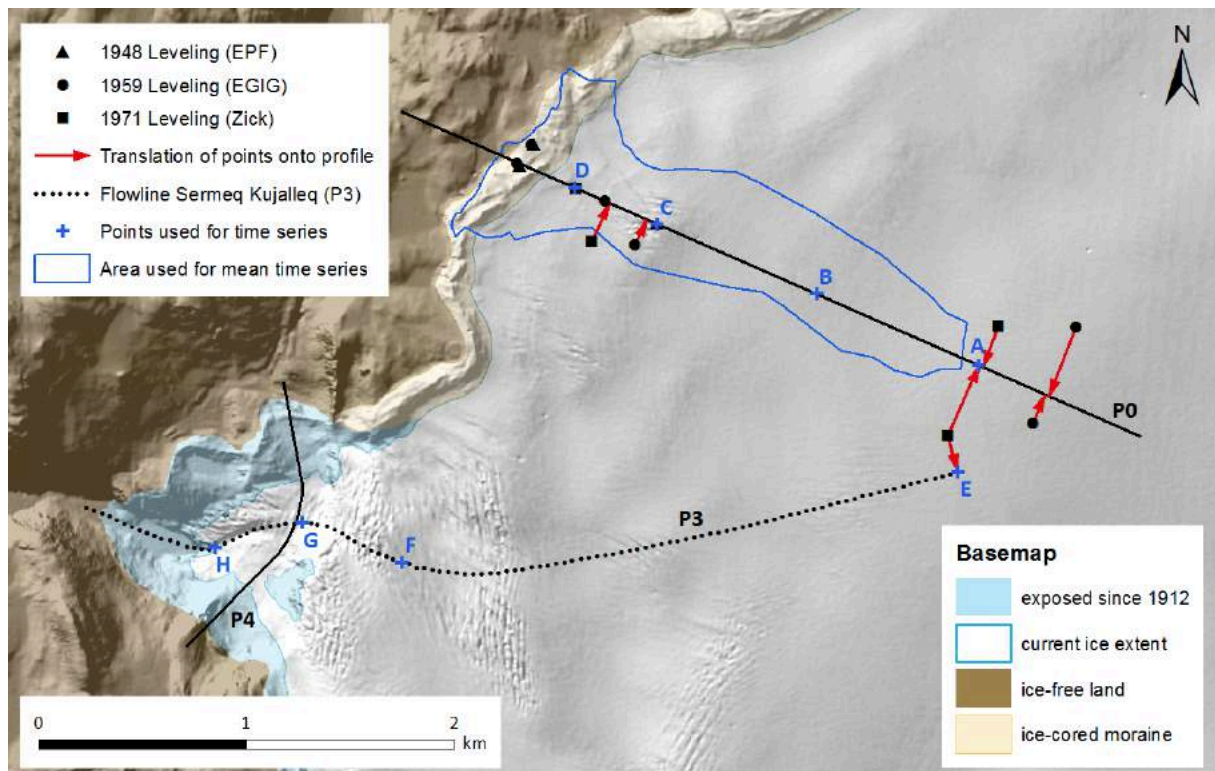
*Figure 46*: *The profiles used to generate the elevation profiles in Figure 47 to Figure 51, the points (A-H) used to generate the time series in Figure 53 and Figure 55, as well as the area used to generate the time series in Figure 54.*

The different qualities of the datasets used is apparent at first sight in Figure 47: While DQ12, GD0309, the ArcticDEMs and DR18 display comparably smooth surfaces, there are large variations especially in the ASTER snapshot datasets (AS03 and AS10). Since the ice surface is in fact rather flat, these variations have to be seen in the light of data uncertainty. The uncertainty (standard deviation) over stable terrain range between 7 and 10m for the ASTER snapshot datasets and are around 5m for the AeroDEM (see Table 14). However, this could be even higher over areas of ice where the contrast is much lower and data acquisition more difficult. Because there is no reference data of the ice for the period in question, there is no way to check this though. In any case the data of AS03, AS10, AE85 and to smaller extent also SFM59 have to be treated with some skepticism. Nonetheless, the changes between 1912 and 2018 are striking and match the changes visible on the images taken in 1912 and 2018 (see Figure 38).
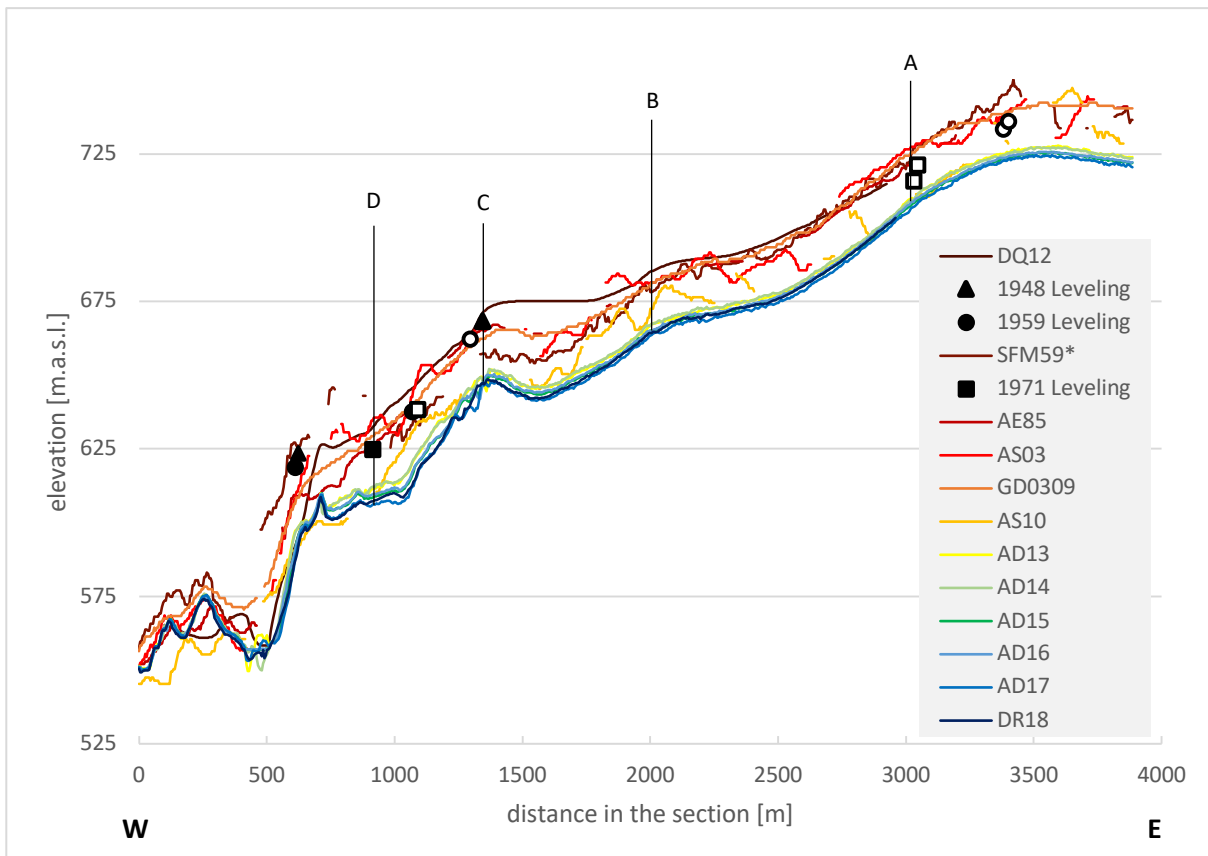
***Figure 47***: *The P0 profile of Nunap Kigdlinga over time. The location of the profile is marked in Figure 46. The GimpDEM (GD0309) is marked with a dotted line, because this data is a result of a temporal composite. The 1959 SFM dataset is marked with a (\*), because it was adapted to fit the leveling points of 1959 in this area. The symbols of the levelings are hollow if the point does not lie directly on the profile. In this case, their values were translated to the nearest point on the profile. The current ice margin is located at about the 500m mark on the x-axis.*

Note also the area from 0 to 500m on the x-axis in Figure 47, which corresponds to the more or less stable forefield of the ice margin. The ice margin today is more or less at the same spot as it was in 1912. However, several datasets in between (SFM59, AE85, AS03 and even GD0309) suggest, that it had temporally advanced by a few dozen meters. The disagreement between the different datasets in the so-called stable areas is rather high. Hence it may make more sense to look at the time series of the four marked points A, B, C and D in Figure 53 or the mean of a larger area in Figure 54, where all measurements are equipped with an appropriate value of uncertainty (standard deviation, see Table 14).

72
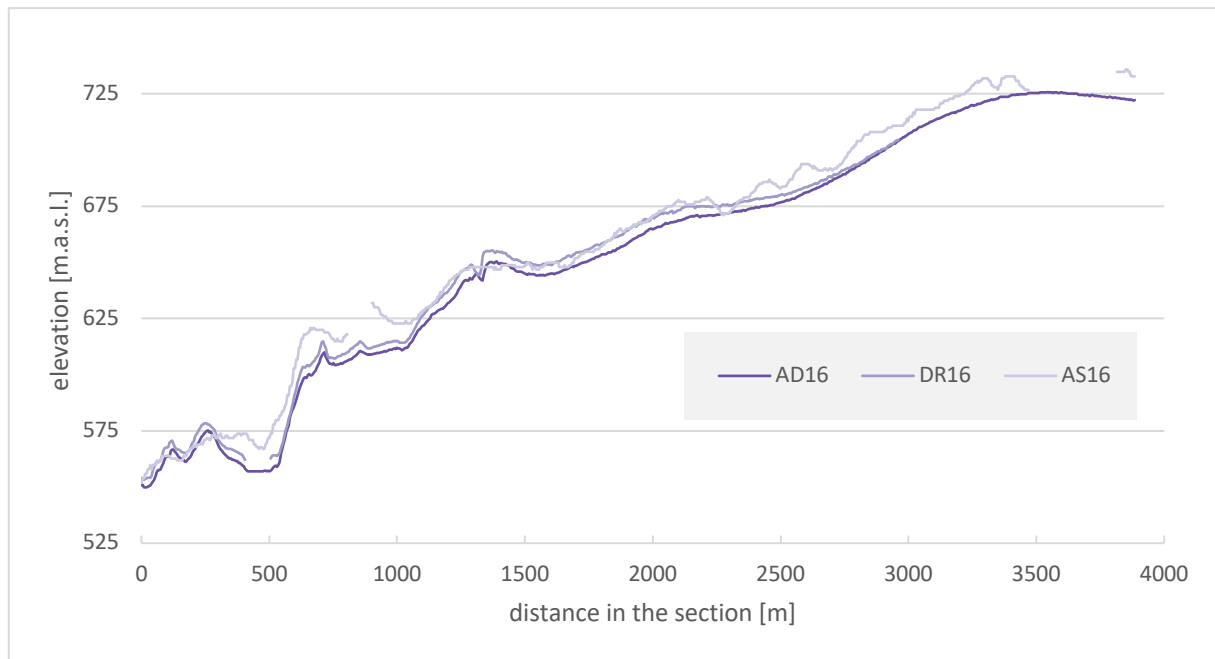
***Figure 48***: *Comparison of the Nunap Kigdlinga cross-section (P0) of three DTMs of 2016 generated and acquired in different ways. They can be seen as exemplary DEMs of the three different quality groups and are colored accordingly.*

In Figure 48 the three available 2016 datasets are compared. They are marked in the colors of the three quality groups: Dark purple for the highest quality group 1, purple for group 2 and light purple for the lowest quality group 3 (see chapter 6.3). Note that for the profile in Figure 47, only AD16 from the highest quality group was considered. The three datasets should deliver more or less the same results as they were all acquired within 6 months. However, there seems to be an issue with DR16, which has a systematic offset compared to the AD16 (see also chapter 7.3.2). And for the AS16 dataset, the limitations become obvious: As stated above, the surface smoothness is not represented correctly in these datasets (see also chapter 7.2.2).

### 6.4.3. Elevation Profiles Sermeq Kujalleq
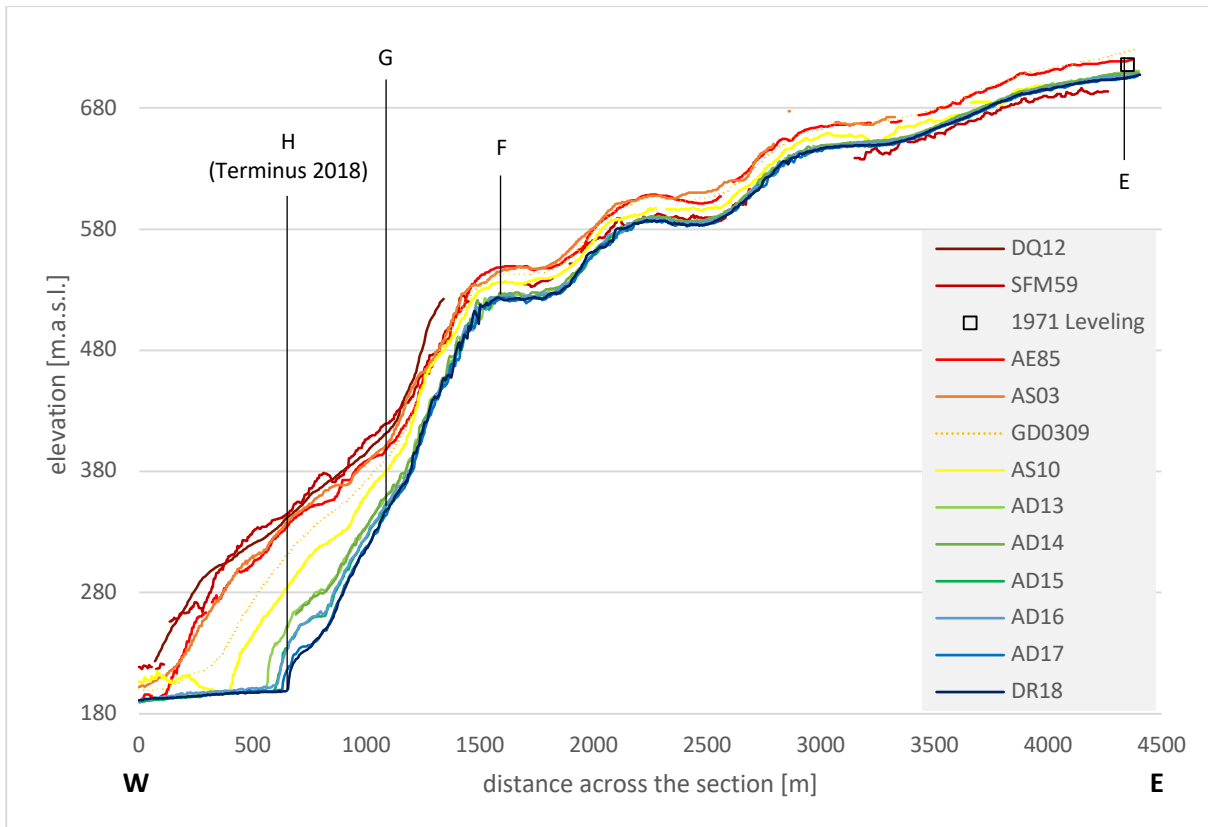


***Figure 49***: *Longitudinal section along the flowline of Sermeq Kujalleq (P3) over time. The location of the profile is marked in Figure 40 and Figure 46. The GimpDEM (GD0309) is marked with a dotted line, because this data is a result of a temporal composite. Note that the point of the 1971 leveling was not located directly on the profile and was therefore projected to the nearest location on the profile. For the exact location, see Figure 46.*

In comparison to Nunap Kigdlinga (see Figure 47), the ASTER and AeroDEM data for Sermeq Kujalleq seems to be less affected by large variations caused by data uncertainty. This allows for a more undistracted look at the temporal development of the flow profile of Sermeq Kujalleq. The development is clear and only goes in one direction: After relatively stable elevations from 1912 to 2003, there is a massive retreat and thinning for the whole glacier area, resulting in the drastic change also visible in the image comparison in Figure 41. In the lower areas, where surface elevation changes of up to 130m are observed, this thinning seems to be much stronger than in higher areas (see also Figure 55). The SFM59 dataset is the only one that in part (especially in higher areas) does not agree with this general development. However, in light of the partial elevation-dependent bias of that dataset (see chapter 6.2.1), which causes too low elevations in higher areas and too high elevations in lower areas, this may be an issue of data-quality.
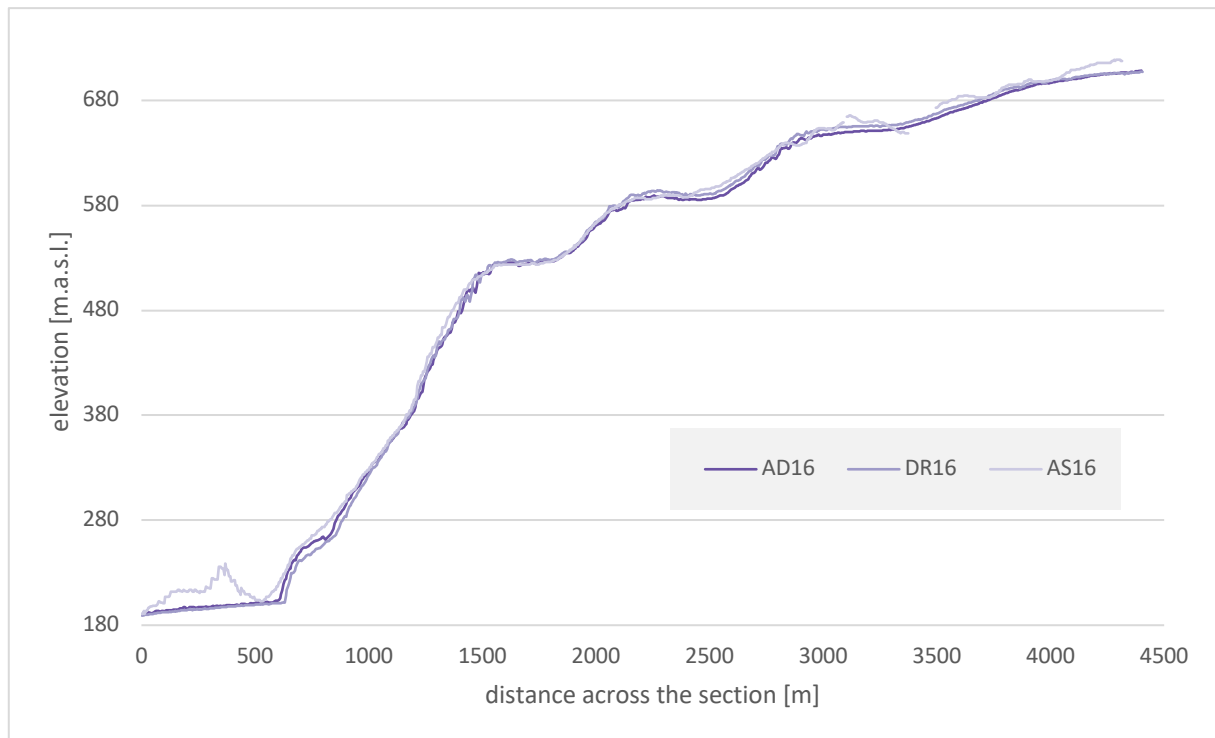
***Figure 50**: Comparison of the Sermeq Kujalleq cross-section (P3) of three DTMs of 2016 generated and acquired in different ways. They can be seen as exemplary DEMs of the three different quality groups and are colored accordingly.*

The different DEMs available for 2016 are once again plotted in Figure 50. In general, AS16 agrees well in steep terrain, but has high deviations in flat areas such as in the forefield (0-500m on the x-axis), as well as in the flat-ice areas in higher elevations (3000-4500m on the x-axis). The possible reasons and implications for this are discussed in chapter 7.2.2. In the terminus area we can see some disagreement between the three datasets which may be connected to the different acquisition dates. AD16 for example was acquired in March of 2016, while DR16 was acquired in August. The effect of the 2016 melt season is therefore visible in this section.
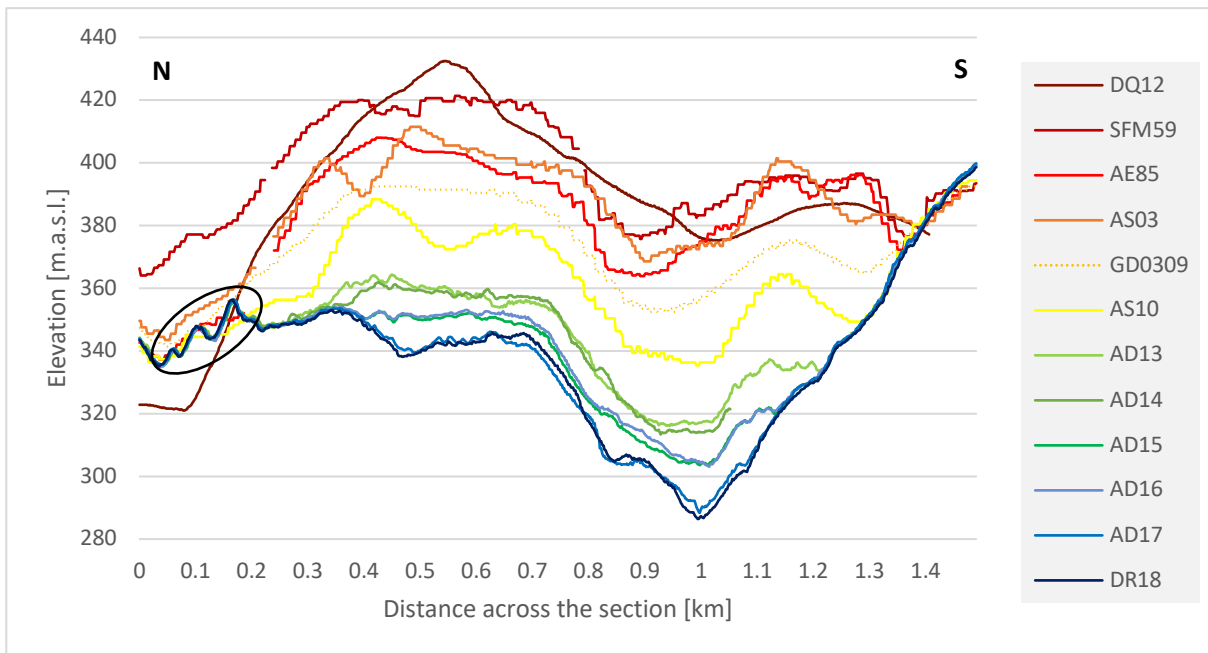
*Figure 51: Cross-section of Sermeq Kujalleq (P4) over time. The GimpDEM (GD0309) is marked with a dotted line, because this data is a result of a temporal composite. The location of the profile is marked in Figure 40. Note that the profile is curved in order to display both the northern and the southern margin in a near-perpendicular cross-section. Lateral moraine ridges are marked with a black circle.*

Looking at a cross-section of Sermeq Kujalleq (Figure 51), the general development is the same. There is a strong surface lowering over time, exposing more and more of the underlying bedrock on both the northern and the southern margin. While on the southern margin, the steep bedrock slope is clearly visible, things are a bit less clear for the northern margin. Early datasets (DQ12 and SFM59) do not agree well on the non-glaciated area (for DQ12 that is about the first 100m on the x-axis). However, the non-glaciated area is not considered stable terrain, because it is largely made up moraine material potentially deposited after 1912. In the highest resolution datasets (AD and DR), we can clearly see the cross-sections of several lateral moraine ridges caused by earlier glacier advances (between 100m and 200m on the x-axis, marked with a black circle in Figure 51).



*Figure 52: Foreland of the Sermeq Kujalleq Glacier. Note the steep bedrock on the orographic left of the glacier (south) as well as the thick moraine accumulation on the orographic right of the glacier (north). For location of the image refer to Figure 86 in Appendix C. Image by Simon Schudel (July 2018).*

### 6.4.4.    Point Time Series

In order to display the temporal development with a proper representation of the uncertainties associated with each of the datasets, time series for single points were generated. The four points A-D were selected along the length of the Nunap Kigdlinga profile in a manner that leveling points could also be included, such as data from 1948 in point C and data from 1971 in points A and D. The four profiles all display similarities as well as unique behavior. All points seem to experience a slight surface lowering between 1912 and 1959. In the case of Point C, this lowering amounts to about 15m. For points A and D, where data from 1971 is available, this surface lowering seems to continue until then. Between 1971 and 2003, most points experience a slight increase in elevation, some to similar elevations as in 1912 (e.g. point B and D). The one striking similarity, which is shared by all points, is the rapid decrease in elevation after 2003. It seems as if this surface lowering generally continues until 2018 with a short intermezzo in 2016, where a surface rise is registered in most points. In general, the surface lowering seems to slow down slightly between 2010 and 2018.
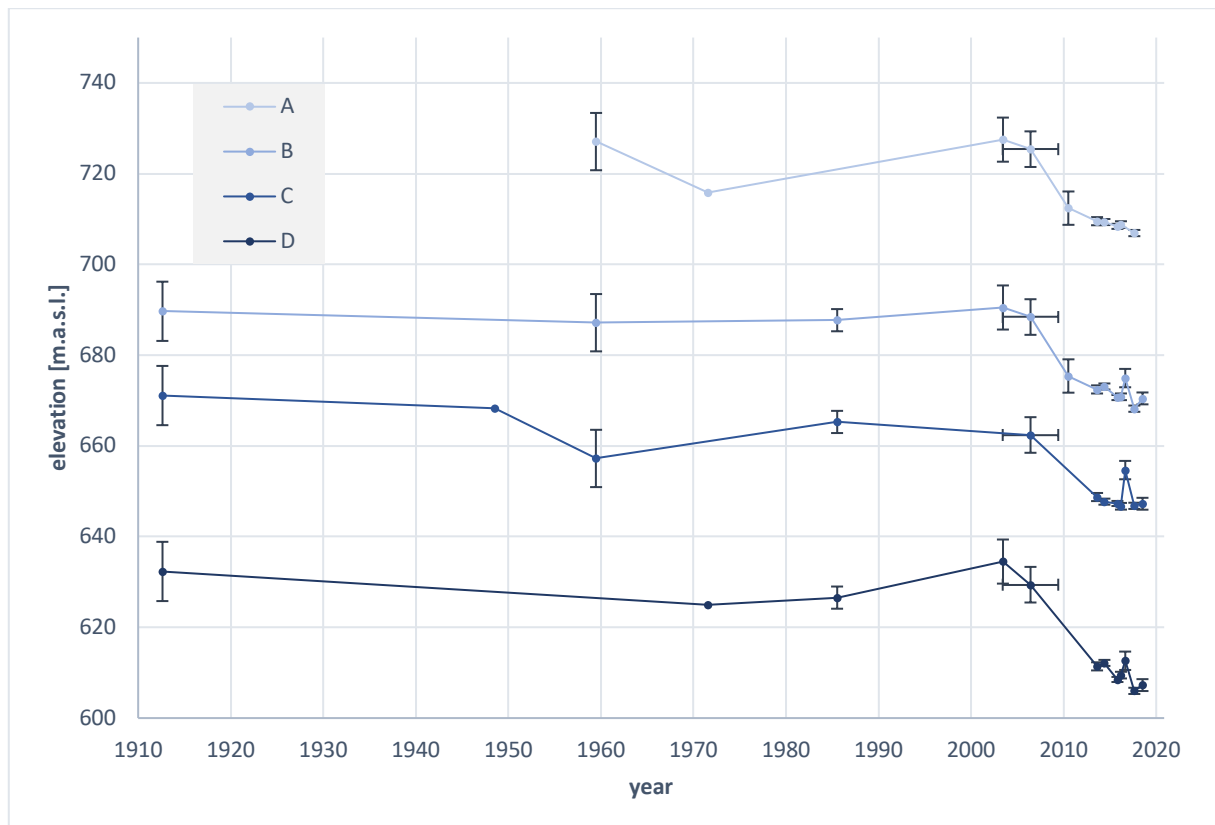


*Figure 53: Change in elevation over time for four selected points (A, B, C & D) on the Nunap Kigdlinga profile (see Figure 47 or Figure 46). Note that the record of 1971 in the time series of point A was translated onto the profile.*

As mentioned above, some datasets, such as the ASTER DTMs, seem to exhibit higher spatial variability than expected. In other words, the noise is higher and therefore the behavior of individual points may be very different. If we look at the mean of a larger amount of points (see Figure 54), this arbitrariness is reduced. For the mean calculation, the area mapped in 1912 by de Quervain & Mercanton (1920) was considered. Note that some datasets had void cells within this area.
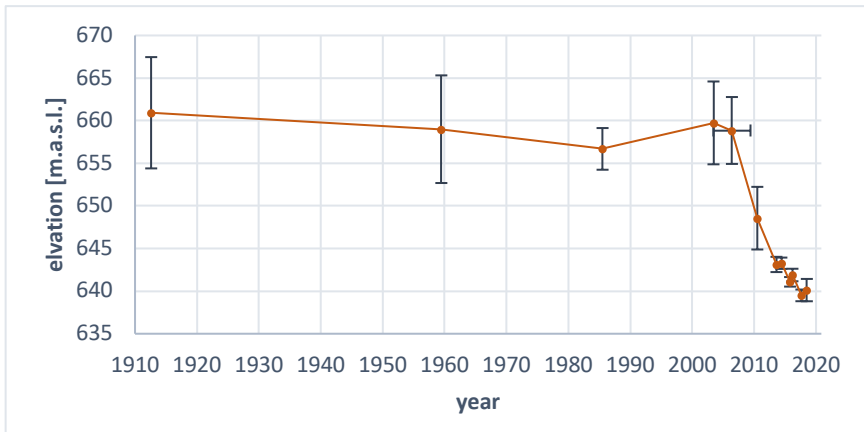
*Figure 54*: Mean change in elevation over time for the whole ice-covered area of Nunap Kigdlinga in the 1912 map (see the area de-lineated in blue in Figure 46). Note that the void cells of certain datasets within this area were not ac-counted for.

Point time series were also generated for Sermeq Kujalleq. The four points E-H were selected at various elevations along the flowline (P3), as shown in Figure 46. The time series for each of them is plotted in Figure 55. Their behavior over time is strikingly similar: A slight surface elevation increase between 1912 and 1959, then a decrease of about 15-20m until 1985. In general however, the surface elevation remains relatively constant between 1912 and 2003. Starting in 2003, a vast surface elevation decrease sets in, whereat the magnitude of that de-crease is clearly elevation dependent. The decrease is much stronger in lower altitudes, but the signal remains the same for elevations up to more than 700m.a.s.l., albeit in a weakened form.
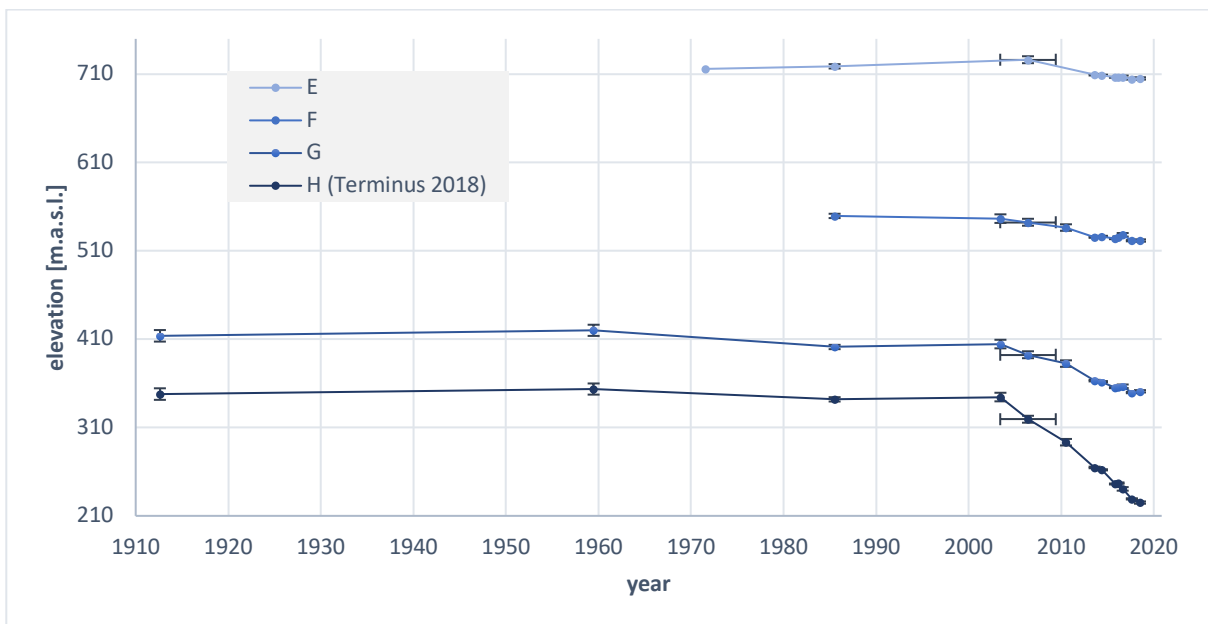


*Figure 55*: Change of elevation over time for four selected points of the Sermeq Kujalleq flow-line profile (see Figure 49 or Figure 46). H is the point that marks the terminus position in 2018. Note that the record of 1971 in the time series of point A was translated onto the profile.

Looking at Figure 49, the problem of unexpected spatial variability of the surface elevation records is not as big as for Nunap Kigdlinga (Figure 47), so the generation of a time series for the mean of an area is not called for.

## 6.5.   Surface Ice flow Velocity and Direction

The ice flow velocities derived from stable feature tracking (2013 – 2018, see chapter 5.10) and the available historic data (chapter 4.4) have been combined in a comparable way in Figure 56.
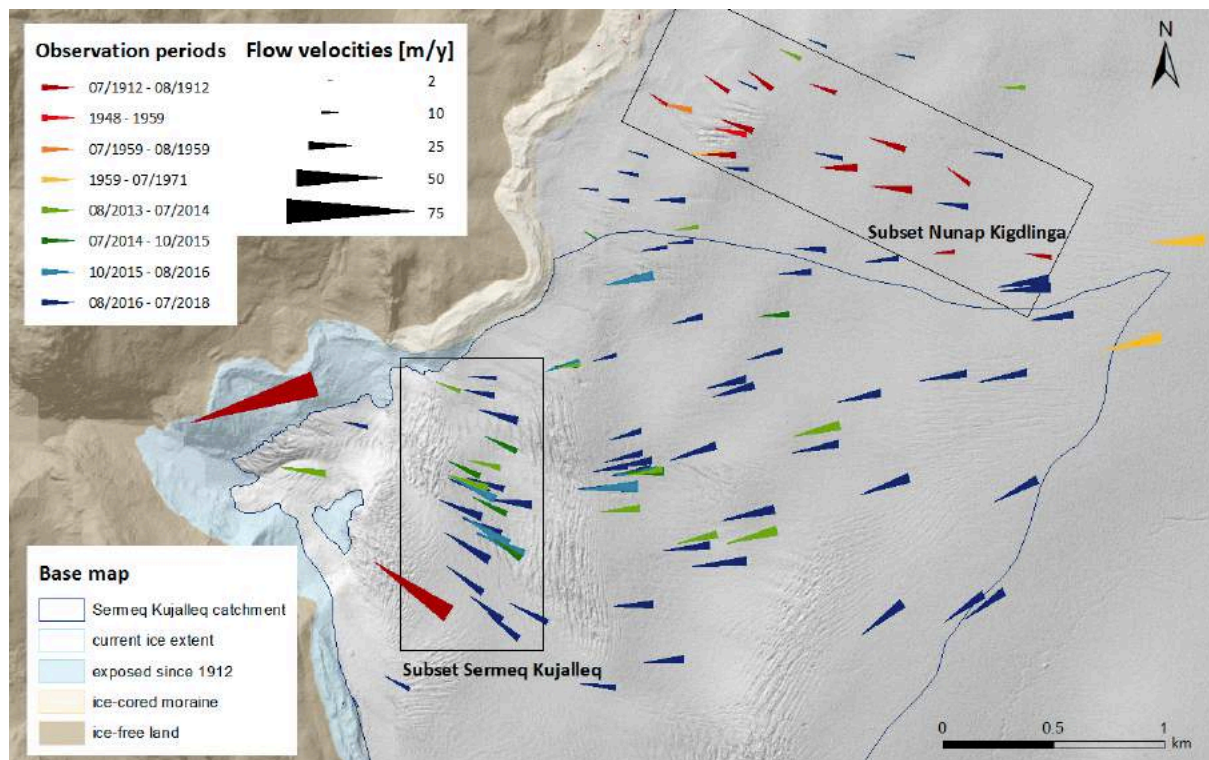


*Figure 56*: *Different velocity observations [m/y]. All velocity data between 2013 and 2018 results from stable feature detection and tracking in drone orthophotos as well as drone and ArcticDEM hill shades. Older data has been included from de Quervain & Mercanton* (1920)*, Bauer* (1968c) *and Zick* (1972). *Note the hard-to-see velocity information on the ice-cored moraine of Nunap Kigdlinga in the range of 2m/y. The marked catchment of Sermeq Kujalleq has been derived from recent ArcticDEM data and only reflects the present-day catchment based on surface inclination.*

Looking at the figure, the differences in data availability and distribution becomes apparent. Apart from detailed measurements by de Quervain & Mercanton (1920) in the Nunap Kigdlinga area, data is only sparsely available until the time between 2013 and 2018, when high resolution satellite and drone data allow for the derivation of flow velocities. While on first sight the flow velocities (arrow size) may look rather homogeneous, there are two strong exceptions: On the ice-cored moraine adjacent to the marked Nunap Kigdlinga subset, there are four measurements (two for 1912, two for the period between 1948 and 1959), which both indicate flow velocities in the magnitude of about 2m/y and are therefore barely visible on the map. The second big exception are the two measurement points of 1912 at Sermeq Kujalleq, where flow velocities of 51 and 73m/y were measured. Taking into account the different geometry of the glacier at the time, these values are hardly comparable to today's measurements. Note also that the highest velocity recorded in 1912 was located in an area which is today ice-free.
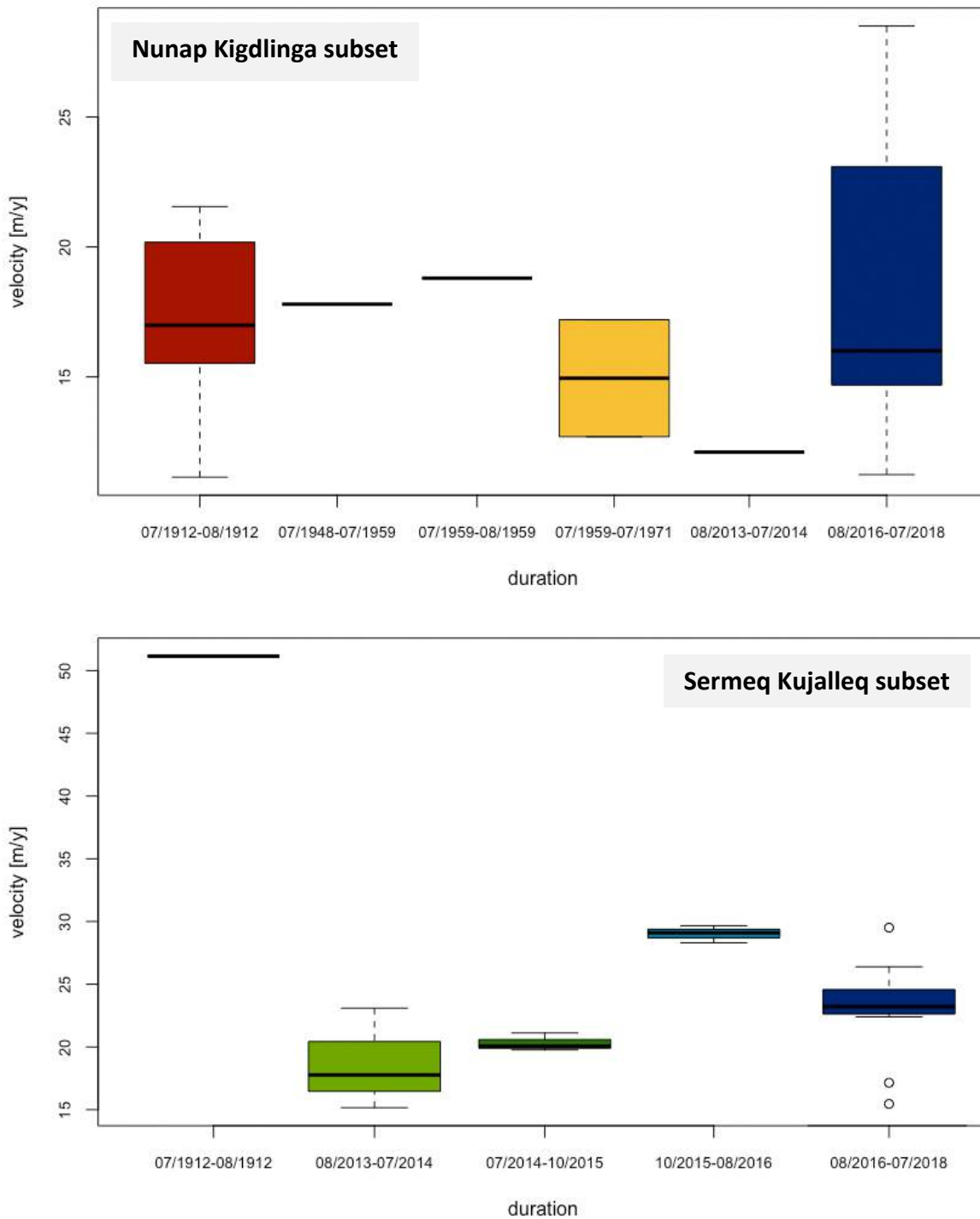
**Figure 57**: *Velocities of the Nunap Kigdlinga (top) and Sermeq Kujalleq (bottom) subset as marked in Figure 56. Note that some records only consist of one to three measurements. Also note that the time periods in the top plot are not the same ones as in the bottom plot. The colors are the same as in Figure 56.*

The two subsets marked in Figure 56 were plotted in boxplots in Figure 57. For Nunap Kigdlinga, the data availability for the different time periods differs a lot and the time period of 1912 and the period between 2016 and 2018 are the only ones with more than 5 measurements each. Nonetheless, there is no significant change over time and the velocities stay roughly in the range of 15 to 20m/y.

In the Sermeq Kujalleq subset, the velocities seem to be more dynamic. Apart from the much higher velocity measured in 1912, the velocities in the last five years were measured to be between 15 and 30m/y, with some considerable deviations between the years. Why this is the case is discussed in chapter 7.1.4.
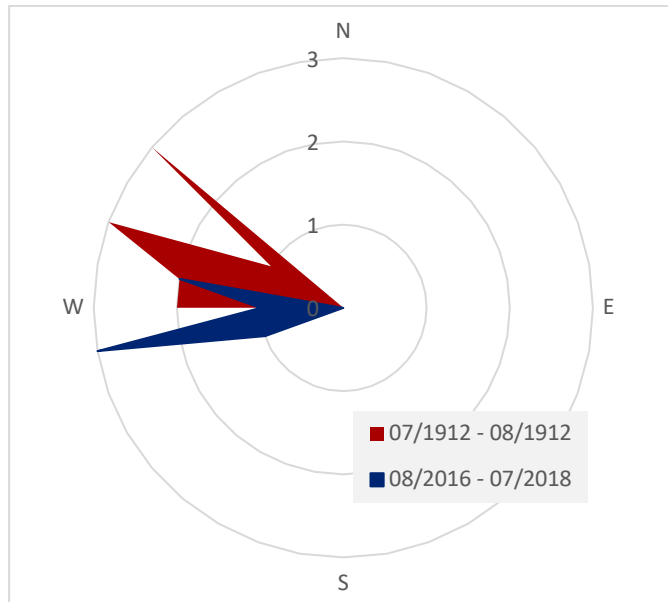


*Figure 58*: Ice flow direction in the Nunap Kigdlinga subset for 1912 and 2016-2018. The figure shows the amount of points with a certain flow direction, rounded to the next 10°.

In terms of direction, there do not seem to be any changes in the Sermeq Kujalleq subset (see Figure 56). However, this is not the case for the Nunap Kigdlinga subset. Considering only the measurement periods of 1912 and the one between 2016 and 2018, which each have five or more records, the shift over time is obvious (see Figure 58). The mean of the two periods are as follows: 289° for 1912 and 266° for 2016-2018. That is a shift of 23°, which is roughly equivalent to a shift from WNW to W.

## 6.6. Temperature Forcing

### 6.6.1. Results for RRT and RR

The two possibilities to determine RRT and the detrending line yield very different results for the three datasets. Figure 59 shows the detrending lines with the different RRT values calculated from the two methods described in chapter 5.11.3. Especially the RRT calculated with the ΔT⁺-approach for the Ilulissat temperatures yields a detrending line, which is clearly a bad fit for the cumulative temperatures (see the dashed orange line in Figure 59).
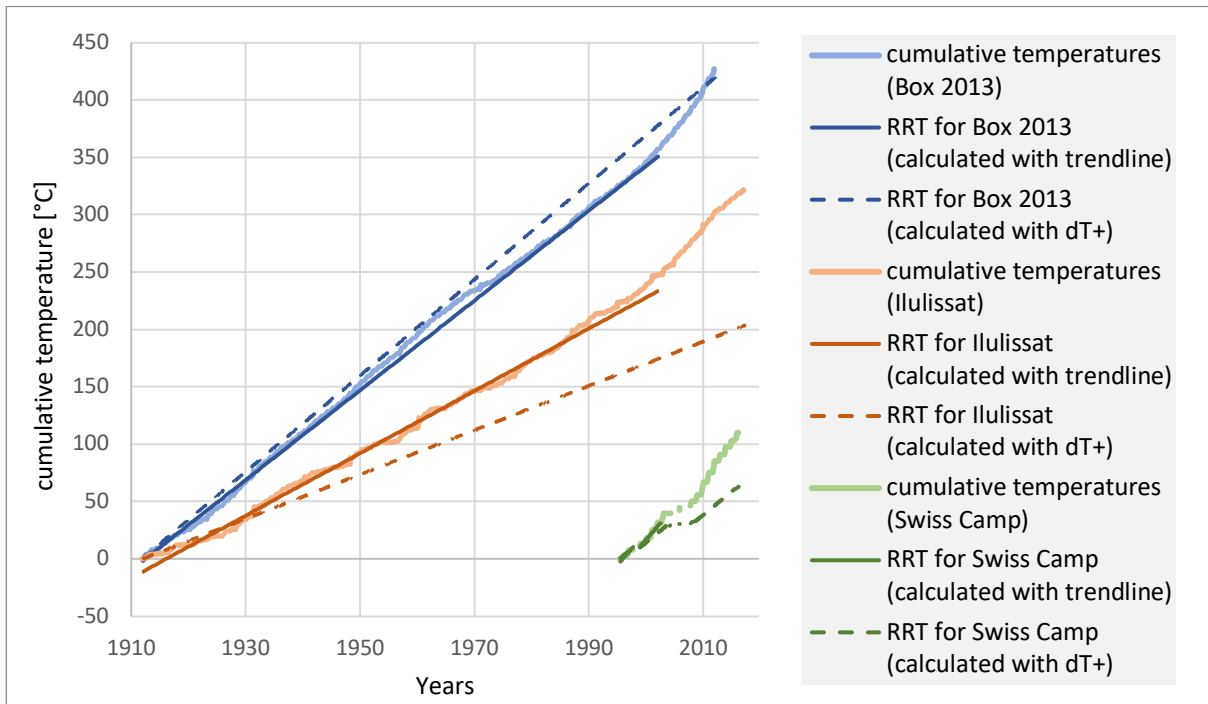


***Figure 59***: *The cumulative positive degree months for the three temperature datasets. Also marked are the different detrending lines calculated either with the trendline or $\Delta T^+$. Note that the RRT for the Swiss Camp is affected by missing data. Note that the trendlines for the trendline-approach were only calculated for the years before 2003.*

Table 17 shows the detailed functions for the detrending lines, including the derived *RRT* values. For both calibration techniques, the *PDMMF* as well as the *RR* in m/month were calculated according to Equation 12 and Equation 16. The $\Delta h$-value needed to calculate *PDMMF*, was taken for Point B (see Figure 46 for location), a point at Nunap Kigdlinga, which is not affected by any dynamic changes and seems to behave exemplarily for Nunap Kigdlinga (see Figure 53). In general, the results for the *RRT* calibration using the trendline seem to agree better in terms of *PDMMF* as well as *RR*. For the calibration of *RRT* with the $\Delta T^+$-approach however, the *PDMMF* and the *RR* values both differ up to one order of magnitude for the different temperature datasets.

*Table 17: Equations of the detrending lines as well as RRT and b values for both calibration approaches.*

|  |  | Ilulissat (DMI) | Swiss Camp (GC-Net) | Box (2013) |
|---|---|---|---|---|
| **Calibra-tion with trendline** | **Equation** | y = 0.23x − 11.74 | y = 0.47x − 2.69 | y = 0.32x − 2.44 |
|  | **RRT** [°C] | 0.23 | 0.47 | 0.32 |
|  | **b** | -11.74 | -2.69 | -2.44 |
|  | **PDMMF** [m/month/°C] | -0.45 | -0.67 | -0.45 |
|  | **RR** [m/month] | 0.10 | 0.13 | 0.14 |
| **Calibra-tion with** $\Delta T^+$ | **Equation** | y = 0.204x ± 0 | y = 0.325x ± 0 | y = 0.347x ± 0 |
|  | **RRT** | 0.204 | 0.325 | 0.347 |
|  | **b** | 0 | 0 | 0 |
|  | **PDMMF** [m/month/°C] | -0.34 | -0.43 | -2.09 |
|  | **RR** [m/month] | 0.07 | 0.14 | 0.73 |

### 6.6.2. Simulated Cumulative Surface Elevation Change

The above-mentioned tendency that the *RRT* values determined with the trendline-approach deliver more consistent results, is also supported by Figure 60, where the detrended cumulative surface elevation change of the three analyzed datasets are plotted. In the figure on the top, which displays the results for the trendline-approach, the results are in better agreement compared to the figure on the bottom ($\Delta T^+$-approach).
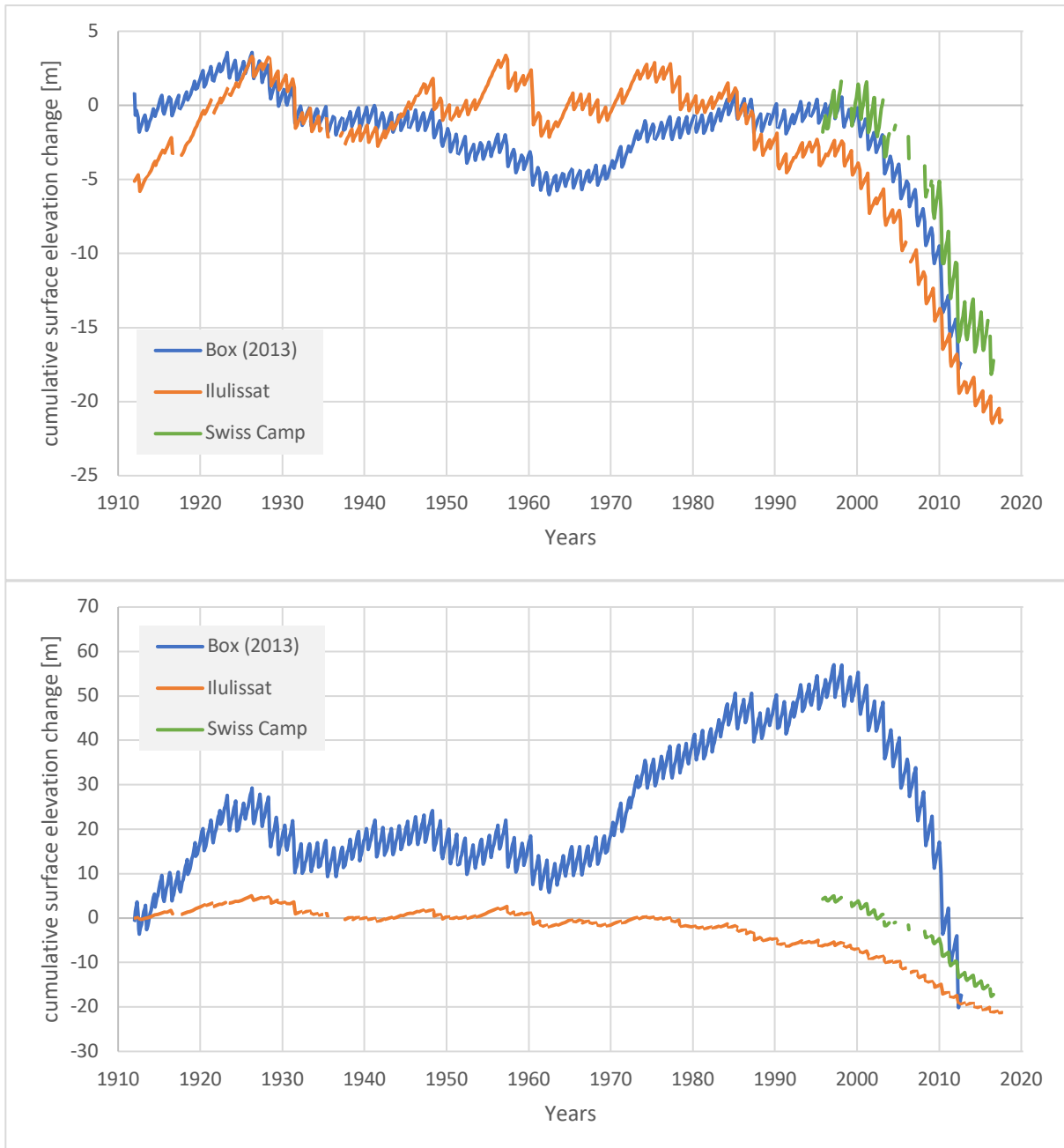
***Figure 60***: *Simulated cumulative surface elevation change with the three temperature datasets and for the two approaches to calculate RRT (top: trendline-approach, bottom: ΔT⁺-approach).*

Thus, it is clear that the selection of the *RRT* and therefore the detrending technique is crucial for the results. To visualize the effect of different *RRT* values, the different detrended cumulative temperatures of Box (2013) displayed in Figure 37 were used to reconstruct cumulative surface elevation change between 1912 and 2013. Note that these *RRT* values are arbitrary and only serve to visualize the effect they have.
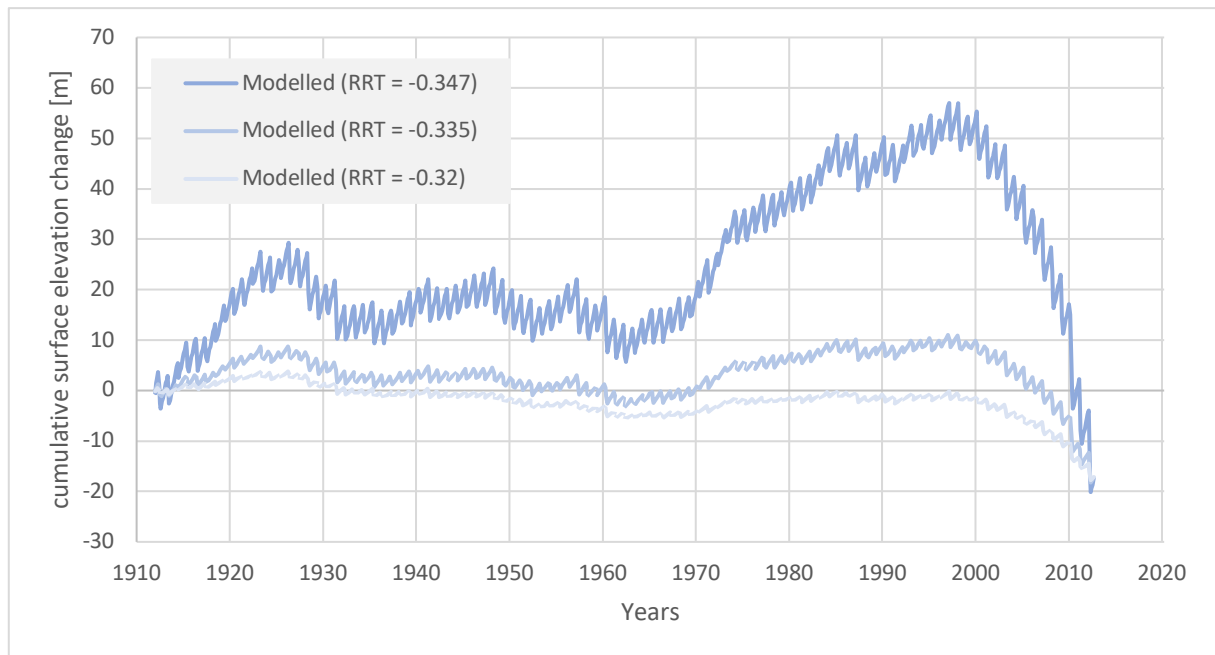
**Figure 61**: *Impact of different exemplary RRT values (see also Figure 37) on the reconstruction of surface elevation change from the same temperature data* (Box 2013)*.*

### 6.6.3.    Melt Rate Reconstruction

As further analysis and comparison will show (see chapter 7.1.5), the temperature data from Box (2013) with the  trendline-approach to determine *RRT* turns out to be the best estimation for the recharge rate. The melt rate is therefore only reconstructed using this estimation: RR = 0.14m/month. That is a value of 1.68m/y. In other words, 1.68m of ablation are compensated by the steady ice recharge per year. To get melt / ablation results, this value thus has to be subtracted from the surface elevation change rate per year (see Equation 17). The resulting melt rates including uncertainties were plotted in *R* and are presented in Figure 62 for point B (Nunap Kigdlinga) and for point H (Sermeq Kujalleq).
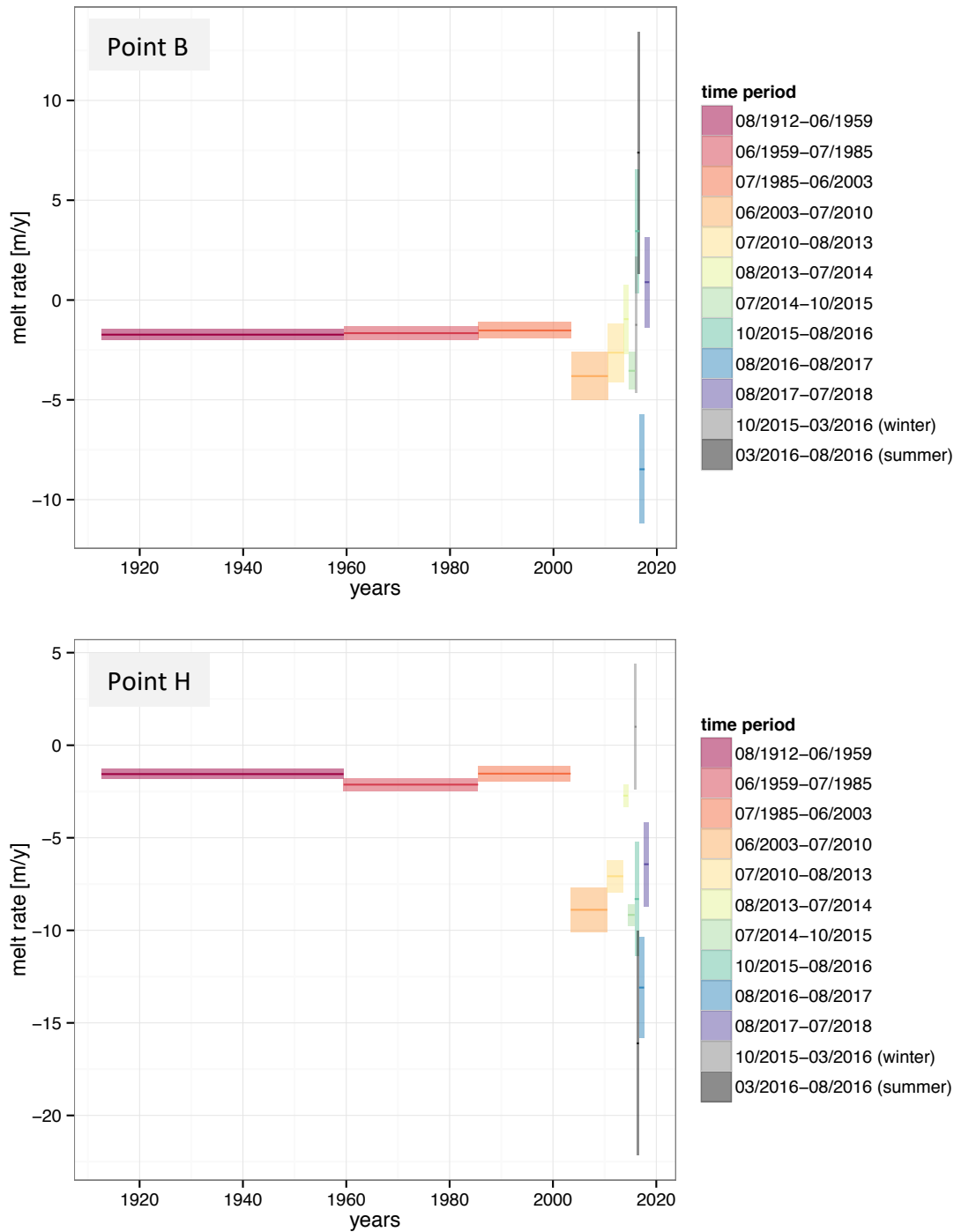
*Figure 62: Melt rates of point B (Nunap Kigdlinga, top) and point H (2018 terminus position of Sermeq Kujalleq, bottom) for different time periods. The two time periods marked with 'winter' and 'summer' offer a hint at the seasonal variability.*

Note that the uncertainty of the elevation change per duration is not only dependent of the uncertainty associated with the input datasets, but also of the duration between the acquisition of the earlier and later dataset (see also Equation 17). That is the reason why the uncertainty is generally higher for the more recent, shorter duration measurements. Another thing to realize is that the *RR* was only optimized for point B, where little dynamic influences are to be expected (see chapter 6.6.1). But those same values were used to calculate the melt rates of point H.

Using the yearly melt rates, it is also possible to estimate the total melt for the observed time period (1912-2018). To do so, Equation 17 is solved for the whole time period between 1912 and 2018 using the surface elevation data of point B, in order to get the mean melt rate.

$$mr_{1912-2018} = \left[(670.46 \pm 1.31m) - (689.66 \pm 6.53m) \cdot \frac{365d}{17117d}\right] - (12 \cdot 0.14m)$$

$$= [(-19.2 \pm 7.84m) \cdot 0.021] - 1.68m$$

$$= (-0.40 \pm 0.16)m \cdot y^{-1} - 1.68m$$

$$= \underline{-2.08 \pm 0.16\ m \cdot y^{-1}}$$

The total melt between 1912–2018 for point B can then be estimated, by projecting this rate onto the whole time period of 106 years:

$$M_{1912-2018} = 106 \cdot (-2.08 \pm 0.16\ m \cdot y^{-1})$$

$$= \underline{220.8 \pm 17.0\ m}$$

# 7. Discussion

## 7.1. Interpretation and Comparison with Other Research

### 7.1.1. Comparison with Eqip Sermia

Some of the analyzed DEMs extend all the way to Eqip Sermia, enabling a direct comparison between the surface elevation changes at the land-terminating ice-margin and the outlet glacier. In Figure 63, three DEMs are compared to the 2017 ArcticDEM, which is the newest large-scale dataset available.
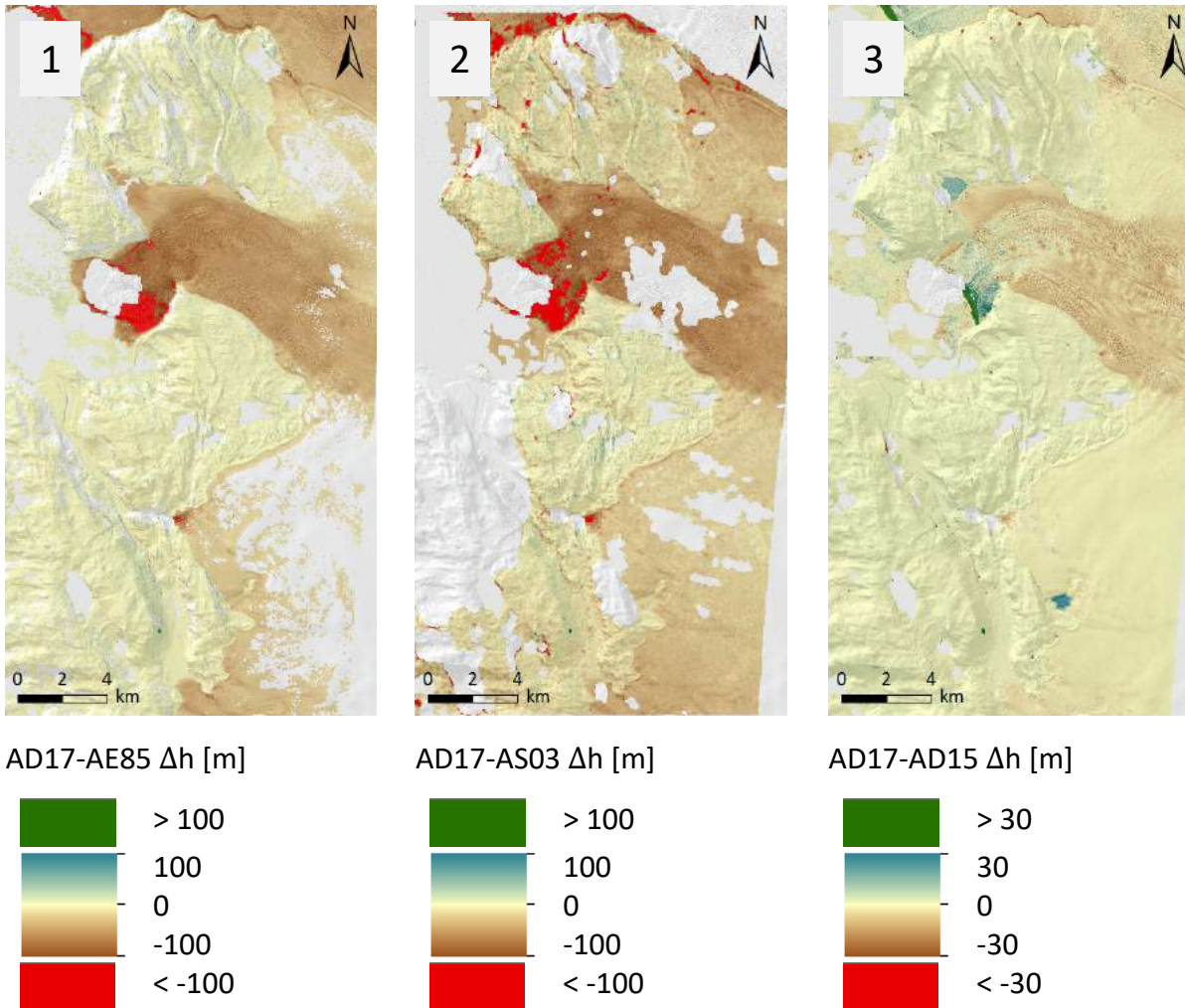


**Figure 63**: *Surface elevation change for Eqip Sermia and adjacent areas including Nunap Kigdlinga and Sermeq Kujalleq. (1) 1985-2017. (2) 2003-2017. (3) 2015-2017. Note that AD17, AD15 and AE85 were not co-registered, because they have very little offset compared to ADcomp. AS03 was co-registered according to the parameters determined for the small subset of the AOI (see Table 14). The hill shade in the background has been generated from ADcomp.*

The DTMs were selected to represent long-term changes from 1985 to 2017 (1), medium-term changes from 2003 to 2017 (2) as well as short-term changes from 2015 to 2017 (3). It is clear that the thinning is always much more widespread and in higher magnitude at Eqip Sermia compared to the ice sheet margin. Only the tip of Sermeq Kujalleq reaches a surface lowering which is comparable to Eqip Sermia. What is also apparent from Figure 63 is the fact that the thinning of Eqip Sermia reaches far back behind the terminus: Even about 15km away from

the terminus of Eqip Sermia, the surface elevation change is higher than at the Nunap Kigdlinga. Note that in the short-term comparison (3), some areas at the Eqip Sermia terminus have undergone an advance and thickening. Other elevation increases on said map are caused by effects of water bodies.



AS03-AE85 Δh [m]

| | |
|---|---|
| | > 100 |
| | 100 |
| | 0 |
| | -100 |
| | < -100 |

AD17-AS03 Δh [m]

| | |
|---|---|
| | > 100 |
| | 100 |
| | 0 |
| | -100 |
| | < -100 |
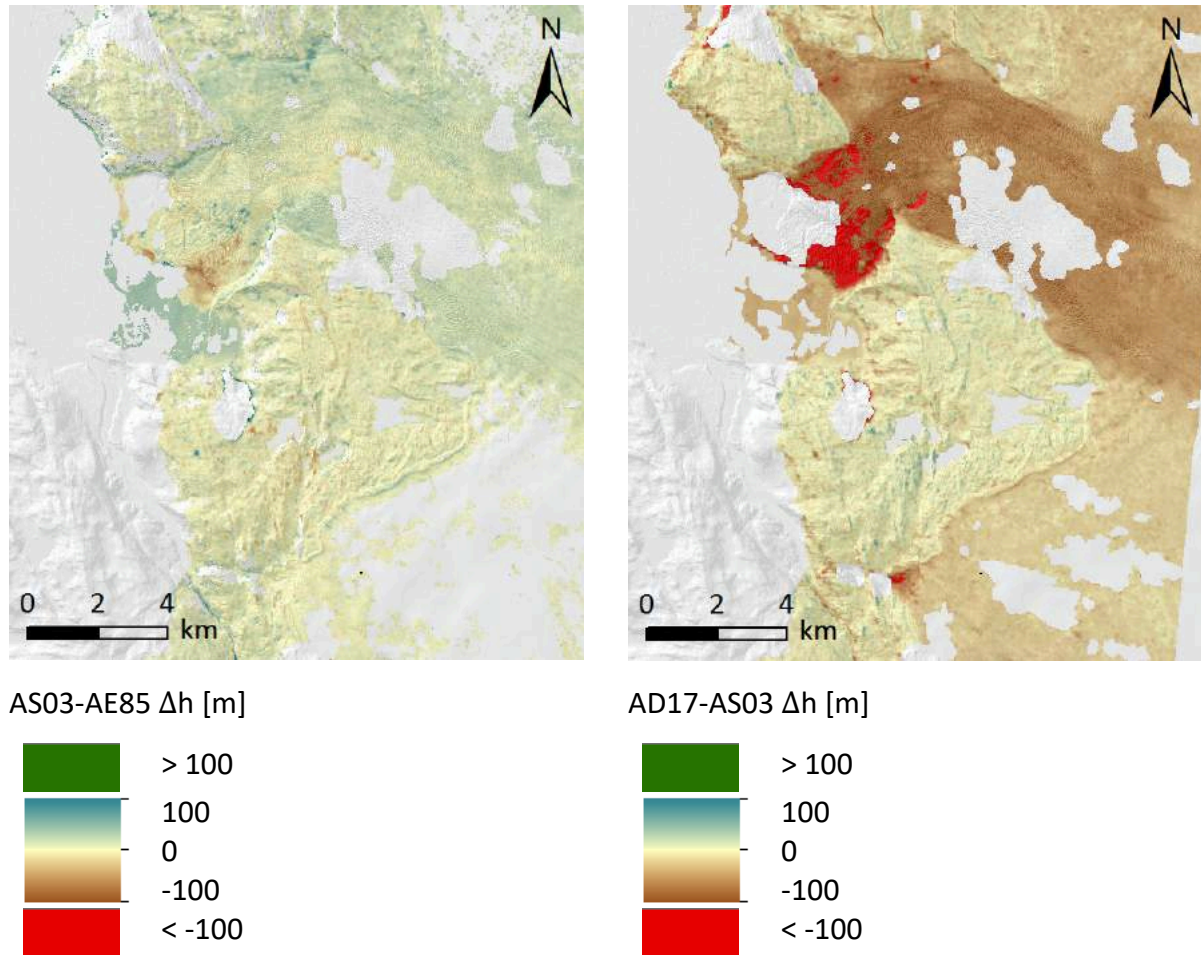
*Figure 64: Surface elevation change for Eqip Sermia and adjacent areas including Nunap Kigdlinga and Sermeq Kujalleq for 1985 – 2003 (left) and 2003 – 2017 (right). Note that AD17 and AE85 were not co-registered, because they both have very little offset compared to ADcomp. AS03 was co-registered according to the parameters determined for the small subset of the AOI (see Table 14). The hill shade in the background has been generated from ADcomp.*

Another interesting comparison is presented in Figure 64. On the left the development between 1985 and 2003 is presented, on the right the development between 2003 and 2017. The difference is striking: While there was no clear trend for the first time period, there is a very strong surface elevation loss in the second time period for all ice-covered areas. This supports the finding that around 2003 there was a turning-point for both Eqip Sermia as well as Nunap Kigdlinga and Sermeq Kujalleq.
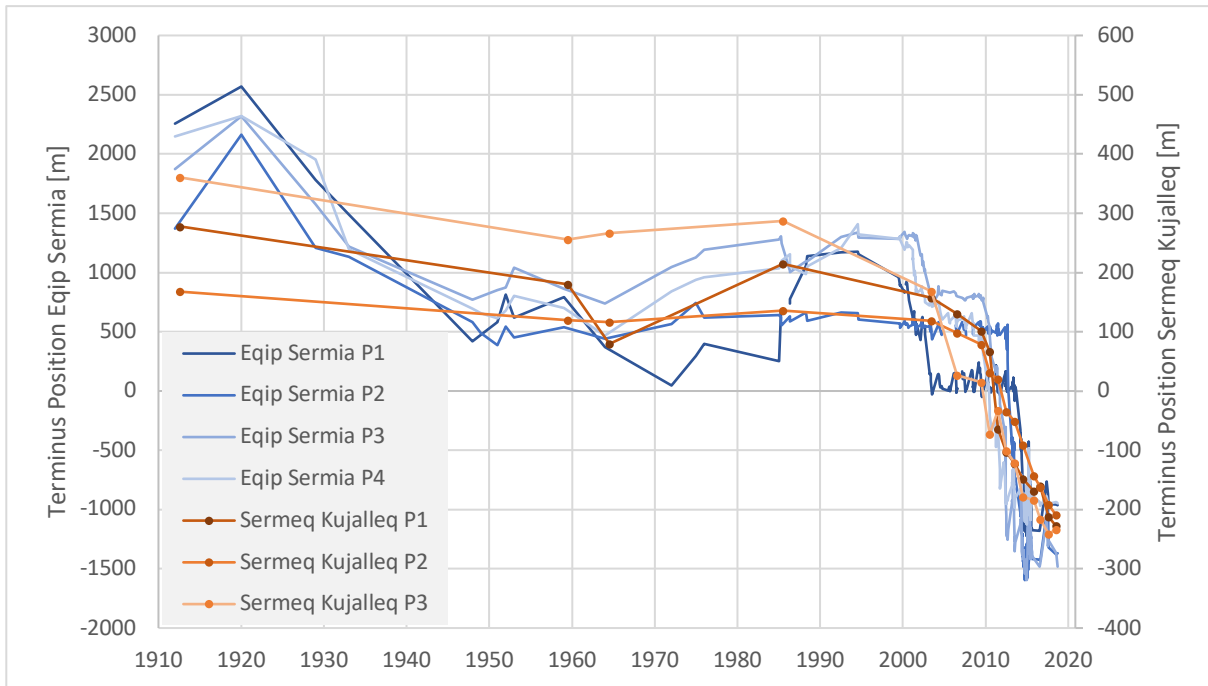
***Figure 65****: Comparison of the terminus positions of both Eqip Sermia and Sermeq Kujalleq. The positions of the terminus can differ across the whole glacier, which is why there are several profiles for each of the glaciers (marked in Figure 8 and Figure 40). The data for Eqip Sermia was adapted from Lüthi et al. (2016) and comple-mented with more recent retreat lines derived from Sentinel-2 imagery. Note that the scale for Sermeq Kujalleq is five times smaller than for Eqip Sermia. 0 was defined as the mean value of each of the profiles.*

Lüthi et al. (2016) describe the horizontal retreat of Eqip Sermia along four profiles (P1 - P4 in Figure 8). This data is compared to the retreat of Sermeq Kujalleq along three profiles (P1 – P3 in Figure 40) in Figure 65. The general trend is strikingly similar for both glaciers, albeit the magnitude of the change is much smaller for Sermeq Kujalleq (the scale in the figure is five times larger than for Eqip Sermia). The advance between 1912 and 1920 measured for Eqip Sermia, was not recorded for Sermeq Kujalleq, because no data is available of that time. But an advance of Sermeq Kujalleq is certainly possible or even likely, considering the advancing state of the glacier terminus in 1912 (see the qualitative assessment in Table 12), which was also described to override vegetation of considerable age (de Quervain & Mercanton 1920; Rabot & Mercanton 1913). There is a clear retreat for both glaciers until about 1960, when a slight advance sets in, which is also recorded for both glaciers. The drastic retreat, which is unprecedented for the whole century, starts about 2002 or 2003 and is again recorded for both glaciers. Due to the fact that Eqip Sermia is a tide-water glacier, the retreat progresses in a stepwise motion (Lüthi et al. 2016), which is not the case for Sermeq Kujalleq. The two areas thus do not only have a similar trend in terms of surface elevation change (see Figure 64), but also in terms of horizontal retreat. Here too the changes are larger in magnitude for Eqip Sermia than for the slow-flowing and land-terminating ice margin, but the general signal is very similar.

Lüthi et al. (2016) conclude that both oceanic and atmospheric temperature forcing, which are of course partly linked to each other, behave very similarly to the variations of the Eqip Sermia terminus position. If the development was mostly linked to oceanic forcing, it would entail that the changes would rather be moving from the calving front upwards, while

atmospheric temperatures as the main driver would suggest a development moving down-wards. However, Lüthi et al. (2016) do not highlight one of the two as the driving factor. The result of this thesis is not directly affected by changing oceanic temperatures, since Sermeq Kujalleq and Nunap Kigdlinga are not marine-terminating, but still yields a similar develop-ment, suggesting that a development like the one of Eqip Sermia may be largely explained by atmospheric temperatures, whereas the oceanic influence may have enhanced the signal for Eqip Sermia.

### 7.1.2. Comparison with Other Land-Terminating Margins

The three Sermeq Kujalleq profiles in Figure 65 have a mean annual retreat rate of about 14 ± 1 m/y between 1985 and 2017. Those numbers are in the same order of magnitude as the results of Mernild et al. (2012), who based their research in southeastern Greenland. They compared the recent retreat between 1972 and 2012 of both land- and marine-terminating ice margins. The land-terminating margin recession is measured at 18 ± 9m/y for GrIS margins and at 10 ± 6m/y for other local land terminating glaciers and ice caps.

The above mentioned ratio of roughly five to one between the retreat of a marine-terminating glacier and the retreat of a land-terminating ice margin in a comparable area, was also de-scribed by Mernild et al. (2012). The marine-terminating outlet glaciers displayed a retreat about three to five times larger than nearby land-terminating, which is about the same rela-tion as between Sermeq Kujalleq and Eqip Sermia (see Figure 65). The same ratio was also described by Levy et al. (2016) for the whole Holocene, however, again for southeast Green-land. Of course, the results from southeast Greenland cannot be directly compared to the results of this thesis, which treated data from the west coast. Especially the oceanic influence may be very different for the two coasts, as the marine-terminating glaciers there are heavily influenced by the East Greenland Coastal Current and the East Greenland Current (Murray et al. 2010). However, it is striking that all these studies yield a retreat rate result for land-based margins which is roughly five times smaller than comparable marine-based glaciers.

The results by Bjørk et al. (2012), which suggest that land-based glaciers are not as affected by the current warm temperatures as the marine-terminating glaciers (see Figure 12), can also only be compared to this thesis with reservation, because the land-terminating glaciers de-scribed in their study are mostly valley glaciers which have retreated higher up over time and are therefore in very different climatic surroundings as e.g. in the 1930s. This is not the case for Sermeq Kujalleq, whose terminus has remained more or less on the same elevation (for now). That is probably also the reason why it has undergone a very similar retreat sequence to the one of Eqip Sermia. Nonetheless, the result of this thesis is opposing the results of Bjørk et al. (2012), as well as the results of Sole et al. (2008), who stated that land-terminating glac-iers were not affected by the drastic changes after the year 2000, which were recorded for most marine-terminating glaciers. Why this is the case needs further investigation, but one possible explanation is the spatial resolution. The changes at Nunap Kigdlinga are not much larger than the uncertainties associated with early DEMs. Thus, a high-resolution analysis like it was done in this thesis, may be necessary to make out such small trends.

### 7.1.3.   Moraine and Debris at Nunap Kigdlinga

When talking about the ice extent at Nunap Kigdlinga, a big unanswered question remains. As mentioned in chapter 2.1.1, the ice is heavily debris-covered and a distinction between an ice-cored moraine or debris-covered ice seems difficult. It is also not entirely clear how this influences the melt and retreat of the margin. However, Bauer (1968c) might give a clue. He described in detail the development of the moraine crest between 1912 and 1959. He records a slight advance of the ice margin / the ice-cored moraine, but at the same time a loss of thickness.

> *"C'est là un exemple type d'un glacier dont le front avance (par suite des conditions particulières dues au glacier parasite qui protège la fonte de son front) et qui, pourtant est en décrue."* (Bauer 1968c: 68)

Thus, he argues that this is typical behavior for a glacier whose front is protected by a parasite glacier (the snow in front of the moraine) from melting. This protection allows an advance, even though there is actually a mass loss. The thickness loss is described by elevation measurements of the highest point of the crest over time. In 1912, the crest of the moraine is described to tower 60m above the forefield (de Quervain & Mercanton 1920). Between 1912 and 1959, the loss amounts to 12.6m (Bauer 1968c). Note that these measurements are not directly comparable to the results in this thesis (e.g. Figure 47 or Figure 53), because they concern the elevation of a moving feature. The same is not true for the results of this thesis, which are always connected to one position. However, today the crest is located at about 40m above the foreland (see Figure 47).

Bauer (1968c) also describes a loss in flow velocity at the very border (on the moraine). In 1912, de Quervain & Mercanton (1920) had measured a velocity of about 2.5m/y, whereas between 1948 and 1959 a movement of only 1.5m/y was observed. According to Bauer (1968c) this is also the effect of the described thinning. However, it may also play a role, that the measurements of de Quervain & Mercanton (1920) were only measured over a few days in summer, while the later measurement was recorded over several years including winters, where ice flow velocity may decrease.

Looking at the long-term data that is available today (see Figure 47), the advance and the surface lowering described by Bauer (1968c) can be observed in the data. The ice margin in 1959, 1985 and even in the GimpDEM of 2003-2009 has moved further on ice-free land than in 1912. However, the ice surface remained at a stable elevation or even slightly increased between 1959 and 2003, before a fast surface lowering of the ice margin set in again. The 'parasite glacier' as well as the thick debris cover at the immediate ice border certainly have an influence on the behavior of the margin and may indeed keep it from retreating any faster. Recent years of comparably strong surface lowering suggest that most of the mass is lost in a 'vertical retreat' (down-wasting), rather than a horizontal one. Movement of the moraine debris, which could lead ice cliffs to be exposed to melt, may also play an increasing role.

### 7.1.4. Surface Ice Flow Velocity and Direction

The ice flow velocity results of this thesis are limited, due to the small number of records. As shown in Figure 56 and Figure 57, the velocities at Sermeq Kujalleq are much higher in 1912 than in recent records. Why this is the case is hard to say, but it is in the nature of a steep glacier lobe like Sermeq Kujalleq, that the velocities are much more dynamic: Fast changes in the surface elevation have an influence on the surface slope as well as ice thickness and therefore the velocity. The surface lowering at the terminus leads to an increase in surface slope, which in theory should yield faster velocities (Benn & Evans 2010). However, the ice thickness, which is the second important factor influencing flow velocity, has decreased considerably and seems to dominate the effect. In other words: Due to the mass loss at the terminus, the mass flux in the Sermeq Kujalleq subset (see Figure 56 and Figure 57) was reduced, which went hand-in-hand with a decrease in velocity. It also has to be stated that Sermeq Kujalleq is very heterogeneous and said subset is located on a plateau above a steep ice fall. Unlike in the analyzed subset, the increase in surface slope can be expected to be more dominant in such a steep zone, which in turn may lead to an increased flow speed in these areas.

For Nunap Kigdlinga the surface flow velocities are observed to be relatively stable at 15-20m/y. These results comply with other recent measurements of ice flow velocity in the same area – namely the available updated *MEaSUREs Greenland Ice Sheet Velocity* data from Joughin et al. (2015). This velocity dataset, which is now also available for more current time periods up to 2018, is created from RADARSAT synthetic aperture radar data. For the data between 2000 and 2013, the data is provided in a 500m gridded raster. The newer data is available in 200m gridded cells. Figure 66 offers a comparison for Nunap Kigdlinga and Sermeq Kujalleq between the velocity data by Joughin et al. (2015) as well as the mean of the data collected in this thesis for each of the two subsets (essentially the same data as in Figure 57).
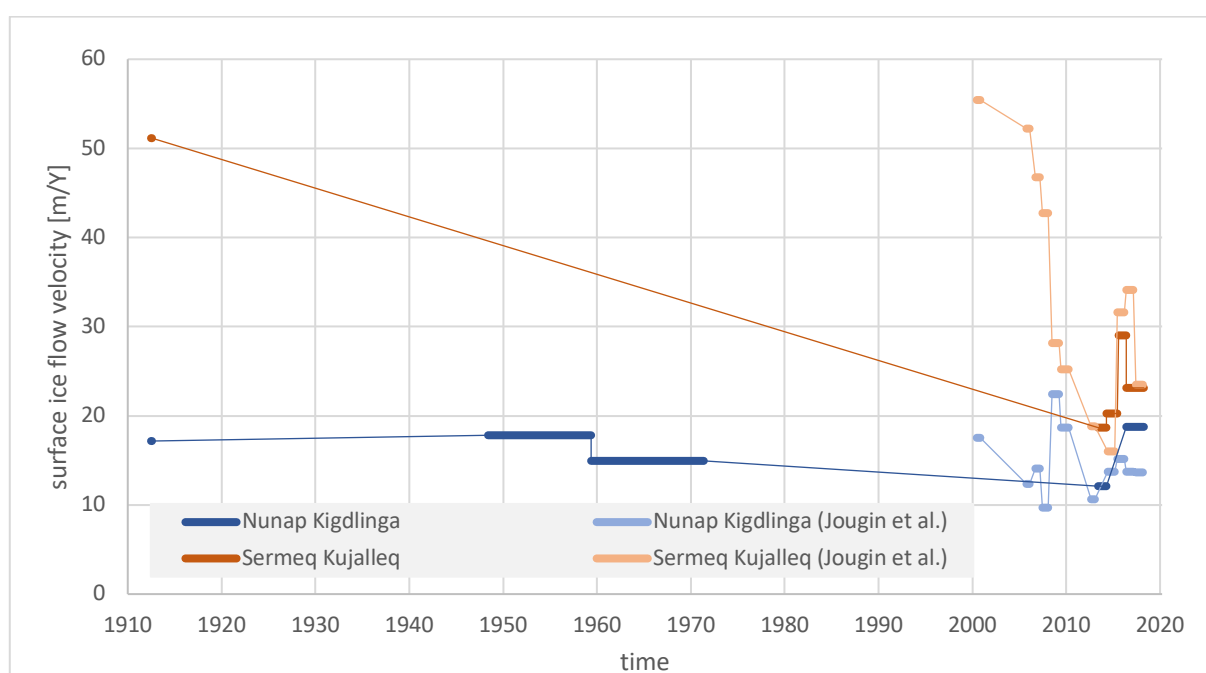


***Figure 66***: *Mean surface ice flow velocity for the Nunap Kigdlinga subset and the Sermeq Kujalleq subset (see Figure 56 for location). They are compared to velocity values of the same area by Joughin et al. (2015).*

Where there is data from both sources, there is generally a good agreement – the highest offset between the two being the year 2017/18 at Nunap Kigdlinga with a difference of about 5m/y. Short term variations, such as a velocity increase 2015/16 at Sermeq Kujalleq are recorded by both sources. Very interesting is the data by Joughin et al. (2015) of Sermeq Kujalleq between 2000 and 2015. The velocities in 2000 are recorded at about 55m/y, which is almost the same as was measured in 1912. The following decade then brings along a massive slowdown to a level of about 25m/y which is almost the same as for Nunap Kigdlinga. Thus, this decrease in velocity is exactly synchronous with the retreat (see Figure 65) and the decrease in surface elevation (see Figure 55) observed at Sermeq Kujalleq.

The observed change in ice flow direction at Nunap Kigdlinga (see Figure 58)  makes sense in light of the profound surface lowering at Sermeq Kujalleq, which must have increased the surface slope towards Nunap Kigdlinga, leading the ice flow, which is largely dependent on the surface slope, to shift in that direction.

### 7.1.5.  Temperature Forcing

The reconstruction of surface elevation changes using temperature data was only possible with the four simplifying assumptions presented in chapter 5.11.1. However, many of the ignored parameters are indeed negligible. Dynamic ice flow is dependent of changing ice surface slopes and aspects (Benn & Evans 2010). At Sermeq Kujalleq glacier, profound changes were indeed observed, and this assumption is therefore certainly not applicable to this area. However, at the rather inactive Nunap Kigdlinga ice margin such dynamics are, if present, very slow and long-term. Sole et al. (2008) state that the *"thinning of land-terminating outlet glaciers … seems to be a response to changes in local mass balance (principally increases in air temperature) (…)".* Since the temperature forcing is only compared to Nunap Kigdlinga (see Figure 67), which does not contain a large range of elevation, the second assumption (same temperature for whole AOI) is plausible. The third assumption entails disregarding the precipitation. Precipitation is of course not actually zero in the area, but it is actually very small. An AWS from GIUZ at Eqi Camp for example registered only 240mm of precipitation from September 2017 to July 2018. Also, most of the precipitation will probably fall as snow, which will just melt away again in spring, without much impact on the ice underneath. A certain insulation effect of the snow cover is likely, but with long-term data, it can be expected that this effect will be accounted for in the melt factor relating the temperature and the melt. Thus, the ice supply coming from the ice sheet is in fact the single most important source of elevation rise. The recharge rate is assumed to be constant in this thesis, but since it is directly dependent of the flow velocity, we know this is not true. The flow velocity of the GrIS is not independent from seasonality, but undergoes surface-melt induced speed-ups of up to 25% (Zwally et al. 2002). Lemos et al. (2018) even recorded a speed-up of 32% for Russell glacier close to Kangerlussuaq, which is also a land-terminating ice lobe similar to Sermeq Kujalleq. Thus, it has to be stated that assuming the recharge rate to be stable is a mere approximation and only valid on a decadal scale. However, Nunap Kigdlinga is not a typical glacier with converging ice, and a more stable flow regime can be expected (see also Figure 57).

As Figure 60 has shown, the calibration of the *RRT* using the trendline-approach yielded the most consistent results for the different temperature datasets. In Figure 67 this cumulative surface elevation change simulated with temperature data is plotted together with the actually measured surface elevation change at point B.
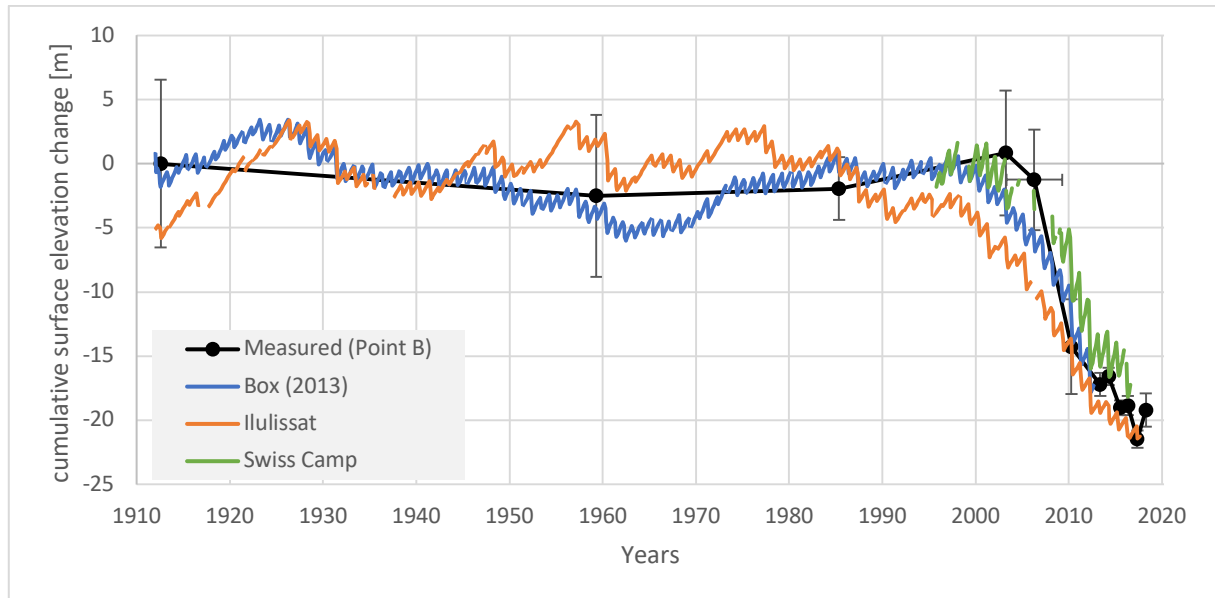


*Figure 67*: Comparison of the measured surface elevation change (black) as well as the simulated surface elevation changes using the three temperature datasets of Box (2013, blue), Ilulissat (orange) and Swiss Camp (green) for point B (see Figure 46 for location). All RRTs were calibrated using the trendline-approach.

The figure shows that all three simulated surface elevation changes roughly agree with the measured surface elevation change. Especially the temperature data by Box (2013) displays a very high level of agreement. The surface elevation change simulated with Ilulissat data (orange) generally displays a higher variability in time but is mostly within the error bars of the measured surface elevation change. The only difference seems to be the start of the warming and surface elevation lowering. In the Ilulissat data, this turning point is already about 1999. Nonetheless, the general warming and surface elevation lowering since the early 2000s are also depicted in this reconstruction, albeit with a certain offset. The reconstruction with the Swiss Camp dataset also yields good results with just small offsets. In order to statistically describe this correlation, the Pearson correlation coefficient *R* is utilized (e.g. Walter 2016). It describes the linear dependence between the measured cumulative surface elevation change and the different simulated cumulative surface elevation changes depicted in Figure 67. It is calculated by solving Equation 18 (see Appendix D). The value for *R* is between 0 and 1, where a higher value indicates a higher correlation. The R-values for the three temperature datasets result in 0.944 for the dataset of Box (2013) 0.935 for the Ilulissat dataset, and 0.947 for the Swiss Camp dataset. This, as well as the visual comparison in Figure 67 shows that the observed cumulative surface elevation change at point B can be recreated using a calibrated cumulative temperature dataset. Consequently, it can be expected that the observed surface elevation change is connected to and dependent of developments in air temperature. While the Swiss Camp dataset shows the highest correlation over a short time period, the dataset of Box (2013) delivers the best long-term fit of all temperature datasets.

### 7.1.6. Comparison of Recharge Rates with de Quervain & Mercanton (1920)

As showed in chapters 5.11.3 and 6.6.1, the *RRT* and the *RR* have a strong impact on the result and the interpretation that follows. It is therefore interesting to know if the assumed values are comparable to existing data of the area. Luckily, Quervain & Mercanton (1920) combined ablation measurements (with the help of ablation stakes) with surface elevation change measurements that were leveled. This allowed the distinction between the three components ablation, recharge and surface elevation change described in Figure 36. The results for the six points they did these measurements for are listed in Table 18.

*Table 18*: *The different components making up the observed surface elevation change. NK stands for Nunap Kigdlinga, SK for Sermeq Kujalleq. Note that negative values for surface rise actually indicate a surface lowering additionally to the ablation (possibly caused by dynamic effects). Data from de Quervain & Mercanton (1920: 269, 273f), measurement period from 3.7. – 11.8.1912.*

| Point | Area | Surface elevation change (39 days) [m] | Ablation (39 days) [m] | Surface rise (recharge) [m] |
|-------|------|----------------------------------------|------------------------|-----------------------------|
| P$_s$ glace | NK | -0.55 | -0.6 | 0.05 |
| 1 | NK | -1.0 | -1.25 | 0.25 |
| 3 | NK | -1.0 | -1.25 | 0.25 |
| 10 | NK | -1.1 | -1.0 | -0.1 |
| P' | SK | -3.3 | -2.0 | -1.3 |
| P'' | SK | -1.2 | -1.6 | 0.4 |

The difference between P' located close to the terminus at the time and P'' much higher up is explained as follows: *"Le lobe fronto-marginal était encore sous l'influence d'une vague de crue efface déjà en amont de la cataracte"* (de Quervain & Mercanton 1920: 274). They argue that there must have been a 'wave' in the ice-flow, which has already passed P'', but is still affecting P'. Nevertheless, they also state that the uncertainties of their measurements are difficult to estimate but should not be underestimated. Due to this, Point P' is excluded from the calculation of the recharge rate of 1912. If we take the surface rise of all points except P' and calculate the average per month, we get a value of 0.13m/month. This is a value that generally agrees with the recharge rates calculation (see chapter 6.6.1) of 0.14 m/month for the temperature dataset of Box (2013) and 0.13 m/month for the temperature dataset of Swiss Camp. The Ilulissat temperature dataset (Cappelen 2018), which proved less suitable to simulate surface elevation change at the AOI yielded a recharge rate of -0.10 m/month.

## 7.2. DEM Comparability

### 7.2.1. Different Methods of Acquisition

Apart from the GimpDEM, which combines optical and laser altimetry data and DQ12, all DTMs were created using solely optical data.

The optical data was acquired by several different kinds of platforms. The images used for DR16 and DR18 were taken from a UAV, the aerial images used to create SFM59 or the AE85 were taken from airplanes, while the ASTER and ArcticDEM images were taken from satellites. The main difference between these sources is ultimately the spatial and temporal resolution. Disregarding the ArcticDEM, which has a very high spatial resolution, increasing flying altitude leads to a decreasing spatial resolution. In terms of temporal resolution, satellite imagery has more advantages, because it is produced very regularly.

DQ12, which was generated from a topographic map, has very different internal uncertainties, which are hard to measure in hindsight. Unlike for the DTMs generated from aerial images, the original data is not available anymore (or at least not anything apart from the leveled points) and the steps in generating the map can therefore not be retraced. The map is also a product of subjective decisions by P.-L. Mercanton and other contributors to the maps.

For RADAR-derived DTMs an uncertainty to consider when comparing to other datasets, would be the penetration depth in snow and ice. However, in this thesis no RADAR-derived DTMs were used.

### 7.2.2. Spatial Variation of Uncertainty

Something that cannot be quantified with the uncertainty measures presented in this thesis is the spatial variation of uncertainty. Since DEMs derived from optical sources depend on detectable features and high contrast, areas of blank ice can be a challenge, especially if the image is overexposed, as it is the case for a few images of the 1959 aerial images used to create the SFM59.

The ASTER DEMs are another example where this becomes obvious. As Figure 48 and Figure 50 show, the disagreement of ASTER DEMs with other data acquired at roughly the same point in time is much higher in flat areas and ice-covered areas than in rough and steep terrain, where apparently the feature detection works much better.

### 7.2.3. Different Reference Systems

The contemporary datasets used in this thesis did not pose a challenge in harmonizing them to the selected projected reference system (see chapter 5.5.1). However, historic coordinates from the EPF/EGIG expeditions as well as from de Quervain & Mercanton (1920) were more difficult to transform. Luckily, some reference points used by these expeditions are still clearly identifiable today and allow an exact 'co-registration'. Especially point *A14 / 'Höhenmarke 1'*, which is equal to the Sondagsfjell reference point on the 1912 maps, was important (see Figure 68). For the data of de Quervain & Mercanton (1920), the maps were georeferenced using two reference points each, as well as further prominent topography features. All other

positional data for their measurement points was then retrieved from the georeferenced maps. This was not possible for the EGIG/EPF measurement points, because their positional information was not marked in high-resolution maps. Instead, only coordinates in a local and historic Lambert-System were available, which Dr. M. Lüthi found to be about 30m off when reprojected. Thanks to differential re-measurements of A14, this offset could be corrected. This was essential in order to retrieve the positional information of the leveling points out on the ice.



*Figure 68*: Marker of the EGIG reference point 'Höhenmarke 1' (left). Differential measurement of the prominent reference point 'B' (361m, for location see Figure 73 in Appendix A or Figure 86 in Appendix C) in the Sermeq Kujalleq map of de Quervain & Mercanton (1920). Images by Simon Schudel (July 2018).

### 7.2.4. Different Spatial Resolutions

Differing spatial resolutions pose a challenge both for the data processing as well as for the interpretation of the results. To facilitate the processing, it was decided early on to assign all datasets a resolution of either 2m or 10m. As stated in chapter 5.5.1, this led to an upscaling from 25 or 30m resolution to 10m resolution for most of the lower resolution DEMs. This effect on the pixel density is not to be confused with the spatial resolution of the data, which is still that of the original resolution. In the interpretation, it has to be remembered that datasets with an initially lower resolution bring about a smoothing effect. This is visualized in Figure 69, where two fictive DTMs in different resolution (2m and 10m) are used to display the same topography.
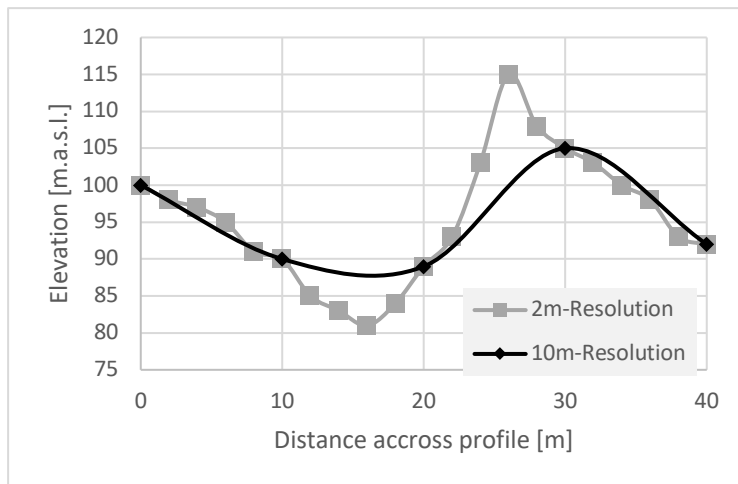
*Figure 69: Fictive example of a terrain displayed in a DTM with a resolution of 2m and in a DTM with a resolution of 10m.*

Note the underestimation of the elevation in convex terrain areas, as well as the overestimation of the elevation in concave terrain areas in the DEM with the 10m resolution. This effect is visible for example in the dh-grids between AS03 and DR18 (see Figure 78) or between GD0309 and DR18 (Figure 79), where the mountain tops are marked with a surface elevation increase and valleys with a surface elevation decrease, when this is actually just an effect of the different spatial resolution. As mentioned above, this smoothing effect is dependent on the original data resolution (e.g. for ASTER DEMs 30m) and not the resampled pixel resolution (e.g. for ASTER DEMs 10m).

### 7.2.5.    Composite vs. Snapshot DEMs

Obviously, the composite DEM (GimpDEM) used in this thesis needs to be viewed carefully, especially in figures where this temporal uncertainty cannot be directly displayed, such as in the planar change maps or the elevation profiles. In the point time series, the temporal uncertainty can be marked with horizontal error bars, which allows a correct interpretation of the data. In general, composite DEMs should not be used to calculate any parameters, which is also the reason why the GimpDEM was disregarded for calculation of the melt rates (see chapter 6.6.3). It can however ease the understanding of the temporal development and provide additional information that is not visible in other available datasets.

## 7.3. Uncertainties and Challenges

### 7.3.1. Data Quality for DQ12

There are several issues of uncertainty associated with the topographic maps of Sermeq Kujalleq and especially Nunap Kigdlinga by de Quervain & Mercanton (1920). There are no data quality assessments in the original publications and the estimation of the uncertainty is difficult in hindsight. In general, the areas between the levelled and measured points in these maps are to be viewed as interpolated sketches. For Sermeq Kujalleq these are surprisingly accurate, since both the glaciomarginal river/creek on the orographic right of the glacier, as well as the ice margin on the orographic left line up perfectly after georeferencing at the two main reference points.

For the Nunap Kigdlinga map, things are a bit different. The topography is not mapped very accurately, and even in the area of stable terrain, certain features clearly identifiable on the map are tricky to find in-situ. Even the second reference point, *'Frysefjeld'* (EPF/EGIG reference point A15) is not as prominent as the map may suggest and could only be determined by taking into account the distance to *'Sondagsfjell'* (EPF/EGIG reference point A14). None of the historic camera locations (1912/1959) supposedly taken from this reference point could be clearly determined (see Figure 2). This, as well as the fact that some of the marked lakes also do not line up nicely, raises the question if this terrain really is that stable. As the example in Figure 70 from ASTER satellite footage shows, lakes can actually be very variable over time.



***Figure 70****: False color footage of two ASTER scenes from 10.07.2012 (left) and 20.08.2012 (right). Circled in yellow is a lake in the forefield which experienced rapid draining within the specified time period.*

Last but not least, there are also several topological errors in the 1912 map of Nunap Kigdlinga (but not in the map of Sermeq Kujalleq). This includes incorrect numbers of contour lines between levelled measurement points, as well as misplaced height spots. A detailed analysis was undertaken (see Figure 71), in order to compensate for topological errors.
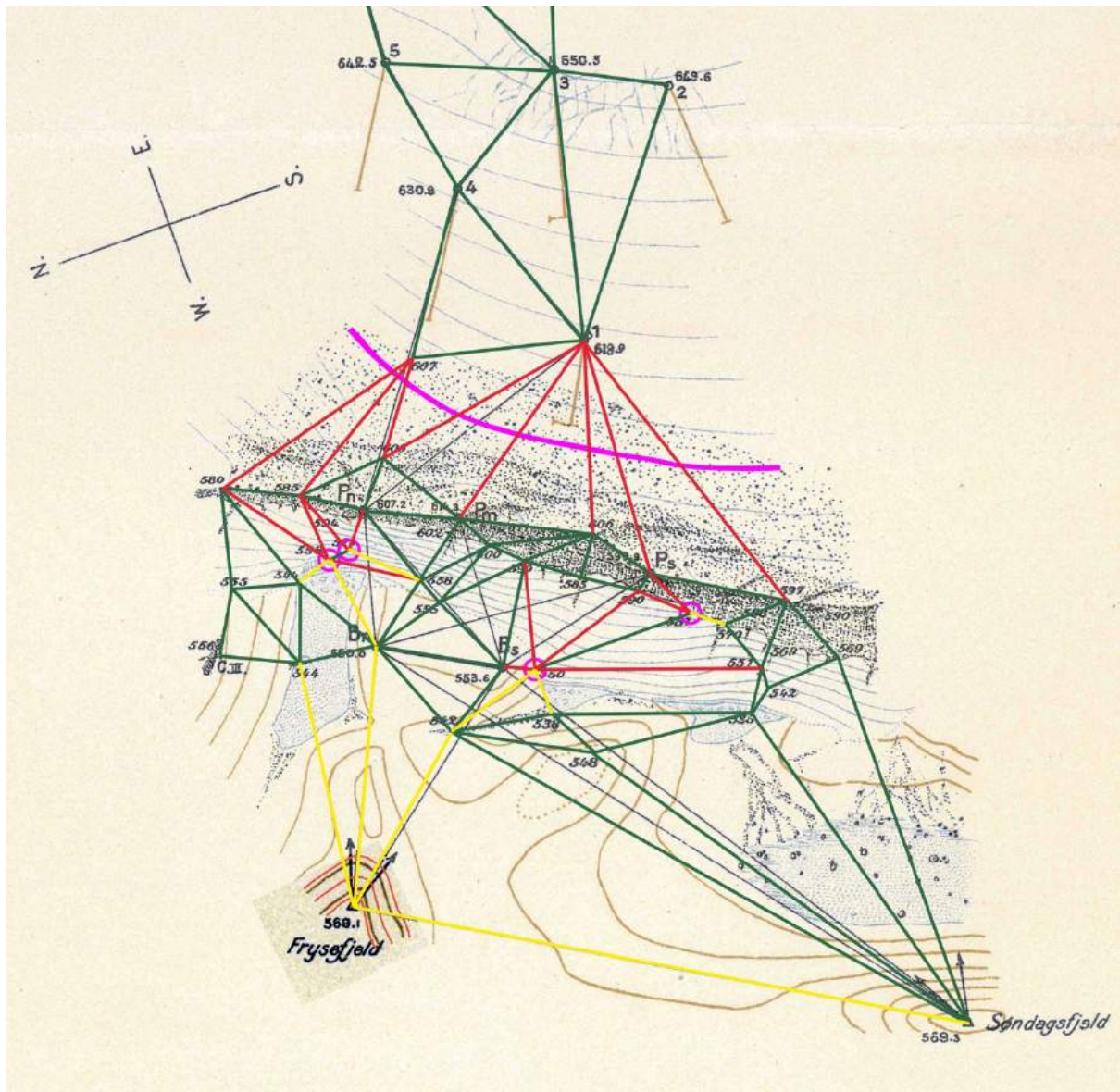
*Figure 71*: *Assessment of topological errors in the 1912 map for Nunap Kigdlinga by de Quervain & Mercanton (1920). The colored lines between the elevation points mark the relation between the number of contour lines and the stated elevation difference between the two points (green = correct number of contour lines, yellow = one missing contour line, red = one supernumerous contour line). In order to correct these errors, the contour line marked in pink was disregarded, the points marked in a pink circle were 'moved' to the correct side of the contour line in question, and for Frysefjeld, an additional contour line was added. Note that the part of the map in the southeast that is not displayed here, did not contain any topological errors.*

The following prioritization of mapped features served as a guideline to correct the topological errors:

1. Leveled measurement points
2. Topographically correct contour lines
3. Sketched (not measured) height spots

All these errors and uncertainties certainly have an impact on the resulting DEM dataset. However, since the uncertainty assessment (see chapter 5.7) was done relative to a reference DEM, these uncertainties are accounted for. That is of course under the assumption that the stable terrain marked in Figure 30 is indeed stable.

101

### 7.3.2. Dome/Bowl Effects in SFM-derived DEMs

When compared to a reference dataset, the 2016 drone DEM exhibits a typical dome effect, where data points of the reference data in the center are lower, data points on the edges higher than for DR16 (see Figure 72).
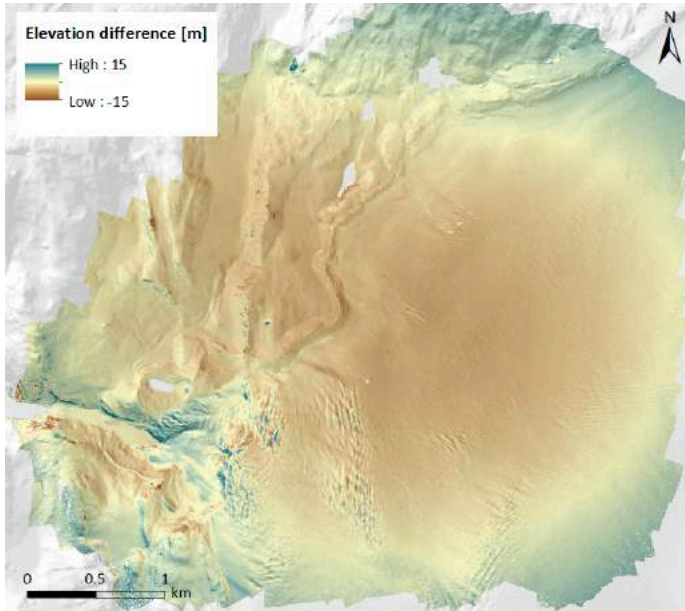


*Figure 72*: Dh-grid between the DR16 and the ArcticDEM composite (ADcomp).

This 'dome' or 'bowl' effect is a common issue in SFM-derived DEMs. As James & Robson (2014) have shown, it can be the result of combining near parallel viewing directions and self-calibrating bundle adjustments. Both applies to the drone image derived DEMs in this research: The images were all taken in nadir direction and are therefore near parallel. And *Agisoft Photoscan* uses a bundle adjustment that estimates both the position of the tie points as well as the internal and external camera alignment and is therefore self-calibrating. Gindraux et al. (2017) identify insufficient GCP density and inexact camera calibrations as other possible reasons. For the 2016 drone DEM there are only GCPs on the non-ice-covered surface, which were introduced in hindsight (see chapter 5.2.1). The GCPs are therefore not evenly distributed and also lack in number. This also leads to a much higher RMSE value of the dataset in respect to the GCPs (see Table 5). One solution to assess the quality on the ice-surface would be the implementation of ground validation points. Indeed, some unmarked locations on the ice had been measured with a handheld GPS in 2016. Using these in-situ measurements as ground validation points would serve as an estimate for the uncertainties in this area (cf. Rossini et al. 2018). However, it can be expected that the uncertainties of the handheld GPS are too big to make reliable estimates.

This dome effect also shows when comparing the data to other datasets of the same period, such as in Figure 48, where the data in the center is clearly affected by a systematic bias if compared to the ArcticDEM of the same period. For all applications relating to elevation change detection, the higher quality AD16 was used (see chapter 6.3). However, only the elevational data is affected by the dome effect and the x- and y-values of DR16 still proved very useful for this thesis – especially for the feature tracking and velocity detection (see chapter 5.10.1).

### 7.3.3.    GCP 'Enforcing' in SFM

In *Agisoft Photoscan*, all GCPs are attributed with their positional information as well as the corresponding uncertainty (Agisoft LLC 2018). The program then positions the points in accordance to the rest of the tie points within this uncertainty and not necessarily at the exact position specified. This had the effect that some of the GCPs with comparably high uncertainties (result of the malfunction of the differential GPS base station), which were used for both the 2016 and 2018 DEM did not end up congruent in the two DEMs and orthophotos. If the main goal of this thesis had been to compare the 2016 and 2018 DEM, then this would be an issue to be corrected. One option to do so would be to 'enforce' the GCPs in *Agisoft Photoscan*, by entering lower uncertainties than actually measured. This would give the program less room to place the respective points. However, since all DEMs (including the 2016 and 2018 drone DEMs) would later be co-registered to another Master DEM anyway (see chapter 5.5), the internal 'correctness' of the dataset was weighed higher than the correctness of the GCPs.

### 7.3.4.    Uncertainties in the Profiles of Nunap Kigdlinga

The profiles of Nunap Kigdlinga were supplemented with leveling data of EPF/EGIG (Bauer 1968c) as well as Zick (1972). This data is generally considered to be more exact than the DEMs of the same age, but they are not free of uncertainty. Apart from the 1971 data, where horizontal uncertainties in the range of a couple of decimeters are stated (Zick 1972), no uncertainty assessment for the points is presented. Moreover, the naming of the points is not entirely consistent over the years. In one instance, there was also a contradiction for an elevation measurement. For the point Y', two different elevations are stated for the year 1952: 595.3 m (Bauer 1968c: 64) and 596.3 m (Bauer 1968c: 70). For this thesis, the mean of the two (595.8 m) was used for this point.

Figure 54 contains a time series of an area. This was done in order to smooth the unnatural noise in certain datasets of this area. However, there are a few limitations to be considered: Due to the filtering of high noise areas and interpolated data (chapter 5.6) or the removal of other faulty cells (see e.g. Figure 29 for the removal of cloud artefacts), some datasets contain void cells. Since these void cells are not evenly distributed across the whole perimeter, but concentrated in patches, the introduced error is affected by spatial autocorrelation. One solution could be to interpolate the void cells with a bilinear interpolation (cf. Denzinger 2018). However, that would also lead to further uncertainties, so it was decided to just use the available data within the specified area.

### 7.3.5.    Uncertainties in Retreat Line Mapping

The retreat of Sermeq Kujalleq as displayed in Figure 40 and Figure 65 is connected to some uncertainties. First of all, the ASTER satellite images used for delineating many of the retreat lines only have a resolution of 15m. A lot of detail is therefore hidden in these images. However, the availability of several spectral bands facilitated the process, because there was additional information apart from the typical RGB images.

Some uncertainty is also connected to debris-covered ice, especially on the orographic left of the glacier lobe. In those areas it can be tricky to distinguish between debris-covered ice and

moraine material. The marked retreat lines are therefore certainly subjective. In general, only ice margins that were rather clear to the author were mapped and otherwise left unmapped in some uncertain segments. Additionally, the mapping uncertainty for each of the sources was estimated and listed in Table 10.

In some mapped years, the mapped ice extent does not coincide with the extent affected by surface lowering at that time. See e.g. Figure 78 (2003), where surface lowering was observed outside of the presumed ice extent, or Figure 81 (2013), where no surface lowering was observed in some areas of the presumed ice extent. Both can be an effect of either erroneous mapping or plausible developments in the terrain: Surface lowering of an ice-cored moraine is possible outside of the presumed ice extent, and debris-covered glacier ice on the other hand may be insulated enough not to experience any surface lowering, while other areas do.

Also note that the 1964 aerial image could only be georeferenced, but not orthorectified, due to a lack of a DEM of that time. Because the image was taken at nadir direction, this uncertainty is negligible though.

# 8.   Conclusion & Outlook

## 8.1.   Conclusion

The aim of thesis was to gain information about the evolution of the land-terminating ice margin of Nunap Kigdlinga and Sermeq Kujalleq over the period of the last century. The concluding outcomes are presented along with the respective research questions.

**a.   How comparable is the data derived from different sources?**
  - **What are the uncertainties associated with each of the datasets?**

The analyzed datasets differ largely in terms of resolution, quality and uncertainty, but after co-registration a comparison of all datasets is possible. That is within the calculated uncertainties, which are found to be best expressed by the Normalized Median Absolute Deviation (NMAD). The datasets can be assigned to three quality groups with similar NMAD values. The highest quality group consisting of the ArcticDEMs has a NMAD value of less than 0.7m. The medium quality group consisting of the two Drone DEMs created with SFM as well as the AeroDEM has NMAD values of 2-5m, while the lowest quality group consisting of the ASTER snapshot DEMs, GimpDEM and SFM-DEM of 1959 and the DEM derived from the 1912 topographic maps, reaches NMAD values of 6 to 12m.

**b.   What is the magnitude, uncertainty and temporal development of the following glacier change parameters: surface lowering, terminus retreat and ice flow velocity?**
  - **How far up the ice can thinning be observed and in what magnitude?**
**c.   How do Nunap Kigdlinga and Sermeq Kujalleq compare in terms of surface elevation change and ice flow velocity?**
  - **Can Sermeq Kujalleq be considered as an 'enhancer' of developments at Nunap Kigdlinga?**

Nunap Kigdlinga and Sermeq Kujalleq underwent very similar temporal changes in terms of surface elevation changes albeit in different magnitudes. The surface elevation was relatively stable between 1912 and 2003, with hints of a slight elevation increase between the 1980s and 2003. Since then a drastic surface lowering has set in, which lasts until today. The speed and magnitude of this surface lowering is unprecedented in the century before this. At Sermeq Kujalleq, the glacier surface lost up to 120 ± 9m of elevation, while at Nunap Kigdlinga the surface lowering was in the range of 20 ± 9m to 30 ± 9m. Thus, Sermeq Kujalleq does behave very similarly to Nunap Kigdlinga but in larger magnitude and could therefore be called 'an enhancer' in this regard. The surface lowering decreases with elevation but goes up beyond the area of interest.

Since 1912, the biggest retreat measured for Sermeq Kujalleq is 601 ±10m, whereat about two thirds of this retreat happened after 2003. The position of the ice margin at Nunap Kigdlinga remained stable, apart from a possible slight advance between 1912 and 1959. The mass loss of Nunap Kigdlinga is therefore predominantly expressed in a down-wasting process. The lack of a horizontal retreat at Nunap Kigdlinga is possibly explained by the dominant debris cover and proglacial snow accumulation but deserves further investigation.

105

The ice flow velocity at Nunap Kigdlinga has remained stable in the range of 15 to 20m/y. Ice flow velocities at Sermeq Kujalleq are more variable and have undergone more dramatic changes due to the changing geometry and ice thickness. While velocities in 2000 were still very similar to those in 1912, the flow velocity at Sermeq Kujalleq plummeted along with the retreat and thinning of that period from more than 50m/y to roughly half of that since 2000.

d. **Can the temporal developments in surface elevation change be linked to changes in temperature?**

• **Which temperature dataset best represents the changes observed?**

It is possible to recreate the measured surface elevation changes with temperature data using an adapted Positive Degree Month Model. Certain simplifying assumptions are necessary to do so, and it is assumed that the ice recharge rate is constant and dynamic ice flow influences as well as precipitation are ignored. Under these assumptions the surface elevation change reconstruction using calibrated cumulative temperatures yields a result which is very similar to the measured surface elevation change, which suggests a strong connection between changes in temperature and surface elevation. The temperature dataset of Box (2013) delivered the best results of all analyzed temperature datasets.

## 8.2. Outlook

In order to further improve the quality of the used datasets as well as foster the understanding of the area, certain improvements in the workflow of this thesis seem feasible. There are several possibilities to improve the SFM59 dataset, which could lead to more accurate results and a better-quality DEM. The main issue is the elevation-dependent bias described in chapter 6.2.1. One way to eliminate this bias would be to follow the procedure by Nuth & Kääb (2011) as laid out in chapter 5.5. Another option would be to use the 1959 leveling points not only to get a better fit of the finished dataset in the Nunap Kigdlinga area, but to implement them as proper GCPs. The second issue with the dataset is the high spatial variability in certain areas. It seems like the threshold when filtering the high-noise areas (see chapter 5.6.1) should have been selected to be higher. Instead of filtering out such areas post-SFM, it could also be dealt with before generating the DEM. Either the point cloud could be edited and filtered with appropriate software such as *RiSCAN Pro* (RIEGL 2016), or the DEM could be generated from a mesh rather than directly from the dense point cloud. This intermediate step would help smooth such problematic areas, as described e.g. by Mertes et al. (2017).

As mentioned in chapter 5.5.5, the combining of the two maps of 1912 into the DQ12 dataset was done by individually calculating the offsets to the ADcomp dataset, which was selected as the master DEM for the co-registration process. However, the results differed by around 7m, which may be the explanation for the two-peaked histogram for DQ12 in Figure 43. Maybe the agreement could have been improved by looking at the two maps not as two individual datasets with individual uncertainties, but rather one dataset which is treated equally. Another improvement could have been achieved by calculating the offsets in respect to the differential GPS measurements, rather than the ADcomp dataset. For the co-registration of all other datasets, consistency in the workflow would be improved if the median and the NMAD as robust estimators for uncertainty were used to determine the number of iterations in the co-registration process rather than the mean error and the standard deviation.

The $\Delta T^+$-approach introduced in this thesis to determine *RRT* turned out to deliver rather inconsistent results for the three different temperature datasets. One way to improve the results as well as the continuity in the workflow would be to redefine the monthly average. Like for the trendline approach, only the mean of the years where the glacier is in an equilibrium should be considered (namely 1912-2003). Despite the unsatisfying results in this thesis, the approach should be applied in other research in order to find out why the difference between the two approaches can be so large.

Despite all the possible improvements, this thesis delivers an important contribution in the assessment of land-terminating ice margins in Greenland. The unprecedented time-series and spatial resolution for direct measurements of such an area help to close the knowledge gaps associated with these types of ice margins. More historic data, especially high-resolution scans of aerial images such as the oblique images from 1949 (Hansen 1968) can be expected to surface in the future and could provide an interesting addition to this research. Moreover, Nunap Kigdlinga and Sermeq Kujalleq make up an area of unmatched data availability and are therefore suitable for analysis in other aspects, which were not covered in this thesis. One

interesting topic to further investigate would certainly be the moraine and debris at Nunap Kigdlinga: Where does it come from, how does it affect the dynamics at the margin? Where is the actual ice-margin? Is the ice-cored moraine still in motion? How does the clear border between clean and dirty ice behave and move or melt out over time and why? This is just a selection of questions to be answered. Isotope records by Clausen & Stauffer (1988) as well as recent, unpublished research of Dr. Martin Lüthi suggest that a clear border of ice originating in the last ice age (Wisconsin glacial episode) and Holocene ice is located close to the ice margin, which would also deserve further investigation.

Apart from further research in the same area, this thesis should also be seen as an encouragement for the investigation of other land-terminating ice margins. The study site displayed vast changes in surface elevation and ice extent since about 2003, synchronous with the close-by marine-terminating Eqip Sermia. This time period is well documented by remote sensing data in most areas, thus allowing a similar approach also in areas with less available historical data. Researching other land-terminating margins and comparing their evolution with nearby marine-terminating glaciers could help to determine whether the study site is an exception in 'following' the fast retreat of marine-terminating glaciers, as studies by Bjørk et al. (2012) or Sole et al. (2008) suggest, or if it is a new large-scale development previously unseen.

# 9. Literature

Agisoft LLC (2018). Agisoft PhotoScan User Manual – Professional Edition, Version 1.4. Available at: http://www.agisoft.com/pdf/photoscan-pro_1_4_en.pdf [Accessed October 23, 2018].

Ahlstrøm, A.P. et al. (2008). Estimating the future ice sheet hydropower potential in Paakitsoq, Ilulissat, West Greenland. In *AGU Fall Meeting Abstracts.* San Francisco.

Airbus Defence & Space (2018). Elevation Models – The right elevation model for all your project needs. Available at: https://www.intelligence-airbusds.com/elevation-models/ [Accessed October 19, 2018].

Arnold, N.S. et al. (1996). A distributed surface energy-balance tnodel for a small valley glacier. – Development and testing for Haut Glacier d'Arolla, Valais, Switzerland. *Journal of Glaciology*, 42(140), pp.77–89. (doi: 10.3189/S0022143000030549)

Baltsavias, E.P. (1999). A comparison between photogrammetry and laser scanning. *ISPRS Journal of Photogrammetry and Remote Sensing*, 54, pp.83–94. (doi: 10.1016/S0924-2716(99)00014-3)

Bamber, J.L., Ekholm, S. & Krabill, W.B. (2001). A new, high-resolution digital elevation model of Greenland fully validated with airborne laser altimeter data. *Journal of Geophysical Research B: Solid Earth*, 106(B4), pp.6733–6745. (doi: 10.1029/2000JB900365)

Barr, W. (2015). Alfred de Quervain's Swiss Greenland expeditions, 1909 and 1912. *Polar Record*, 89(2), pp.366–385. (doi: 10.1017/S0032247414000199)

Bartusch, M. et al. (2009). TanDEM-X – Die Erde in drei Dimensionen. E. Mittelbach, ed., Bonn-Oberkassel, Germany: Deutsches Zentrum für Luft- und Raumfahrt e.V. (DLR). Available at: http://www.dlr.de/dlr/en/Portaldata/1/Resources/documents/TanDEM-X_web.pdf [Accessed October 29, 2018]

Bauer, A. (1953). Frontverschiebungen des Gletschers Eqip Sermia, West·Grönland 1912-1953. *Polarforschung*, 23(1/2), pp.234–235.

Bauer, A. (1955). Glaciologie Groenland II. le glacier de l'Eqe. Librairie Scientifique Hermann, ed., Paris: Actualités Scientifiques et Industrielles.

Bauer, A. (1968a). Le Glacier de l'Eqe (Eqip Sermia) – Mouvement et variations du front (1959), Copenhagen: C.A. Reitzels Forlag.

Bauer, A. (1968b). Missions aériennes de reconnaissance au Groenland 1957-1958. Copenhagen: C.A. Reitzels Forlag.

Bauer, A. (1968c). Mouvement et variation d'altitude de la zone d'ablation ouest de l'indlandsis du groenland entre 1948 et 1959. Copenhagen: C.A. Reitzels Forlag.

Bauer, A. (1954). The Balance of the Greenland Ice Sheet. *Journal of Glaciology*, 2(17), pp.456–462.

Bauer, A. & Carbonnell, M. (1968). Exploitation des couvertures photographiques aériennes répétées du front des glaciers vêlant dans Disko Bugt et Umanak Fjord, Juin-Juillet 1964. *Meddelelser om Grønland*, 173(5), p.78.

Benn, D.I. & Evans, D.J.A. (2010). Glaciers & Glaciation. 2nd ed., London: Hodder Education. (doi: 10.1017/CBO9781107415324.004)

Bhardwaj, A. et al. (2016). UAVs as remote sensing platform in glaciology: Present applications and future prospects. *Remote Sensing of Environment*, 175, pp.196–204. (doi: 10.1016/j.rse.2015.12.029)

Bjørk, A.A. et al. (2012). An aerial view of 80 years of climate-related glacier fluctuations in southeast Greenland. *Nature Geoscience*, 5(6), pp.427–432. (doi: 10.1038/ngeo1481)

Bjørk, A.A., Kruse, L.M. & Michaelsen, P.B. (2015). Brief communication: Getting Greenland's glaciers right - A new data set of all official Greenlandic glacier names. *Cryosphere*, 9(6), pp.2215–2218. (doi: 10.5194/tc-9-2215-2015)

Box, J.E. (2013). Greenland ice sheet mass balance reconstruction. Part II: Surface mass balance (1840-2010). *Journal of Climate*, 26(18), pp.6974–6989. (doi: 10.1175/JCLI-D-12-00518.1)

Box, J.E. & Steffen, K. (2000). Greenland Climate Network (GC-NET) – Data Reference. Boulder, CO. Available at: http://cires1.colorado.edu/steffen/gcnet/Gc-net_documentation_Nov_10_2000.pdf [Accessed January 11, 2019]

Braithwaite, R.J. (1995). Positive degree-day factors for ablation on the Greenland ice sheet studied by energy balance modelling. *Journal of Glaciology*, 41(137), pp.153–160. (doi: 10.3189/S0022143000017846)

Braithwaite, R.J. & Olesen, O.B. (1990). A simple energy-balance model to calculate ice ablation at the margin of the Greenland ice sheet. *Journal of Glaciology*, 36(123), pp.222–228. (doi: 10.1017/S0022143000009473)

Burns, J.H.R. & Delparte, D. (2017). Comparison of commercial structure-from-motion photogrammety software used for underwater three-dimensional modeling of coral reef environments. *International Archives of the Photogrammetry, Remote Sensing and Spatial Information Sciences - ISPRS Archives*, 42(2W3), pp.127–131. (doi: 10.5194/isprs-archives-XLII-2-W3-127-2017)

Candela, S.G. et al. (2016). Automated topographic change detection via dem differencing at large scales using the ArcticDEM database. In *2016 AGU Fall Meeting Abstracts*. San Francisco.

Cappelen, J. (2018). DMI Historical Climate Data Collection 1784-2017. J. Cappelen, ed., Copenhagen, DK. Available at: http://www.dmi.dk/laer-om-generelt/dmi-publikationer/ [Accessed December 17, 2018]

Carrivick, J.L. et al. (2017). Ice-margin and meltwater dynamics during the mid-Holocene in the Kangerlussuaq area of west Greenland. *Boreas*, 46(3), pp.369–387. (doi: 10.1111/bor.12199)

Chauché, N. et al. (2014). Ice-ocean interaction and calving front morphology at two west Greenland tidewater outlet glaciers. *Cryosphere*, 8(4), pp.1457–1468. (doi: 10.5194/tc-8-1457-2014)

Childs, C. (2004). Interpolating Surfaces in ArcGIS Spatial Analyst. *ArcUser*, pp.32–35. Available at: https://www.esri.com/news/arcuser/0704/files/interpolating.pdf [Accessed October 9, 2018]

Clausen, H.B. & Stauffer, B. (1988). Analyses of two ice cores drilled at the ice-sheet margin in West Greenland. *Annals of Glaciology*, 10, pp.23–27.

Dai, C. et al. (2018). Estimating River Surface Elevation From ArcticDEM. *Geophysical Research Letters*, 45(7), pp.3107–3114. (doi: 10.1002/2018GL077379)

Dai, C. & Howat, I.M. (2017). Measuring Lava Flows With ArcticDEM: Application to the 2012–2013 Eruption of Tolbachik, Kamchatka. *Geophysical Research Letters*, 44(24), p.12,133-12,140. (doi: 10.1002/2017GL075920)

Davis, C.H. & Sun, S. (2004). Long-term thinning of the southeast Greenland ice sheet from Seasat, Geosat, and GFO satellite radar altimetry. *IEEE Geoscience and Remote Sensing Letters*, 1(2), pp.47–50. (doi: 10.1109/LGRS.2004.824742)

Denzinger, F. (2018). Structure from Motion using historical aerial images to analyse changes in surface elevation and volume on Abramov Glacier, Kyrgyzstan. Master's Thesis. University of Zurich.

Dowdeswell, J.A. (2006). Global Sea-Level Rise. *Science*, 311, pp.963–964. (doi: 10.1126/science.1124190)

Eineder, M. & Holzner, J. (2000). Interferometric DEMs in Alpine Terrain – Limits and Options for ERS and SRTM. *Proceedings Geoscience and Remote Sensing Symposium (IGARS)*, 7, pp.3210–3212. (doi: 10.1109/IGARSS.2000.860385)

Ekholm, S. (1996). A full coverage, high-resolution, topographic model of Greenland computed from a variety of digital elevation data. *Journal of Geophysical Research*, 101(B10), pp.21961–21972. (doi: 10.1029/96JB01912)

EORC & JAXA (2018). ALOS Global Digital Surface Model (DSM) – ALOS World 3D-30m (AW3D30), Version 2.1, Product Description. Available at: https://www.eorc.jaxa.jp/ALOS/en/aw3d30/aw3d30v21_format_e.pdf [Accessed October 26, 2018].

ETHZ Library Image Archive (2019). E-Pics Collection. Available at: https://ba.e-pics.ethz.ch [Accessed January 21, 2019].

European Commission (2015). Copernicus – Europe's eyes on Earth. Brussels, Belgium. (doi: 10.2873/93104)

De Feranti, J. (2014). Viewfinder Panorama DEM. Available at: http://www.viewfinderpanoramas.org/ [Accessed October 19, 2018].

Fettweis, X. et al. (2017). Reconstructions of the 1900–2015 Greenland ice sheet surface mass balance using the regional climate MAR model. *The Cryosphere*, 11(2), pp.1015–1033. (doi: 10.5194/tc-11-1015-2017)

Fisher, P.F. & Tate, N.J. (2006). Causes and consequences of error in digital elevation models. *Progress in Physical Geography*, 30(4), pp.467–489. (doi: 10.1191/0309133306pp492ra)

Fitzpatrick, A.A.W. et al. (2013). Ice flow dynamics and surface meltwater flux at a land-terminating sector of the Greenland ice sheet. *Journal of Glaciology*, 59(216), pp.687–696. (doi: 10.3189/2013JoG12J143)

Fonstad, M.A. et al. (2013). Topographic structure from motion: A new development in photogrammetric measurement. *Earth Surface Processes and Landforms*, 38(4), pp.421–430. (doi: 10.1002/esp.3366)

Frey, H. & Paul, F. (2012). On the suitability of the SRTM DEM and ASTER GDEM for the compilation of topographic parameters in glacier inventories. *International Journal of Applied Earth Observation and Geoinformation*, 18(1), pp.480–490. (doi: 10.1016/j.jag.2011.09.020)

Furukawa, Y. & Ponce, J. (2010). Accurate, dense, and robust multiview stereopsis. *IEEE Transactions on Pattern Analysis and Machine Intelligence*, 32(8), pp.1362–1376. (doi: 10.1109/TPAMI.2009.161)

Gindraux, S., Boesch, R. & Farinotti, D. (2017). Accuracy assessment of digital surface models from Unmanned Aerial Vehicles' imagery on glaciers. *Remote Sensing*, 9(2), pp.1–15. (doi: 10.3390/rs9020186)

Google Earth (2018). DigitalGlobe Imagery. Available at: https://google.com/earth/ [Accessed March 16, 2018].

Håkansson, L. et al. (2014). Slow retreat of a land based sector of the West Greenland Ice Sheet during the Holocene Thermal Maximum: evidence from threshold lakes at Paakitsoq. *Quaternary Science Reviews*, 98, pp.74–83. (doi: 10.1016/j.quascirev.2014.05.016)

Hanna, E. et al. (2011). Greenland Ice Sheet surface mass balance 1870 to 2010 based on Twentieth Century Reanalysis, and links with global climate forcing. *Journal of Geophysical Research Atmospheres*, 116(24), pp.1–20. (doi: 10.1029/2011JD016387)

Hansen, K. (1968). Glacialgeologiske og sedimentologiske undersøgelser ved Eqe – Vestgrønland. Copenhagen.

Hemond, H.F. & Fechner, E.J. (2015). 4.2.1 The Dry Adiabatic Lapse Rate. In *Chemical Fate and Transport in the Environment (Third Edition)*. Boston, MA: Elsevier B.V., pp. 311–454. (doi: 10.1016/B978-0-12-398256-8.00004-9)

Hock, R. (2003). Temperature index melt modelling in mountain areas. *Journal of Hydrology*, 282(1–4), pp.104–115. (doi: 10.1016/S0022-1694(03)00257-9)

Hofmann, W. (1964). Die Geodätische Lagemessung über das Grönländische Inlandeis der internationalen glaziologischen Grönland-Expedition (EGIG) 1959. Copenhagen, DK.

Höhle, J. & Höhle, M. (2009). Accuracy assessment of digital elevation models by means of robust statistical methods. *ISPRS Journal of Photogrammetry and Remote Sensing*, 64(4), pp.398–406. (doi: 10.1016/j.isprsjprs.2009.02.003)

Holland, D.M. et al. (2008). Acceleration of Jakobshavn Isbræ triggered by warm subsurface ocean waters. *Nature Geoscience*, 1, pp.659–664. (doi: 10.1038/ngeo316)

Holtzscherer, J.-J. & Bauer, A. (1954). Contribution à la connaissance de l'inlandsis du Groenland. Paris, F.

Howat, I.M. et al. (2005). Rapid retreat and acceleration of Helheim Glacier, east Greenland. *Geophysical Research Letters*, 32(22), pp.1–4. (doi: 10.1029/2005GL024737)

Howat, I.M., Negrete, A. & Smith, B.E. (2014). The Greenland Ice Mapping Project (GIMP) land classification and surface elevation data sets. *Cryosphere*, 8(4), pp.1509–1518. (doi: 10.5194/tc-8-1509-2014)

Hutchinson, M.F. (1989). A new procedure for gridding elevation and stream line data with automatic removal of spurious pits. *Journal of Hydrology*, 106(3–4), pp.211–232. (doi: 10.1016/0022-1694(89)90073-5)

Hutchinson, M.F., Xu, T. & Stein, J.A. (2011). Recent Progress in the ANUDEM Elevation Gridding Procedure. In T. Hengl et al., eds. *Proceedings of the Geomorphometry*. Redlands, CA, USA, pp. 19–22. (doi: 10.1002/osp4.29)

Immerzeel, W.W. et al. (2014). High-resolution monitoring of Himalayan glacier dynamics using unmanned aerial vehicles. *Remote Sensing of Environment*, 150, pp.93–103. (doi: 10.1016/j.rse.2014.04.025)

James, M.R. et al. (2017). Optimising UAV topographic surveys processed with structure-from-motion: Ground control quality, quantity and bundle adjustment. *Geomorphology*, 280, pp.51–66. (doi: 10.1016/j.geomorph.2016.11.021)

James, M.R. & Robson, S. (2014). Mitigating systematic error in topographic models derived from UAV and ground-based image networks. *Earth Surface Processes and Landforms*, 39(10), pp.1413–1420. (doi: 10.1002/esp.3609)

Jaud, M. et al. (2016). Assessing the accuracy of high resolution digital surface models computed by PhotoScan® and MicMac® in sub-optimal survey conditions. *Remote Sensing*, 8(465), pp.1–18. (doi: 10.3390/rs8060465)

Joughin, I. et al. (2010). Greenland flow variability from ice-sheet wide velocity mapping. *Journal of Glaciology*, 56(197), pp.415–430. (doi: 10.3189/002214310792447734)

Joughin, I. et al. (2015, updated 2018). MEaSUREs Greenland Ice Sheet Velocity Map from InSAR Data, Version 2 – Greenland Velocity Mosaic 200, velocity magnitude. NASA National Snow and Ice Data Center Distributed Active Archive. Boulder, CO. (doi: 10.5067/OC7B04ZM9G6Q)

Jouvet, G. et al. (2017). Initiation of a major calving event on the Bowdoin Glacier captured by UAV photogrammetry. *Cryosphere*, 11(2), pp.911–921. (doi: 10.5194/tc-11-911-2017)

Kääb, A. (2005). Remote Sensing of Mountain Glaciers and Permafrost Creep. W. Häberli & M. Maisch, eds., Zürich, CH: Geographisches Institut der Universität Zürich. (doi: 10.3189/172756507781833857)

Kaplan, E.D. & Hegarty, C.J. (2006). Differential GPS. In E. D. Kaplan & C. J. Hegarty, eds. *Understanding GPS – principles and applications*. Norwood, MA: ARTECH House, Inc., pp. 379–454. ISBN 1-58053-894-0

Kelley, S.E. et al. (2012). Maximum late Holocene extent of the western Greenland Ice Sheet during the late 20th century. *Quaternary Science Reviews*, 56, pp.89–98. (doi: 10.1016/j.quascirev.2012.09.016)

Kjeldsen, K.K. et al. (2015). Spatial and temporal distribution of mass loss from the Greenland Ice Sheet since AD 1900. *Nature*, 528(7582), pp.396–400. (doi: 10.1038/nature16183)

Korona, J. et al. (2009). SPIRIT. SPOT 5 stereoscopic survey of Polar Ice: Reference Images and Topographies during the fourth International Polar Year (2007-2009). *ISPRS Journal of Photogrammetry and Remote Sensing*, 64(2), pp.204–212. (doi: 10.1016/j.isprsjprs.2008.10.005)

Korsgaard, N., Weng, W. & Kjær, K.H. (2017). AirBase - A database of 160,000 aerial photos of Greenland 1930-1980s. In *Geophysical Research Abstracts*. EGU General Assembly 2017. Vienna.

Korsgaard, N.J. et al. (2016). Data Descriptor: Digital elevation model and orthophotographs of Greenland based on aerial photographs from 1978 – 1987. *Scientific Data*, 3, pp.1–15. (doi: 10.1038/sdata.2016.32)

Kraaijenbrink, P.D.A. et al. (2016). Object-based analysis of unmanned aerial vehicle imagery to map and characterise surface features on a debris-covered glacier. *Remote Sensing of Environment*, 186, pp.581–595. (doi: 10.1016/j.rse.2016.09.013)

Larsen, N.K. et al. (2016). Holocene ice marginal fluctuations of the Qassimiut lobe in South Greenland. *Scientific Reports*, 6(March), pp.1–11. (doi: 10.1038/srep22362)

Lemos, A. et al. (2018). Seasonal Variations in the Flow of Land-Terminating Glaciers in Central-West Greenland Using Sentinel-1 Imagery. *Remote Sensing*, 10, pp.1–12. (doi: 10.3390/rs10121878)

LeSchack, L.A. (1964). The French Polar Effort and the Expeditions Polaires Francaises. *Arctic*, 17(1), pp.1–14. (doi: 10.14430/arctic3480)

Lesnek, A.J. & Briner, J.P. (2018). Response of a land-terminating sector of the western Greenland Ice Sheet to early Holocene climate change: Evidence from 10Be dating in the Søndre Isortoq region. *Quaternary Science Reviews*, 180, pp.145–156. (doi: 10.1016/j.quascirev.2017.11.028)

Levy, L. et al. (2016). Fluctuations of the Greenland Ice Sheet since the last ice age: comparisons of the response of marine and land-terminating ice margins to Holocene climate changes. In *Geophysical Research Abstracts*. EGU General Assembly 2016, Vienna. p. 8902.

Lowe, D.G. (2004). Distinctive Image Features from Scale-Invariant Keypoints. *International Journal of Computer Vision*, 60(2), pp.91–110. (doi: 10.1023/B:VISI.0000029664.99615.94)

Lozowski, E.P. et al. (1989). The Use of Cumulative Monthly Mean Temperature Anomalies in the Analysis of Interannual Climate Variability. Alberta, Canada.

Lüthi, M.P. et al. (2016). A century of geometry and velocity evolution at Eqip Sermia, West Greenland. *Journal of Glaciology*, 62(234), pp.640–654. (doi: 10.1017/jog.2016.38)

Maune, D.F. et al. (2001). Introduction. In D. F. Maune, ed. *Digital Elevation Model Technologies and Applications: The DEM Users Manual.* Bethesda, Maryland: American Society for Photogrammetry and Remote Sensing, p. 537.

Mercanton, P.-L. (1914). En marge de l'inlandsis – Chronique du "Groupe de l'ouest" de l'expedition suisse au Groenland 1912-13. In *Bibliothèque Universelle et Revue Suisse1*. Lausanne, pp. 295–328.

Mernild, S.H. et al. (2012). Multi-decadal marine- and land-terminating glacier recession in the Ammassalik region, southeast Greenland. *Cryosphere*, 6(3), pp.625–639. (doi: 10.5194/tc-6-625-2012)

Mertes, J.R. et al. (2017). Using structure-from-motion to create glacier DEMs and orthoimagery from historical terrestrial and oblique aerial imagery. *Earth Surface Processes and Landforms*, 42(14), pp.2350–2364. (doi: 10.1002/esp.4188)

Mölg, N. & Bolch, T. (2017). Structure-from-motion using historical aerial images to analyse changes in glacier surface elevation. *Remote Sensing*, 9(10). (doi: 10.3390/rs9101021)

Morin, P. et al. (2016). ArcticDEM; A Publically Available, High Resolution Elevation Model of the Arctic. In *Geophysical Research Abstracts*. Vienna.

Morlighem, M., Williams, C.N., et al. (2017). BedMachine v3: Complete Bed Topography and Ocean Bathymetry Mapping of Greenland From Multibeam Echo Sounding Combined With Mass Conservation. *Geophysical Research Letters*, 44(21), p.11'051-11'061. (doi: 10.1002/2017GL074954)

Morlighem, M., Williams, C., et al. (2017). IceBridge BedMachine Greenland, Version 3. (doi: 10.5067/2CIX82HUV88Y)

Müller, T. (2016). Lotsendienste für 57 Kronen. *UZH News – Transactions – Geld, Glück, Gesundheit, Gerechtigkeit*. Available at: https://www.news.uzh.ch/de/articles/2016/transactions-groenland-expedition.html [Accessed January 21, 2019].

Murray, T. et al. (2010). Ocean regulation hypothesis for glacier dynamics in southeast Greenland and implications for ice sheet mass changes. *Journal of Geophysical Research: Earth Surface*, 115(3), pp.1–15. (doi: 10.1029/2009JF001522)

NGA & NSF (2018). Guide: Introduction to ArcticDEM. Available at: https://www.pgc.umn.edu/guides/arcticdem/introduction-to-arcticdem/ [Accessed October 17, 2018].

Niederheiser, R. et al. (2016). Deriving 3D point clouds from terrestrial photographs - Comparison of different sensors and software. *International Archives of the Photogrammetry, Remote Sensing and Spatial Information Sciences - ISPRS Archives*, 41(June), pp.685–692. (doi: 10.5194/isprsarchives-XLI-B5-685-2016)

Nuth, C. & Kääb (2011). Co-registration and bias corrections of satellite elevation data sets for quantifying glacier thickness change. *Cryosphere*, 5(1), pp.271–290. (doi: 10.5194/tc-5-271-2011)

Paredes, J.A. et al. (2017). Study of effects of high-altitude environments on multicopter and fixed-wing UAVs' energy consumption and flight time. In *IEEE International Conference on Automation Science and Engineering*. Xi'an, China, pp. 1645–1650. (doi: 10.1109/COASE.2017.8256340)

Pelliciotti, F. et al. (2005). An enhanced temperature-index glacier melt model including the shortwave radiation balance: development and testing for Haut Glacier d'Arolla, Switzerland. *Journal of Glaciology*, 51(175), pp.573–587. (doi: 10.3189/172756505781829124)

Pellitero, R. et al. (2016). GlaRe, a GIS tool to reconstruct the 3D surface of palaeoglaciers. *Computers and Geosciences*, 94, pp.77–85. (doi: 10.1016/j.cageo.2016.06.008)

Porter, C. et al. (2018). Arctic DEM V3. (doi: 10.7910/DVN/OHHUKH)

Pritchard, H.D. et al. (2009). Extensive dynamic thinning on the margins of the Greenland and Antarctic ice sheets. *Nature*, 461(7266), pp.971–975. (doi: 10.1038/nature08471)

de Quervain, A. & Mercanton, P.-L. (1920). Ergebnisse der Schweizerischen Grönlandexpedition 1912-1913. Zürich.

de Quervain, A. & Mercanton, P.-L. (1925). Résultats scientifiques de l'expédition suisse au Groenland 1912-1913. Copenhagen: Bianco Lunos Bogtrykkeri.

Rabot, C. & Mercanton, P.L. (1913). Les variations périodiques des glaciers. XVIII me Rapport, 1912. *Zeitschrift für Gletscherkunde*, (VIII), pp.42–62.

RIEGL (2016) *Operating & Processing Software RiSCAN PRO – Data Sheet*, Orlando, FL. Available at: http://www.riegl.com/uploads/tx_pxpriegldownloads/11_DataSheet_RiSCAN-PRO__2016-01-13.pdf [Accessed at October 29, 2018]

Rignot, E., Echelmeyer, K. & Krabill, W.B. (2001). Penetration depth of interferometric synthetic aperture radar signals in snow and ice. *Geophysical Research Letters*, 28(18), pp.3501–3504. (doi: 10.1029/2000GL012484)

Rignot, E. & Kanagaratnam, P. (2006). Changes in the Velocity Structure of the Greenland Ice Sheet. *Science*, 311(5763), pp.986–990. (doi: 10.1126/science.1121381)

Rossini, M. et al. (2018). Rapid melting dynamics of an alpine glacier with repeated UAV photogrammetry. *Geomorphology*, 304, pp.159–172. (doi: 10.1016/j.geomorph.2017.12.039)

Ryan, J.C. et al. (2015). UAV photogrammetry and structure from motion to assess calving dynamics at Store Glacier, a large outlet draining the Greenland ice sheet. *Cryosphere*, 9(1), pp.1–11. (doi: 10.5194/tc-9-1-2015)

Scambos, T.A. & Haran, T. (2002). An image-enhanced DEM of the Greenland ice sheet. *Annals of Glaciology*, 34, pp.291–298. (doi: 10.3189/172756402781817969)

Seckel, H. (1977a). Das geometrische Nivellement über das Grönländische Inlandeis der Gruppe Nivellement A der internationalen glaziologischen Grönland Expedition 1967-68. *Meddelelser om Grønland*, 187(3), p.86.

Seckel, H. (1977b). Höhenänderungen im Grönländischen Inlandeis zwischen 1959 und 1968. Copenhagen: Nyt Nordisk Forlag Arnold Busck.

Slater, J.A. et al. (2011). Global Assessment of the New ASTER Global Digital Elevation Model. *Photogrammetric Engineering & Remote Sensing*, 77(4), pp.335–349. (doi: 10.14358/PERS.77.4.335)

Smith, M.W., Carrivick, J.L. & Quincey, D.J. (2015). Structure from motion photogrammetry in physical geography. *Progress in Physical Geography*, 40(2), pp.247–275. (doi: 10.1177/0309133315615805)

Snavely, N., Seitz, S. & Szeliski, R., 2006. Photo tourism: exploring photo collections in 3D. *ACM Transactions on Graphics*, 1(25), pp.835–846.

Solbø, S. & Storvold, R. (2013). Mapping Svalbard Glaciers With the Cryowing Uas. *ISPRS - International Archives of the Photogrammetry, Remote Sensing and Spatial Information Sciences*, XL-1/W2, pp.373–377. (doi: 10.5194/isprsarchives-XL-1-W2-373-2013)

Sole, A. et al. (2008). Testing hypotheses of the cause of peripheral thinning of the Greenland Ice Sheet: Is land-terminating ice thinning at anomalously high rates? *Cryosphere*, 2(2), pp.205–218. (doi: 10.5194/tc-2-205-2008)

Tachikawa, T. et al. (2011). Characteristics of ASTER GDEM version 2. *2011 IEEE International Geoscience and Remote Sensing Symposium*, pp.3657–3660. (doi: 10.1109 / IGARSS.2011.6050017)

Tadono, T. et al. (2014). Precise Global DEM Generation by ALOS PRISM. *ISPRS Annals of Photogrammetry, Remote Sensing and Spatial Information Sciences*, II(4), pp.71–76. (doi: 10.5194/isprsannals-II-4-71-2014)

Tedstone, A.J. et al. (2015). Decadal slowdown of a land-terminating sector of the Greenland Ice Sheet despite warming. *Nature*, 526(7575), pp.692–695. (doi: 10.1038/nature15722)

Tschaen, L. (1959). Groenland 1948 - 1949 -1950 – Astronomie - Nivellement Géodésique sur l'Inlandsis, Nouveau Calcul, Paris.

Turner, D., Lucieer, A. & Wallace, L. (2014). Direct georeferencing of ultrahigh-resolution UAV imagery. *IEEE Transactions on Geoscience and Remote Sensing*, 52(5), pp.2738–2745. (doi: 10.1109/TGRS.2013.2265295)

U.S./Japan ASTER Science Team (2007). ASTER On-Demand L3 DEM and Orthorectified Images, GeoTIF Format. (doi: 10.5067/ASTER/AST14DMO.003)

USGS (2008). Declassified Intelligence Satellite Photographs: Fact Sheet. Sioux Falls, SD. Available at: http://pubs.usgs.gov/fs/2008/3054/pdf/fs2008-3054.pdf [Accessed December 5, 2018]

USGS (2016). Landsat – Earth observation satellites: Fact Sheet. Sioux Falls, SD. (doi: 10.3133/fs20153081)

Walter, A. (2016). Estimation of Glacier Melt and Discharge of the Eqip Glacier, a Calving Outlet Glacier in Greenland. Master's Thesis. University of Zurich.

Weidick, A., Kelly, M. & Bennike, O. (2004). Late Quaternary development of the southern sector of the Greenland Ice Sheet, with particular reference to the Qassimiut lobe. *Boreas*, 33(4), pp.284–299. (doi: 10.1111/j.1502-3885.2004.tb01242.x)

Westoby, M.J. et al. (2012). Structure-from-Motion photogrammetry: A low-cost, effective tool for geoscience applications. *Geomorphology*, 179, pp.300–314. (doi: 10.1016/j.geomorph.2012.08.021)

Zick, W. (1972). Eisbewegungen am Eqip Sermia und im westlichen Randgebiet des grönländischen Inlandeises (EGIG Arbeitsgebiet). *Polarforschung*, pp.24–30.

Zwally, H.J. et al. (2011). Greenland ice sheet mass balance: Distribution of increased mass loss with climate warming; 2003-07 versus 1992-2002. *Journal of Glaciology*, 57(201), pp.88–102. (doi: 10.3189/002214311795306682)

Zwally, H.J. et al. (2002). Surface melt induced acceleration of Greenland ice sheet flow. *Science*, 297(July), pp.218–222. (doi: 10.1126/science.1072708)
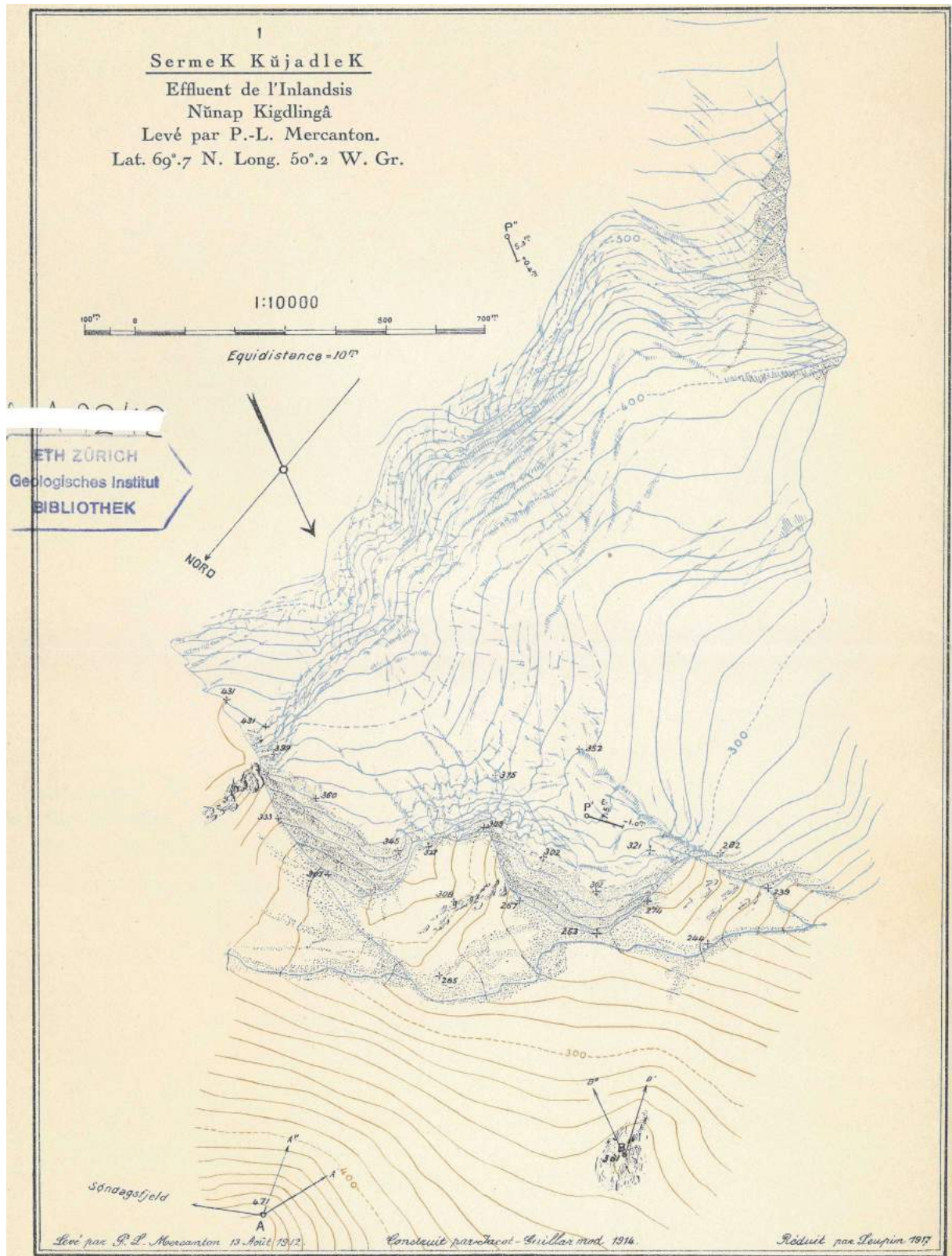
# Appendix

## A. 1912 Maps of Mercanton



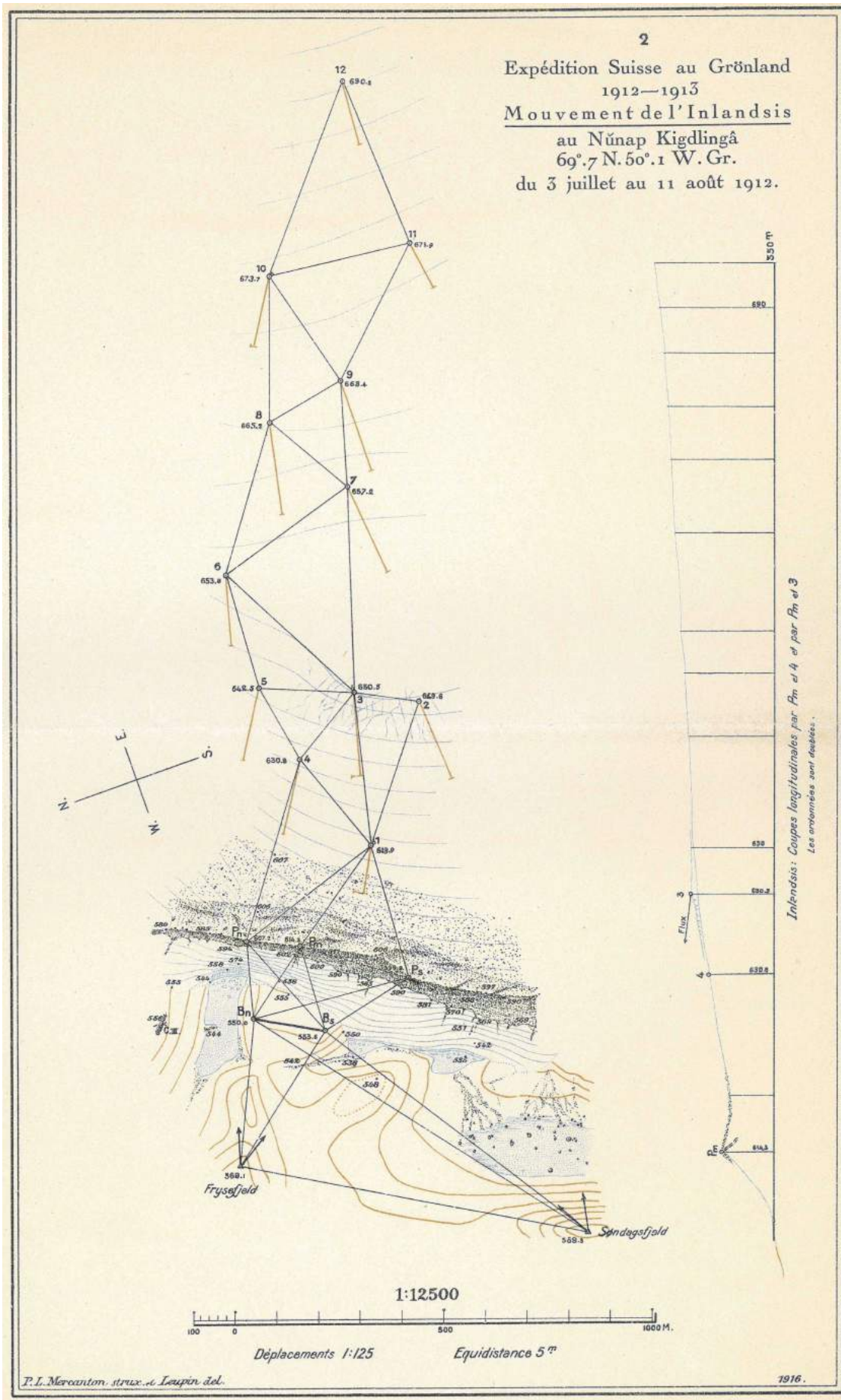*Figure 73*: *Sermeq Kujalleq Map of 1912* (de Quervain & Mercanton 1920)

**Figure 74**: *Nunap Kigdlinga Map of 1912* (de Quervain & Mercanton 1920)

## B.    DEM Differencing

In the following figures there are the enlarged dh-grids displayed in Figure 45. For each Figure the glacier extent lines of Sermeq Kujalleq are also marked for the two DTM datasets. Note that the hill shade of ADcomp was inserted in the background for ease of orientation.
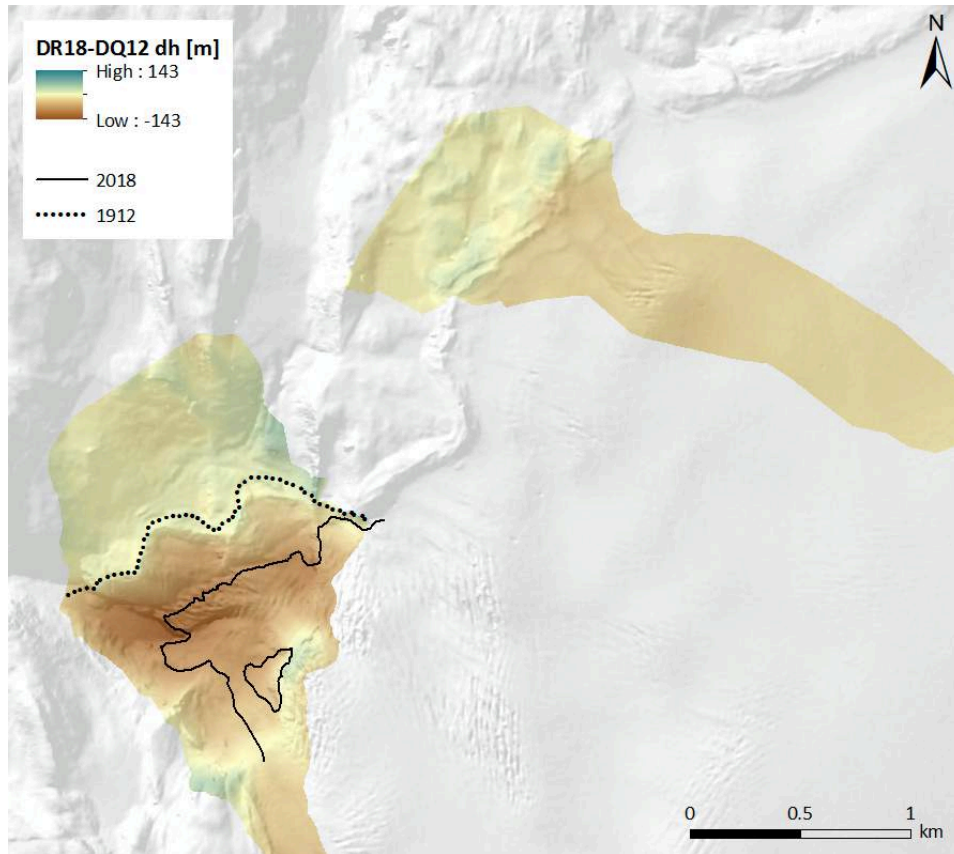


***Figure 75****: Surface elevation change between 13.08.1912 (DQ12) and 08.07.2018 (DR18).*
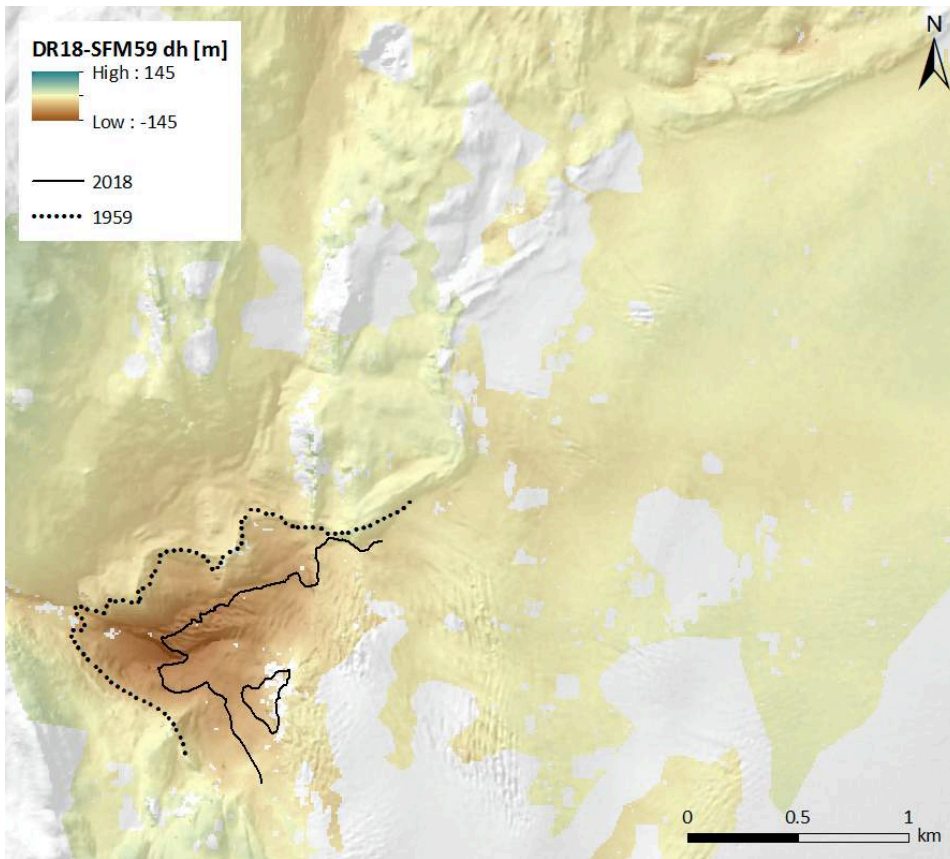
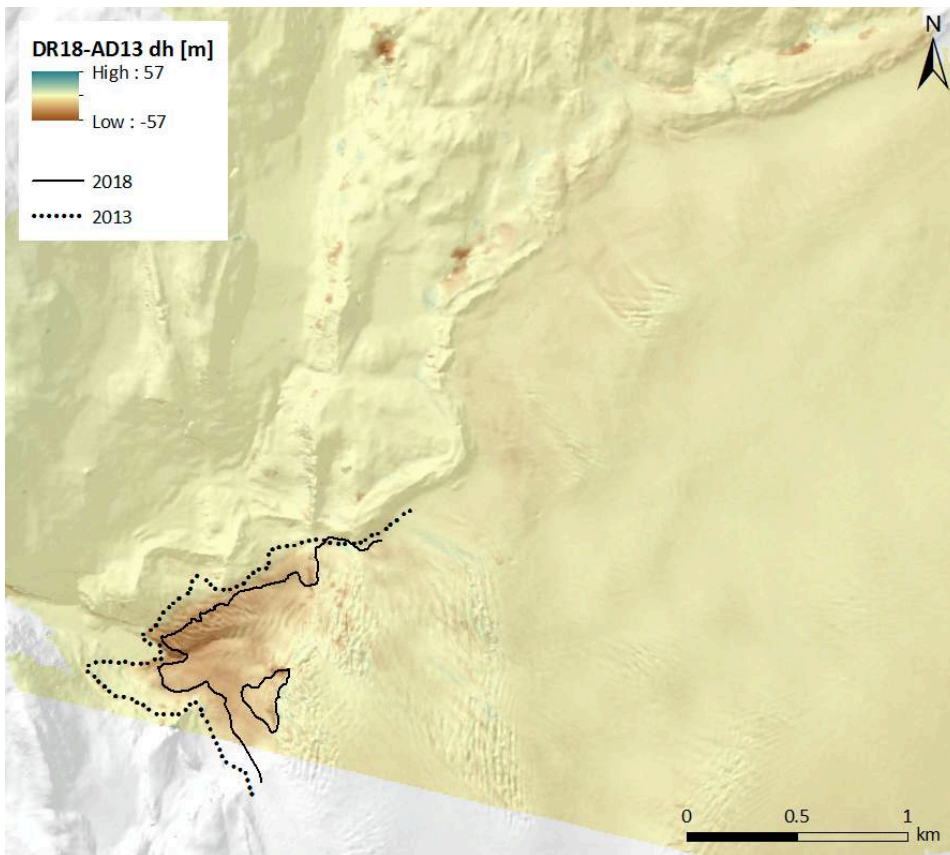*Figure 76: Surface elevation change between 25.06.1959 (SFM59) and 08.07.2018 (DR18).*
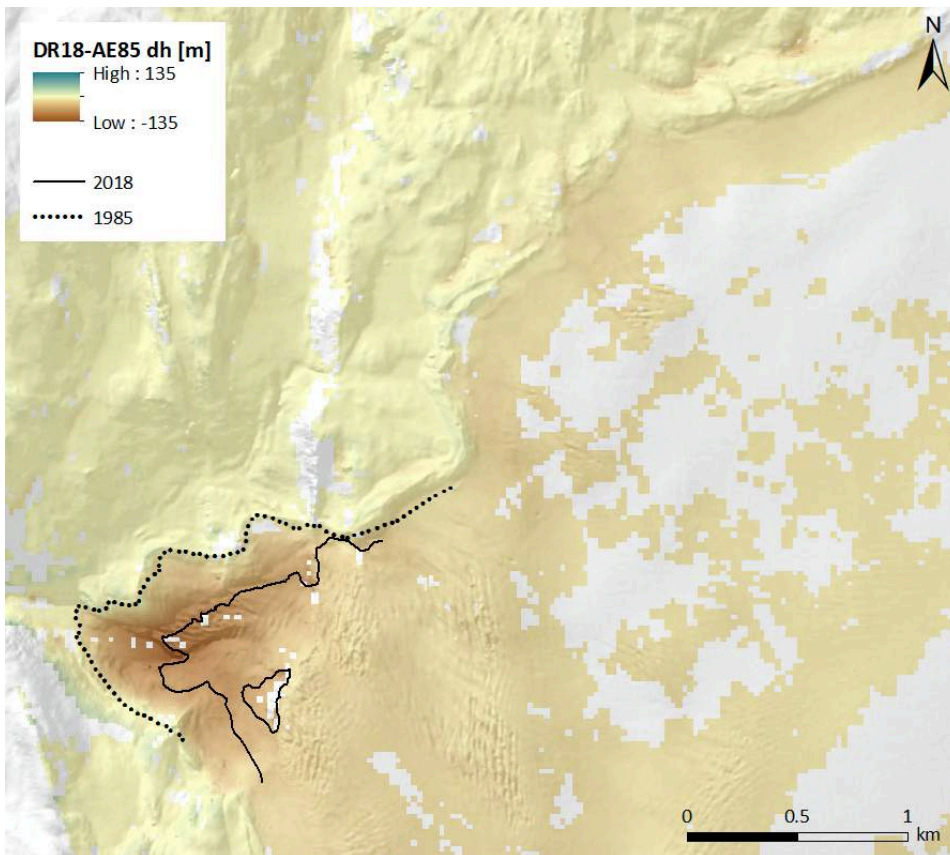


*Figure 77: Surface elevation change between 09.07.1985 (AE85) and 08.07.2018 (DR18).*
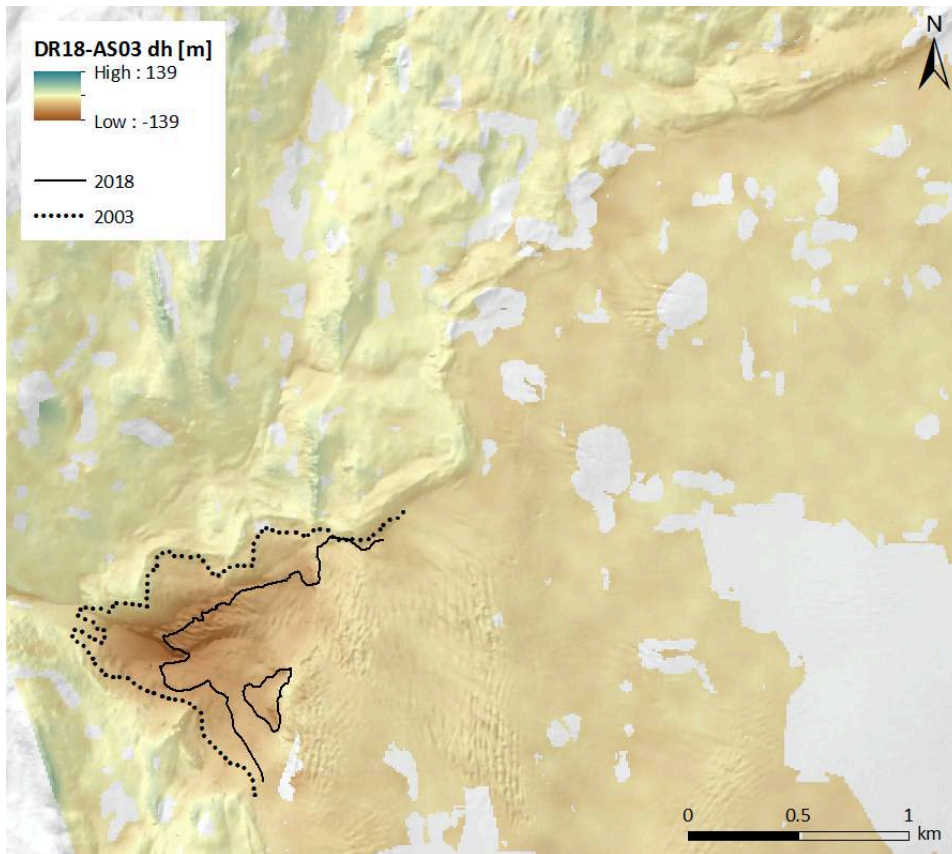
*Figure 78*: Surface elevation change between 09.06.2003 (AS03) and 08.07.2018 (DR18).
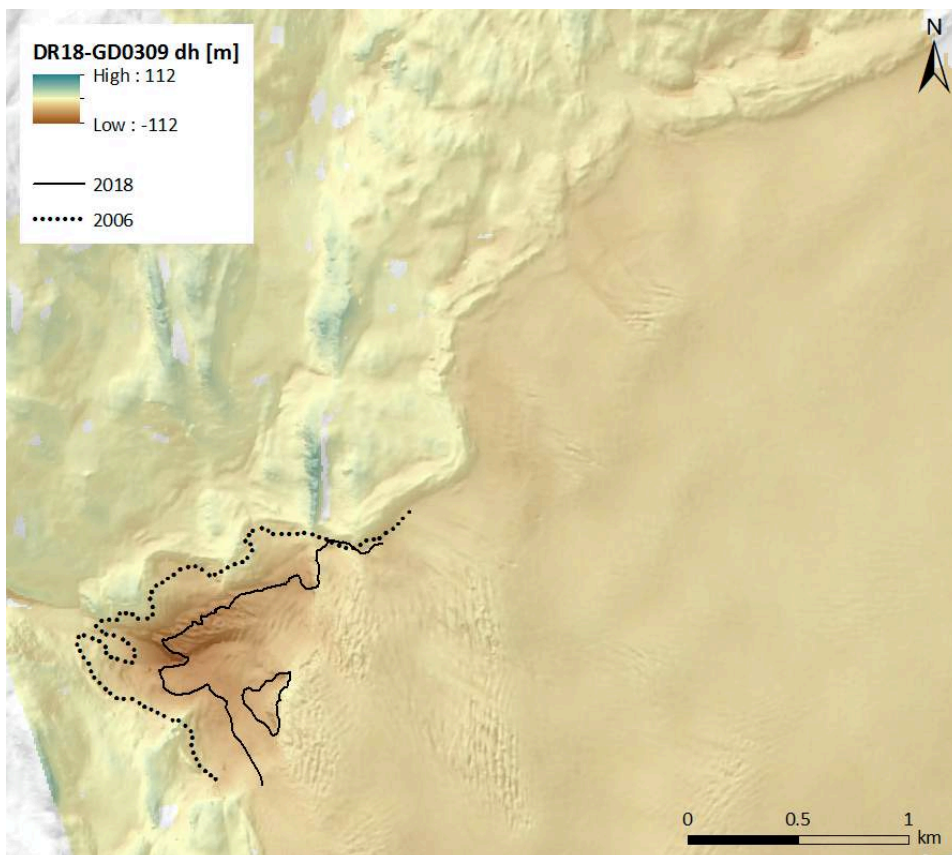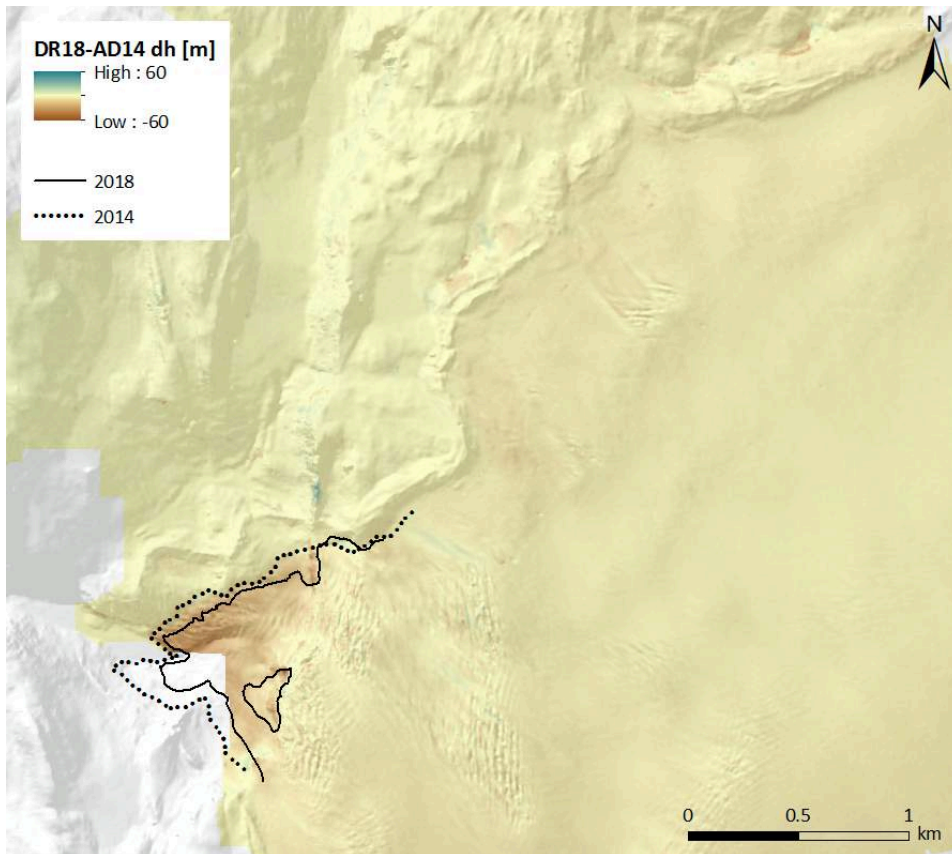


*Figure 79*: Surface elevation change between the GimpDEM (2003-2009, exact acquisition date unknown) and 08.07.2018 (DR18). The glacier extent marked for 2006 is from 19.07.2006.
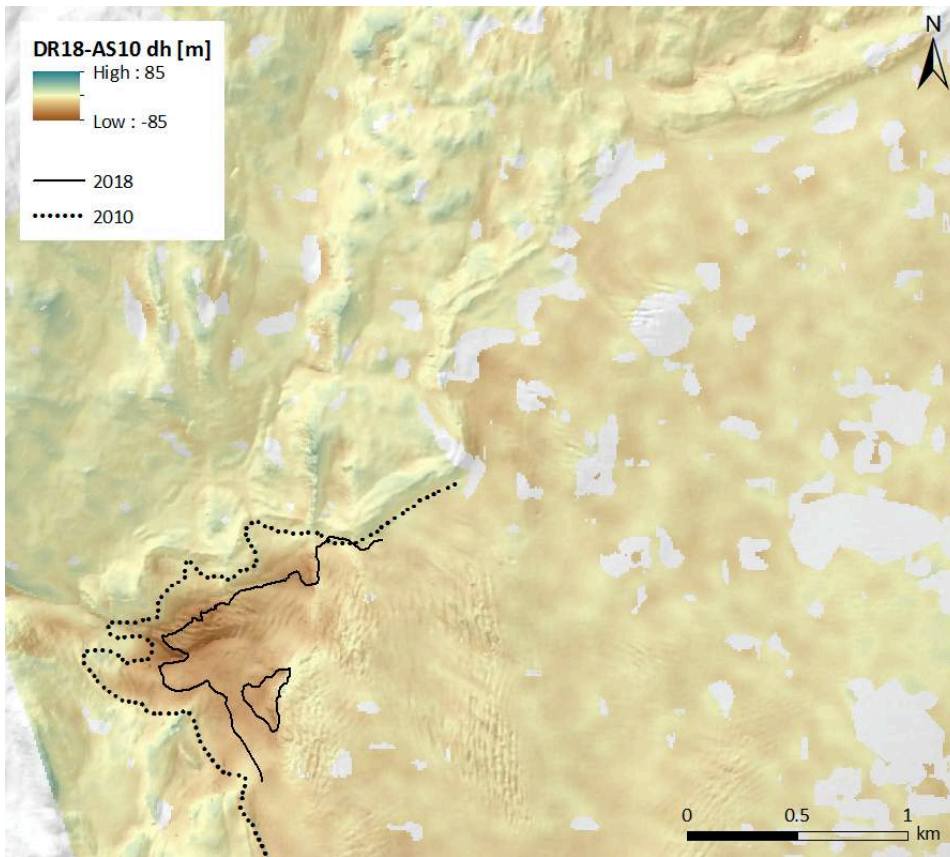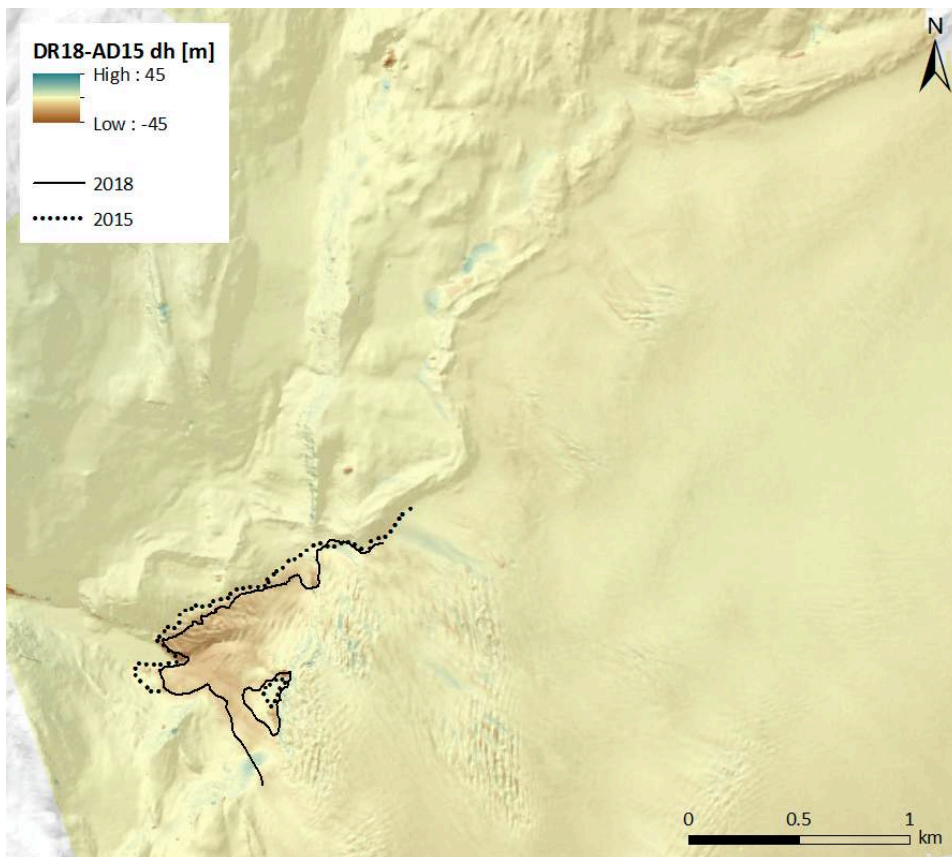
*Figure 80*: Surface elevation change between 09.07.2010 (AS10) and 08.07.2018 (DR18).



*Figure 81*: Surface elevation change between 11.08.2013 (AD13) and 08.07.2018 (DR18).

*Figure 82*: Surface elevation change between 04.07.2014 (AD14) and 08.07.2018 (DR18).



*Figure 83*: Surface elevation change between 24.10.2015 (AD15) and 08.07.2018 (DR18).
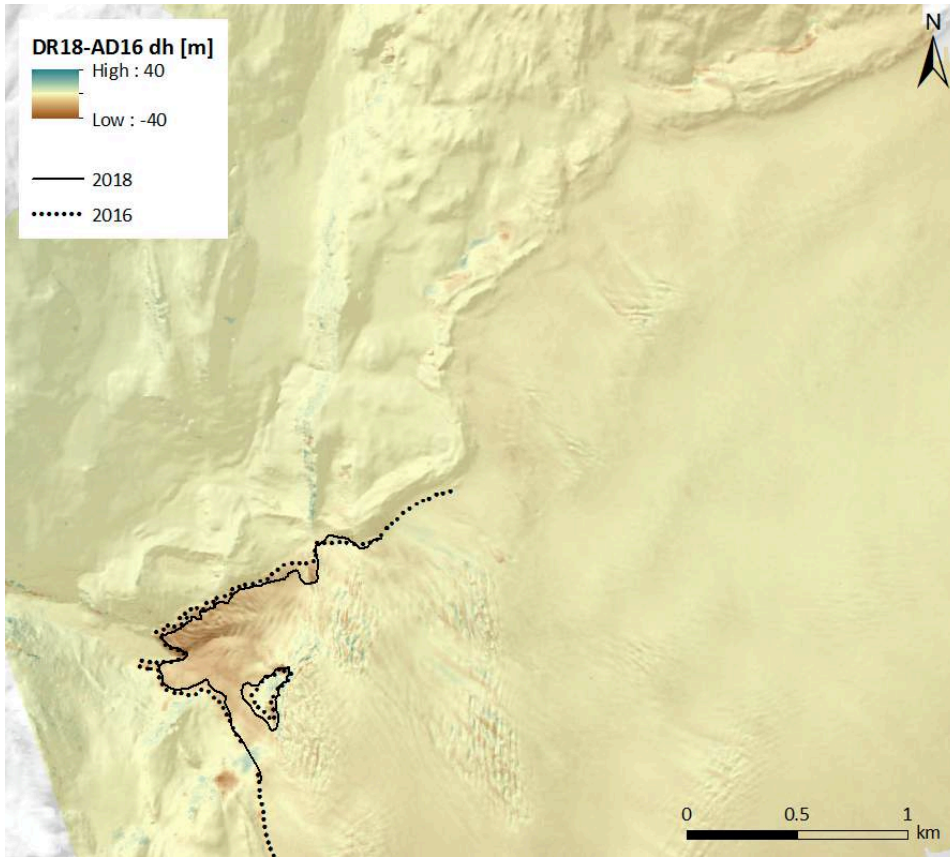
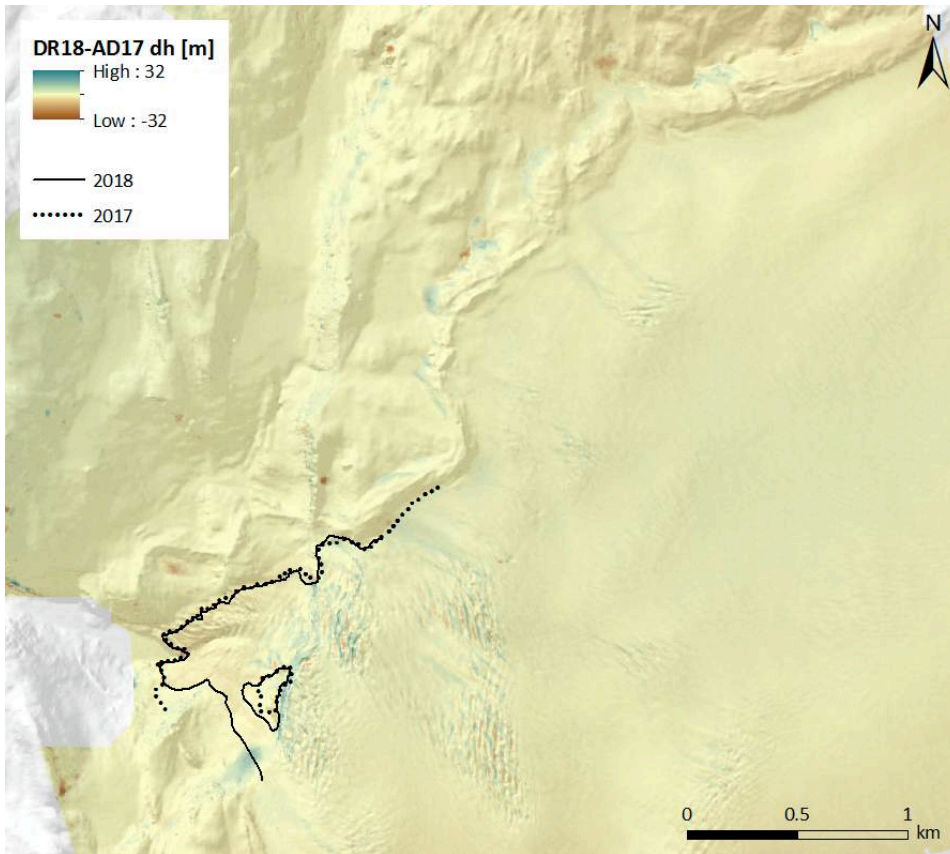*Figure 84*: Surface elevation change between 11.03.2016 (AD16) and 08.07.2018 (DR18).



*Figure 85*: Surface elevation change between 11.08.2017 (AD17) and 08.07.2018 (DR18).
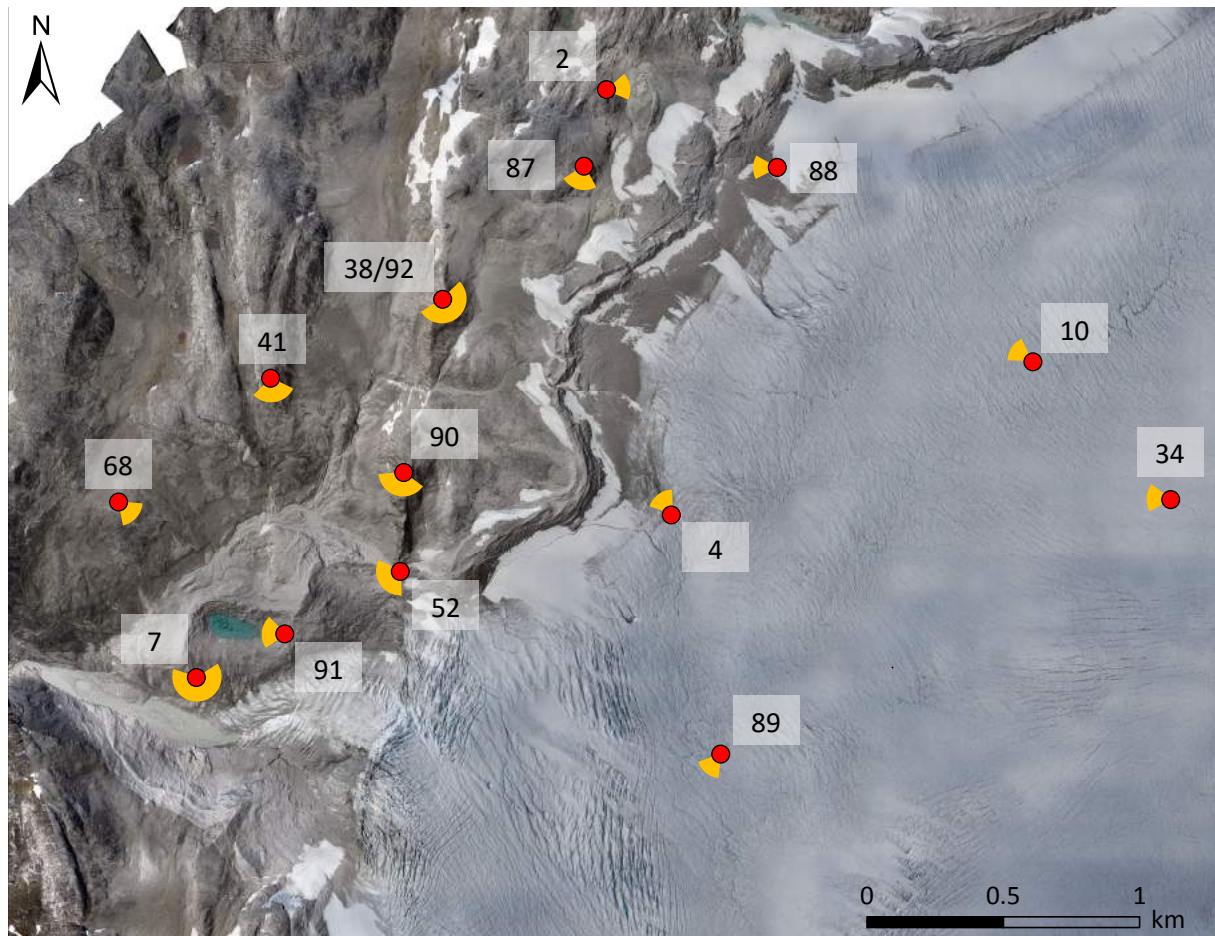
## C.    Additional Photographs



***Figure 86****: Image positions (red) and viewing angles (yellow) for the different figures of this thesis. Labels are according to Figure numbers. Background image: Orthophoto and hill shade of DR18.*
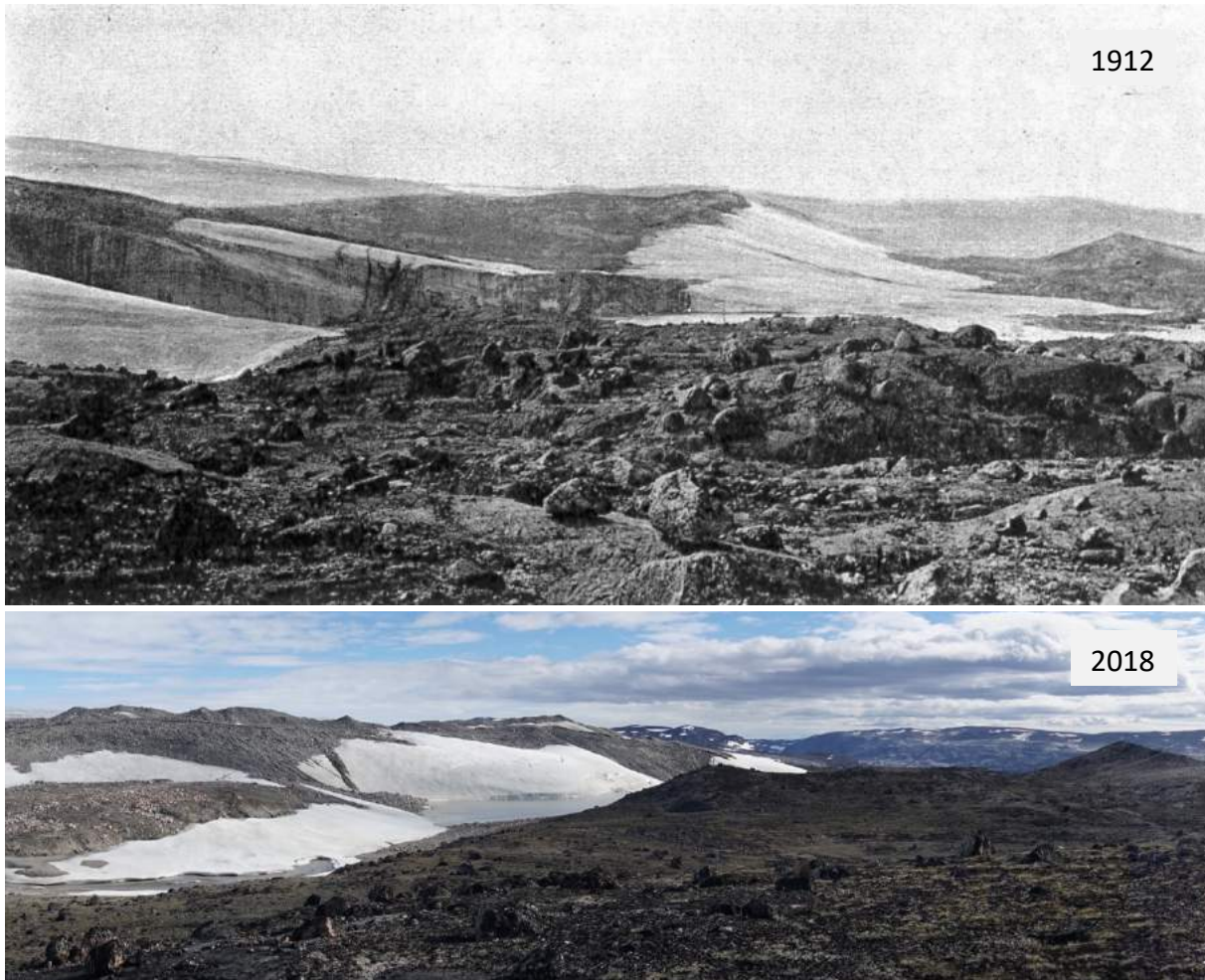
1912

2018

*Figure 87*: Forefield of the ice margin (Søndagsfjell on the right). Note that the actual position of the photograph couldn't be determined. Photos from 1912 (de Quervain & Mercanton 1920) and 2018 (Simon Schudel).



*Figure 88*: Nunap Kigdlinga ice sheet margin. View from zone 5 towards the ice-cored moraine (zone 4). For location of the image refer to Figure 86. Image by Simon Schudel (July 2018).

***Figure 89****: Supraglacial melt water pond above the main Sermeq Kujalleq ice cascade. For location of the image refer to Figure 86. Image by Simon Schudel (July 2018).*



***Figure 90****: Sermeq Kujalleq. For location of the image refer to Figure 86. Image by Simon Schudel (July 2018).*

***Figure 91****: Lake that has formed behind the terminal moraine of Sermeq Kujalleq. For location of the image refer to Figure 86. Image by Simon Schudel (July 2018).*
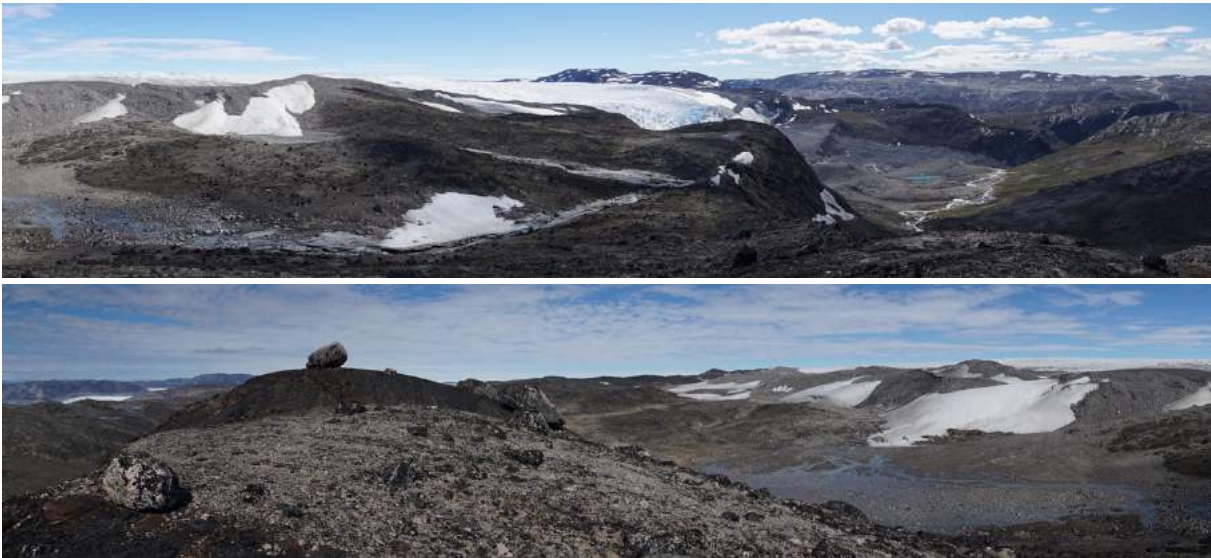


***Figure 92****: View from Sondagsfjell towards south (top) and west (bottom). For location of the image refer to Figure 86. Images by Simon Schudel (July 2018).*

***Figure 93***: *Field work base camp ('Eqi Camp') with the EGIG hut and the Eqip Sermia terminus in the background. Image by Simon Schudel (July 2018).*

## D.    Pearson Correlation Coefficient

$$R = \frac{\sum_{i=1}^{n}(x_i - \bar{x})(y_i - \bar{y})}{\sqrt{\sum_{i-1}^{n}(x_i - \bar{x})^2}\sqrt{\sum_{i-1}^{n}(y_i - \bar{y})^2}}$$

*Equation 18*

$\bar{x}$        = sample mean of the measured surface elevation change

$\bar{y}$        = sample mean of the simulated surface elevation change

$n$        = sample size

$x_i$        = individual sample points of the measured surface elevation change indexed with *i*

$y_i$        = individual sample points of the simulated surface elevation change indexed with *i*

## E.    Workflow Overview



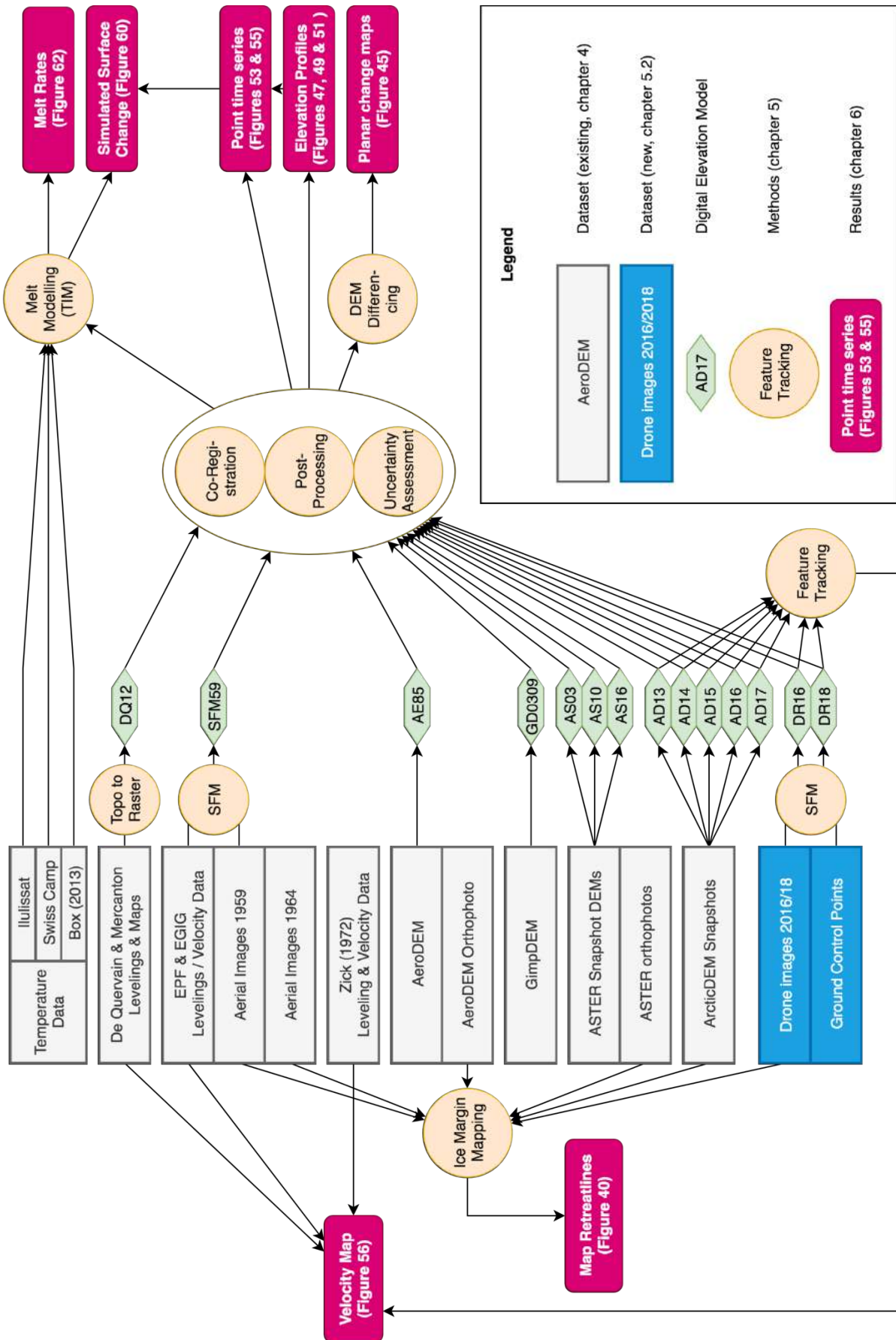***Figure 94****: Overview of the thesis workflow.*

## Personal Declaration

I hereby declare that the submitted thesis is the result of my own, independent work. All external sources are explicitly acknowledged in the thesis.

Simon Schudel

31.01.2019, Zürich